Dissertation
submitted to the
Combined Faculties of the Natural Sciences and Mathematics
of Heidelberg University, Germany
for the degree of
Doctor of Natural Sciences

Put forward by
Luca Xaver Bayha
Born in: Stuttgart
Oral examination: 15.07.2020

Emergence of Many-Body Physics in Two-Dimensional Few-Fermion Systems

Referees: **Prof. Dr. Selim Jochim**
Prof. Dr. Markus Oberthaler

Abstract:

This thesis reports on experiments investigating the emergence of many-body physics in mesoscopic two-dimensional (2D) few-fermion systems.
The starting point are low-entropy samples of ultracold ^{6}Li atoms in a quasi-2D geometry. When scanning the depth of the trapping potential, we observe an enhanced stability of closed-shell configurations of the 2D harmonic oscillator. This enables us to deterministically initialize closed-shell configurations of 2, 6 and 12 atoms in the ground state.
By modulating the interaction strength we probe the excitation spectrum arising from the interplay of the finite single-particle gap in closed-shell configurations with the tunable attractive interactions. The full atom-counting statistics reveal pair excitations with a non-monotonous interaction dependence. These modes can be identified as the few-body precursors of a Higgs mode associated with a normal to superfluid phase transition in the thermodynamic limit.
Additionally, we can access the momentum distribution with single-particle resolution. This is demonstrated by measuring the momentum distribution of up to six non-interacting fermions in the ground state of the 2D trap. We observe strong density correlations that arise from fermionic quantum statistics. In the future, extending the imaging scheme to interacting systems will allow us to observe the emergence of fermionic many-body paring directly in momentum space.

Zusammenfassung:

Diese Arbeit beschreibt Experimente, welche die Entstehung von kollektivem Verhalten in zweidimensionalen fermionischen Wenigteilchensystemen untersuchen. Ausgangspunkt der Experimente sind ultrakalte ^{6}Li-Atome in einer Quasi-2D-Fallengeometrie. Beim Scannen der Tiefe des 2D-Potentials beobachten wir eine erhöhte Stabilität des Systems bei Atomzahlen, die Konfigurationen geschlossener Schalen des zweidimensionalen harmonischen Oszillators entsprechen. Dies ermöglicht es uns, geschlossene Schalen von 2, 6 und 12 Atomen im Grundzustand deterministisch zu initialisieren.

Wir untersuchen das Anregungsspektrum, welches sich aus dem Zusammenspiel der endlichen Energielücke von Anregungen einzelner Atome in einer geschlossenen Schale mit der einstellbaren anziehenden Wechselwirkung ergibt. Das Spektrum zeigt bemerkenswerte Paaranregungen mit einer nicht monotonen Wechselwirkungsabhängigkeit. Diese Moden können als die Vorläufer von Higgs-Moden in einem Wenigteilchensystem identifiziert werden. Im thermodynamischen Limit sind die Higgs-Moden mit einem Phasenübergang von einer normalen- zu einer Supraflüssigkeit verknüpft.

Im Experiment können wir auch die Impulsverteilung mit Einzelteilchenauflösung messen. Dies wird anhand von Messungen der Impulsverteilung von bis zu sechs nicht wechselwirkenden Fermionen im Grundzustand der 2D-Falle gezeigt. Wir beobachten starke Dichtekorrelationen, die sich aus der fermionischen Quantenstatistik ergeben. Eine Kombination der vorgestellten experimentellen Ergebnisse ermöglicht zukünftige Messungen, welche die Entstehung von fermionischer Vielteilchen Paarbildung direkt im Impulsraum untersuchen.

Contents

1. Introduction **1**

2. Theoretical Framework **5**

2.1. The Harmonic Oscillator 5
2.2. Quantum Statistics 6
2.3. Ultracold Interactions 9
2.3.1. Low Energy Scattering 10
2.3.2. Tuning Interactions 12
2.3.3. Mean-Field Interactions 15
2.3.4. Scattering in 2D 15
2.3.5. Two Particles in a Harmonic Trap 18
2.4. Many-Body Physics 22
2.4.1. Phase Transitions 23
2.4.2. The BEC-BCS Crossover 27
2.4.3. Finite Temperature 33
2.4.4. BEC-BCS Crossover in 2D 34
2.4.5. BCS Theory for Trapped Fermions 35

3. Experimental Tools and Setup **41**

3.1. Properties of Lithium 41
3.2. Vacuum Chamber and Experiment Control 41
3.3. Dissipative Cooling 42
3.4. Optical Dipole Traps and Evaporative Cooling 44
3.4.1. Conservative Potentials and Light Shifts 44
3.4.2. Experimental Realization 45
3.4.3. The 2D Trap 45
3.5. Magnetic Fields for State Manipulation 46
3.6. Absorption Imaging 47
3.7. Condensation in a Quasi-2D Fermi Gas 48
3.8. Many-Body Paring in the Normal Phase 50

4. Experimental Tools to Study Mesoscopic Fermi Systems 53
4.1. Creating Arbitrary Potentials 54
4.1.1. Fourier Optics 55
4.2. Physical Implementation 57
4.2.1. The High Resolution Objective 60
4.3. Single Atom Detection 61
4.3.1. MOT Imaging 62
4.3.2. Free Space Fluorescence Imaging 64
4.4. Deterministic Preparation 68
4.5. Manipulating the Potential 73
4.5.1. Correcting Aberrations 73
4.5.2. Measuring Trap Frequencies 75
4.5.3. Transforming the Trap 78

5. Observing the Few-Body Precursor of a Phase Transition 81
5.1. Creating Closed Shells of 2D Fermions 82
5.1.1. Transfer to a Quasi-2D Trap 82
5.1.2. Observing the Shell Structure of a 2D Fermi Gas 84
5.2. Emergence of Collective Excitations 91
5.2.1. Excitation Spectrum 91
5.2.2. Tuning Interactions 94
5.2.3. Comparing Different Excitation Schemes 98
5.2.4. Approaching the Many-Body Limit 99
5.3. Coherent Control of Strongly Interacting Fermions 101

6. Observing a Pauli-Crystal 105
6.1. Sampling the Many-Body Wavefunction 106
6.2. Melting the Crystal 109

7. Conclusion and Outlook 113

Bibliography 116

A. Appendix 133

1. Introduction

Many-body physics describes phenomena that are often difficult to understand from looking only at the individual constituents of the system and a microscopic theory [1]. This is due to emergent collective behavior such as symmetry breaking, phase transitions and new effective collective degrees of freedom [2]. Remarkably, the properties of such many-body systems are often universal in the sense that they do not depend on the microscopic details of the underlying Hamiltonian, but rather on its symmetry [3–5]. Some of the most striking examples are the universal low-energy modes in symmetry-broken phases, like the excitation spectrum of superfluids and sound modes in crystals [4].

This universality raises two important questions: How do similar many-body phenomena emerge from different microscopic Hamiltonians and how is the physics of microscopic systems connected to the thermodynamic limit. These questions are especially relevant for mesoscopic samples. On the one hand they are still far away from the thermodynamic limit. On the other hand they contain already too many particles to be solved exactly, due to the exponential growth of Hilbert space size. The remarkable experimental observation is that, although the concepts of symmetry breaking are strictly valid only in the thermodynamic limit, they are already important for mesoscopic systems consisting of only tens of particles [6].

Understanding how many-body physics emerges is also of practical interest, as most of the matter around us consists of mesoscopic substructures, since both atoms and nuclei are in this range of system sizes. Whereas the spectra of atoms are dominated by the strong central potential and can mainly be described by single particle excitations, nuclei are a prime example for emergent behavior. They are dominated by the attractive interactions and show collective excitations [7] and spectra consistent with a BCS superfluid [8].

Systematic experiments on the emergence of collectivity in these naturally occurring systems are difficult considering the limited tunability of both interactions and particle number. First experiments with artificial model systems in this range of particle numbers have been performed with liquid helium droplets, where the emergence of superfluidity was observed for around 50 particles [6]. Other de-

signer systems are quantum dots [9] and atomic clusters [10]. Like liquid helium droplets, they allow for flexible preparation of different atom numbers, but interactions cannot be tuned.
Recently, ultracold atoms have been used as a platform to study the emergence of many-body physics in few-fermion systems [11, 12]. They are ideal model systems, as they offer free tunability of the trapping geometry, quantum statistics, and even the interactions [13]. Moreover, it is possible to create both few-particle [14] and macroscopic systems [15, 16] governed by exactly the same microscopic Hamiltonian.

Here, we extend the studies of deterministically initialized ultracold few-fermion systems to quasi-2D geometries. Compared to the previously available quasi-1D systems, they resemble the behavior of nuclei and atoms more closely, as symmetries of the Hamiltonian result in degenerate levels and the emergence of energy shells for fermions. Furthermore, in these two-dimensional systems, manifestations of many-body physics, such as phase transitions, can be observed [17, 18].
In this work we study a few-particle system of attractively interacting fermions. In the many-body limit this system has been studied extensively both in theory and experiment [19–25]. Here, the ground state is a superfluid for any finite attraction. This interesting many-body limit in combination with the tunability of ultracold atoms allows us to experimentally address the question of how superfluidity emerges in mesoscopic fermionic systems.
The confinement required to create small instances of interacting fermions in 2D introduces a second energy scale, which is given by the trap level spacing. Here, the most interesting configurations are these corresponding to closed shells, where Pauli blocking results in a finite single-particle gap. Therefore, the Fermi surface has an enhanced stability towards perturbations and the single-particle gap suppresses pairing for weak attraction. In contrast to the bulk system, this results in a normal to superfluid phase transition upon increasing the interactions [26]. In the vicinity of this phase transition point the low-energy behavior of the system is governed by emergent universal modes [27].
Experimentally, we access this regime by the deterministic preparation of closed-shell configurations of ^{6}Li in a quasi-2D harmonic oscillator. The achievement of initializing these states with high fidelity is the starting point for all further measurements. We study the excitation spectrum of the closed-shell configurations in dependence of the interaction strength. We observe pair excitation modes, which, by comparison to numerics [28], can be identified as the few-body precursors of a universal mode connected to the phase transition in the many-body limit.

In a last set of experiments we lay the foundation for a more detailed future study of the few-body precursor of the phase transition. We implement a single-particle and momentum resolved imaging scheme. This allows us to sample the many-body wavefunction of non-interacting fermions. We observe strong correlations in the momentum density of identical fermions arising from the anti-symmetrization of the wave function.

Outline

- In chapter 2, we provide the theory background required to understand the measurements presented in the remainder of the thesis. We start with a review of quantum statistics and the interactions of two ultracold atoms, both in free space and in a confined geometry. This is the foundation for our preceding discussion of symmetry breaking and the phase diagram of attractively interacting fermions. Here, we will focus on the influence of an external trapping potential and few-particle signatures of the many-body physics.

- Chapter 3 gives an overview of the experimental setup and methods used to study large clouds of quasi-2D ultracold fermions. This is followed by a summary of the experimental results on the 2D BEC-BCS crossover obtained with this setup.

- In chapter 4, we discuss the changes made to the experiment and the tools implemented to study mesoscopic Fermi systems in tunable geometries.

- In chapter 5, we present the experimental results on the observation of the few-body precursor of a quantum phase transition. We first discuss our ability to deterministically create closed-shell configurations of quasi-2D ultracold fermions and demonstrate their enhanced stability. Starting from these systems we study the interplay of the single-particle spectrum with the freely tunable interactions. The full counting statistics of the many-body excitation spectrum of the few-fermion system reveals a peculiar pair excitation mode. By comparison to theory we show that this mode is the few-body precursor of the amplitude mode associated to the normal to superfluid phase transition.

- In chapter 6 we present our measurements of the momentum distribution of identical fermions. Using single atom resolved imaging, we observe correlations in the momentum density of the deterministically created closed-shell configurations. These correlations arise from the anti-symmetry of the wavefunction when exchanging identical fermions.

- In the last chapter, we provide a short summary of the main results obtained in this thesis and the avenues this setup opens for the exploration of how correlations and many-body pairing emerge in strongly interacting mesoscopic Fermi systems.

2. Theoretical Framework

In this chapter we provide the theoretical background and physical concepts required to understand the measurements presented in the rest of this thesis. Starting from a single particle in a harmonic trap we give an overview over the different concepts employed for the description of (strongly) interacting ultracold fermions. We discuss the influence of quantum statistics on the properties of ensembles of non-interacting particles. In the next step, interactions are introduced and the properties of two interacting ultracold atoms, both in free space and a trap are summarized. This is followed by a brief review of the essential ingredients of the BEC-BCS crossover and the excitation modes of symmetry broken phases. Lastly, we discuss how to connect this many-body regime to the few-body limit.

2.1. The Harmonic Oscillator

In all our experiments, we trap atoms in an attractive potential. This confinement results in a discrete spectrum and a finite ground-state energy. Close to the potential minimum, the confinement can be approximated by a harmonic oscillator. For the 1D harmonic oscillator the potential it is given by $V = \frac{1}{2}m\omega^2 x^2$, where ω denotes the trap frequency. Hence, the Hamiltonian is

$$\hat{H} = -\frac{\hbar^2}{2m}\partial_{\mathrm{x}}^2 + \frac{1}{2}m\omega^2 x^2, \tag{2.1}$$

with the mass m and $\hbar$ is the reduced Planck's constant. The eigenstates are denoted by $|n\rangle$, with $n \in \mathbb{N}_0$ and have an energy $E_{\mathrm{n}} = \hbar\omega(n + \frac{1}{2})$. The wavefunctions of the eigenstates are Hermite polynomials times an additional Gaussian envelope [29]. The eigenfunctions have the same shape in real and momentum space, as the Hamiltonian is symmetric under exchange of position x and momentum p.

The energy scale $\hbar\omega$ also defines the typical length and momentum scales of the problem given by the harmonic oscillator length $l_{\mathrm{ho}} = \sqrt{\hbar/(m\omega)}$ and harmonic oscillator momentum $p_{\mathrm{ho}} = \sqrt{\hbar m\omega}$.

For higher dimensional systems the potential is given by the sum of harmonic potentials along the different axes. The problem is separable and the eigenstates are products of the 1D solutions. For a round 2D harmonic oscillator, i.e. $\omega_x = \omega_y$, the eigenstates are given by $|n_\mathrm{x}, n_\mathrm{y}\rangle$ and the energy $E = \hbar\omega(n_\mathrm{x} + n_\mathrm{y} + 1)$ depends only on the sum of n_x and n_y. This degeneracy is due to the rotational symmetry of the problem and the Hamiltonian commutes with the angular momentum operator. Hence, there exist simultaneous eigenstates, which are labeled $|n, L_z\rangle$, where $n \in \mathbb{N}_0$ is the principal quantum number and the angular momentum is given by L_z. The angular momentum can take values

$$L_z = n, n-2, \ldots, 0, \ldots, -n+2, -n \qquad \text{for} \quad n \quad \text{even}, \tag{2.2}$$

$$L_z = n, n-2, \ldots, 1, -1, \ldots, -n+2, -n \qquad \text{for} \quad n \quad \text{odd}. \tag{2.3}$$

The energy of the n^{th} shell is given by $E_\mathrm{n} = \hbar\omega(n+1)$ and it contains $n+1$ degenerate energy levels. The level structure is sketched in Fig. 2.1.
Realistic potentials are, however, never perfectly harmonic. This results in an unequal spacing of the energy shells. For the Gaussian potentials used to trap ultracold atoms the confinement becomes weaker for shells with higher energy, i.e. the energy difference between the first and second shell is larger than the energy difference between the second and third shell. Additionally, the anharmonicity results in a splitting of the energy of different states in a shell, where states with the same $|L_z|$ have the same energy. In most cases this anharmonicity is only a small perturbation to the harmonic potential.
For an anisotropic trap $\omega_x \neq \omega_y$, angular momentum is not a good quantum number anymore. For small anisotropies the system can still be described in terms of energy shells. However, the different levels within a shell are not degenerate anymore, but are slightly split by the trap anisotropy.
With the single particle spectra at hand, we will discuss the properties of systems consisting of indistinguishable particles in the next section. There we will see that quantum statistics has a strong influence on the behavior of a non-interacting system.

2.2. Quantum Statistics

Classically, even identical particles can be distinguished by their phase space trajectories. In quantum mechanics, however, identical particles are indistinguishable. The indistinguishability becomes relevant, when the density of particles in phase space becomes comparable to the phase space cell volume and different par-

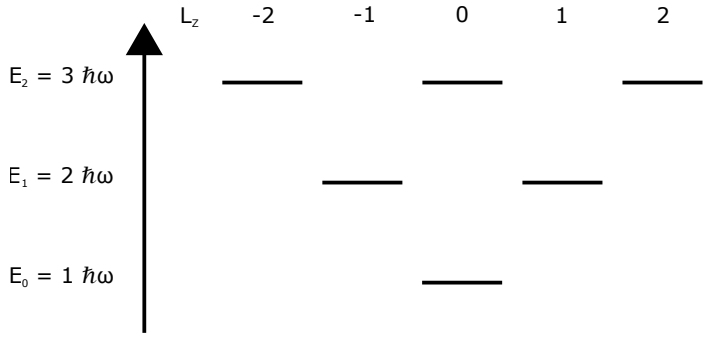

Figure 2.1.: **Level structure of the 2D harmonic oscillator.** The different shells are labeled by the principal quantum number n and there are $n+1$ degenerate states in each energy shell. The states within a shell differ by their angular momentum L_z.

ticles cannot be discerned by their phase space trajectories anymore. This is the case when the deBroglie wavelength [30] $\lambda_{\mathrm{dB}} = p/h$, where h is Planck's constant, is similar to the inter-particle spacing d. Clearly, the outcome of a measurement cannot change when exchanging two identical particles. This implies

$$|\Psi(x_1, \ldots, x_{\mathrm{i}}, \ldots, x_{\mathrm{j}}, \ldots, x_{\mathrm{n}})|^2 = |\Psi(x_1, \ldots, x_{\mathrm{j}}, \ldots, x_{\mathrm{i}}, \ldots, x_{\mathrm{n}})|^2. \tag{2.4}$$

Here, x_{i} labels the i^{th} particle and includes both external and internal degrees of freedom. Since this holds for any pair of indistinguishable particles the wavefunction has to be either anti-symmetric or symmetric under the exchange of identical particles, i.e.

$$\Psi(x_1, \ldots, x_{\mathrm{i}}, \ldots, x_{\mathrm{j}}, \ldots, x_{\mathrm{n}}) = \pm\Psi(x_1, \ldots, x_{\mathrm{j}}, \ldots, x_{\mathrm{i}}, \ldots, x_{\mathrm{n}}). \tag{2.5}$$

The class a particle belongs to is determined by its spin via the spin-statistics theorem [31]. Half-integer spin particles, where we give the spin in units of the reduced Planck's constant, correspond to the minus sign and are called fermions. Integer spin particles are called bosons and correspond to the plus sign. This also holds for composite particles such as ^{6}Li, which consist of an odd number of fermions and thus has a half-integer spin and is itself a fermion. We will briefly discuss the consequences of the two different exchange statistics on the properties of many-body systems.

Fermions

The many-body wavefunction of fermions is anti-symmetric under the exchange of two particles. The easiest way of obtaining such a many-body wavefunction is to take the Slater determinant of the single-particle wavefunctions. The anti-symmetry implies that there can be at most one fermion per quantum state, which is nothing other than the Pauli exclusion principle [32]. This also affects the thermodynamics of the system, where the probability of a state with energy ϵ being occupied with a fermion at a temperature T is given by the Fermi-Dirac distribution [33]:

$$n_{\mathrm{f}}(\epsilon, \mu, \beta) = \frac{1}{\exp(\beta(\epsilon - \mu)) + 1}, \tag{2.6}$$

where $\beta = \frac{1}{k_{\mathrm{B}}T}$ is the inverse temperature and k_{B} denotes the Boltzmann constant. The chemical potential μ acts as a Lagrange multiplier fixing the total number of particles in the grand canonical ensemble and corresponds to the energy required to add a particle. At low temperatures ($T \leq \mu$) the particles start to form a so-called Fermi sea, where the states with energy below the chemical potential are occupied by a single fermion with a probability close to 1. At zero temperature the distribution becomes a step function: All states with energy below the chemical potential are occupied, whereas all states above are empty (see Fig. 2.2 (b)). The Fermi energy E_{F} denotes the energy of the highest occupied state at zero temperature $T = 0$ and coincides with the chemical potential μ at $T = 0$. These well-defined occupation probabilities of the different trap levels at low temperatures are essential for the deterministic preparation of mesoscopic samples as will be discussed in chapter 4.1.

Bosons

For bosons the wavefunction is symmetric under particle exchange and there is no restriction on the maximum number of particles occupying a single quantum state. Thus, even a macroscopic number of particles can occupy a single state. This is also seen from the occupation probability of a state, which is given by the Bose-Einstein distribution [33]:

$$n_{\mathrm{b}}(\epsilon, \mu, \beta) = \frac{1}{\exp(\beta(\epsilon - \mu)) - 1}. \tag{2.7}$$

For bosonic systems the chemical potential has to be smaller than the lowest energy level, as otherwise the occupation probability would become negative, which is unphysical. This limits, at a fixed temperature, the number of particles

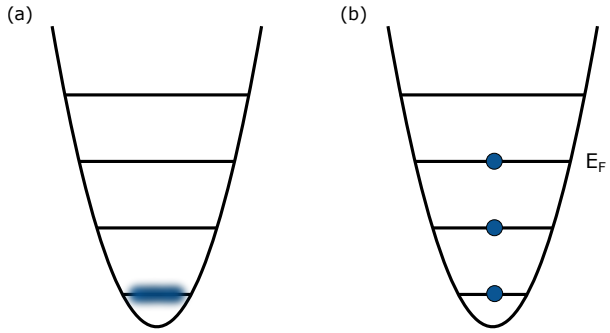

Figure 2.2.: **Occupation of a harmonic trap at zero temperature.** The cases for bosons and fermions are sketched in panel (a) and (b) respectively. At $T = 0$, all bosons occupy the ground state of the potential and the system forms a BEC. For fermions each level is at most occupied by one particle. At zero temperature the system forms a so-called Fermi sea and all states up to the Fermi energy E_F are occupied, whereas all higher lying states are empty. Contrasting (a) and (b) shows the striking influence of quantum statistics on the properties of (non-interacting) many-body systems.

a system can accommodate in the excited states. The largest number N_max of particles at a fixed temperature in the excited states is reached, when the chemical potential is equal to the ground state energy. The number of particles in excited states is then obtained by integrating equation (2.7) over all states, but the ground state. The ground state has to be treated separately, as the number of particles in the ground state N_0 can become macroscopic. For an isotropic 3D harmonic oscillator the maximal number of particles at a temperature T in the excited state is [34]

$$N_\mathrm{max} = Li_3(1)\left(\frac{k_\mathrm{B}T}{\hbar\omega}\right)^3, \tag{2.8}$$

with the polylogarithm $Li_3(1) \approx 1.20$. Thus, when adding more particles than N_max to the trap all additional particles have to be placed in the ground state. The number of particles in the ground state $N_0 = N - N_\mathrm{max}$ becomes a macroscopic fraction of the total particle number. These particles occupying the ground state all have the same wavefunction and the system forms a Bose-Einstein condensate (BEC).

2.3. Ultracold Interactions

So far, we have been discussing non-interacting particles, but much of the richness of ultracold atom experiments stems from our ability to tune their interactions. Thus, as a first step towards interacting many-body physics, we will briefly sum-

marize the scattering of two particles at low temperatures. Here, we will only discuss elastic collisions, as inelastic scattering between two atoms is strongly suppressed and furthermore results in loss of the participating atoms from the trap. Following the discussion in [35, 36], we will find that at these low energies the interactions can be described by a single parameter, the scattering length. Next we will discuss how to modify the interactions by employing a Feshbach resonance, where we will follow the discussion of [37], or by confining the motion of the particles using an external harmonic potential. For strong confinement along a single direction, this results in a scattering process that can be described as being effectively 2D [13, 38].

2.3.1. Low Energy Scattering

For the scattering of two particles, it is convenient to work in relative coordinates and thereby reduce the problem to a single-particle problem, given by

$$-\frac{\hbar^2}{2\mu_r}\nabla^2\Psi(\vec{r}) + V(\vec{r})\Psi(\vec{r}) = E\Psi(\vec{r}). \tag{2.9}$$

Here, μ_r denotes the reduced mass. In the following we assume that the interaction potential $V(\vec{r})$ has a finite range, as it is the case for the experimental relevant van-der-Waals potential. We look for solutions with (positive) energy $E = \frac{\hbar^2 k^2}{2\mu_r}$, where for large distances the energy is purely kinetic. For a spherical symmetric interaction potential the relative wavefunction can be written as [36]

$$\Psi(\vec{r}) = \Psi_{in}(\vec{r}) + \Psi_{out}(\vec{r}) \propto e^{ikz} + f(k,\theta)\frac{e^{ikr}}{r}, \tag{2.10}$$

which is a superposition of the ingoing plane wave and an outgoing scattered spherical wave. Since the potential is rotationally symmetric the scattering amplitude $f(k,\theta)$ can only depend on the angle θ, between the ingoing wave and the direction along which the outgoing wave is observed and not on the azimuthal angle ϕ. The differential cross-section is given by the square of the scattering amplitude. The spherical symmetric interactions conserve angular momentum and the problem can be simplified by expanding it in angular momentum eigenstates, i.e. spherical waves [36]

$$\Psi(r) = \sum_{l=0}^{\infty} P_l(\cos(\theta))\frac{u_{k,l}(r)}{r}. \tag{2.11}$$

The angle dependence is encoded in the Legendre polynomials $P_l(\cos(\theta))$ and the radial wavefunction $u_{k,l}(r)$ is obtained by solving the the radial Schrödinger equation

$$\frac{1}{\mu_r}\partial_r^2 u_{k,l}(r) + \left(\frac{k^2}{\mu_r} + \frac{l(l+1)}{2\mu_r r^2} - \frac{2V(r)}{\hbar^2}\right) u_{k,l}(r) = 0. \tag{2.12}$$

Angular momentum conservation implies that the ingoing and outgoing flux is conserved in each partial wave independently and each partial wave can only obtain a real phase shift δ_l [36]. This yields the scattering amplitude [35]

$$f(k,\theta) = \frac{1}{k}\sum_l (2l+1) e^{i\delta_l} \sin\delta_l P_l(\cos(\theta)). \tag{2.13}$$

At the low temperatures relevant in our experiment the interactions can be further simplified, since only the lowest partial wave picks up a non-trivial phase shift. This can be seen from the momentum dependence of the phase shift, which scales as $\delta_l \propto k^{2l+1}$ for small momenta. Thus, the scattering amplitude vanishes for all partial waves but $l = 0$ at low temperatures, where the relative momenta converge to zero.[1]

Intuitively, this is understood by looking at equation (2.12), where the term $\frac{l(l+1)}{\mu_r r^2}$ describes the centrifugal barrier arising from the angular momentum of the scattering particles. Hence, for energies much lower, than the centrifugal barrier the classical turning point of the particles is at distances much larger than the range of the potential and the interaction potential has no influence on the state of these particles. Thus, we can describe interactions at these low temperatures by a single number, which is the phase shift of the zero angular momentum component. It is convenient to replace the phase shift by the scattering length [35]

$$a_{\mathrm{sc}} = -\lim_{k\to 0}\frac{\tan\delta_0}{k}, \tag{2.14}$$

which gives the zero energy limit of the scattering phase shift and neglects the momentum dependence of δ_0. The next term in the expansion defines the effective range r_{eff} of the potential [37]. For the case of the broad resonances of ^{6}Li the effective range is $r_{\mathrm{eff}} = 87a_0$ [39], where a_0 is the Bohr radius, and the term $k^2 r_{\mathrm{eff}}/2$ can be neglected for all experiments performed in the course of this thesis. Thus, at low temperatures and momenta much smaller than the effective range of the potential the scattering cross-section is

$$\sigma = \frac{4\pi a_{\mathrm{sc}}^2}{1 + a_{\mathrm{sc}}^2 k^2}. \tag{2.15}$$

[1] This is only true, if there are no scattering resonances in the higher partial waves.

For a diverging scattering length the cross-section is limited to $\sigma = 4\pi/k^2$. In this so-called unitary limit interactions only depend on the wavelength of the colliding particles. Here, the system is scale invariant, i.e. looks the same on all scales, as there is only a single scale, that is given by the momentum.

For ultracold scattering we can replace the complicated van-der-Waals potential by a single parameter. This is due to the small energy of the colliding particles, which makes it impossible to probe the microscopic details of the interaction potential. Thus, it is possible to replace the real interaction by a different effective potential, which reproduces the same scattering length. For theory calculations one often employs a delta potential[2] $V_{\text{int}}(r) = \frac{\hbar^2 a_{\text{sc}}}{2\mu_r}\delta(r)$ as the effective interaction potential. This gives a very accurate description of the interactions in our system, where the wavelength is comparable to the inter-particle spacing (degenerate regime), which is much larger than the interaction potential range.

Identical Particles

So far we have not considered the symmetry properties of the wavefunction under particle exchange, i.e. we only considered scattering of distinguishable particles. From section 2.2 we know that for identical particles the wavefunction has to be (anti-)symmetrizied. The center of mass wavefunction is symmetric under particle exchange by construction. For identical particles also the relative wavefunction has to be (anti-)symmetrized. Thus, the cross-section is [36]

$$\frac{d\sigma}{d\theta} = |f(k,\theta) + f(k,\theta-\pi)|^2 \quad \text{and} \quad \frac{d\sigma}{d\theta} = |f(k,\theta) - f(k,\theta-\pi)|^2 \tag{2.16}$$

for bosons and fermions respectively. For identical bosons (fermions) only even (odd) partial waves contribute, but with twice the amplitude. Therefore, a single spin component of ultracold atomic fermions is effectively non-interacting.[3] Consequently, for thermalization of the sample and to access many-body physics, we perform all our experiments with a mixture of two hyperfine states.

2.3.2. Tuning Interactions

The existence of Feshbach resonances in ultracold atomic systems makes it possible to tune interactions over all relevant ranges from non-interacting to being

[2] In 3D one has to take the properly regularized version $V_{\text{int}}(r)\Psi(r) = a_{\text{sc}}\delta(r)\partial_r(r\Psi(r))$ [22].
[3] This is not the case in the presence of higher partial wave resonances or for dipolar quantum gases [40].

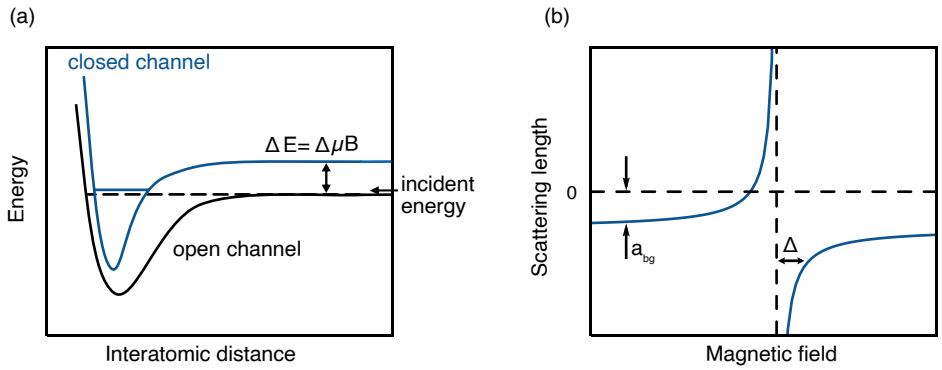

Figure 2.3.: **Sketch of the principle of a Feshbach resonance.** (a) Open (black) and closed channel (blue) interatomic potential. At short interatomic distances the open and closed channel potentials are not eigenstates of the Hamiltonian and the bound states in the closed channel get coupled to the open channel. This results in an additional phase shift of the scattered particle. (b) Sketch of the magnetic field dependence of the scattering length. The Feshbach resonance can be characterized by its width Δ and a background scattering length a_{bg}. Adapted from [37].

the largest energy scale of the system. A Feshbach resonance arises if a quasi-bound state is embedded in a continuum of (scattering) states in the same energy range. Thus, we have to take into account the internal structure of the colliding particles to describe the resonance, which requires two coupled internal states of the particles. The ingoing state configuration is called the open channel. The so-called closed channel is given by a different internal state of the particles and has a larger energy at large interparticle distances. Thus, after the scattering event the particles have to leave again in the closed channel (see Fig. 2.3 (a) for a sketch of the potential curves).

At small relative distances the different channels are not eigenstates of the Hamiltonian, due to e.g. spin-spin interaction and the two channels are coupled. If there is a bound state in the closed channel with energy close to the energy of the incoming scattering particles already a weak coupling of the two internal states changes the scattering process significantly. The coupling to the closed channel results in an additional phase shift of the scattered particles. For the case of a magnetic Feshbach resonance the two channels have different magnetic moments and one can tune their relative energy by applying a magnetic offset-field. This changes the energy of the bound state in the closed channel relative to the energy of the scattering particles and thereby the effective coupling, which in turn changes the scattering length. The scattering length as function of the magnetic

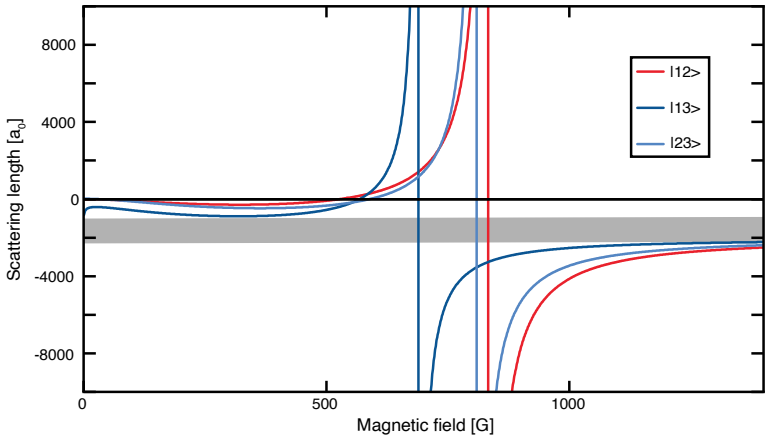

Figure 2.4.: **Scattering length as function of the magnetic field for the lowest three hyperfine states of ^{6}Li.** There exists a broad Feshbach resonance for each of the different combinations. The narrow Feshbach resonance at 548 G is not shown. Note that we can access nearly all scattering lengths apart from a region between -900 and -2100 a_0 (gray area). We label the hyperfine states according to their energy from lowest $|1\rangle$ to highest $|3\rangle$ (see section 3.1). Data for the plot is taken from the supplementary material of Ref. [39].

field B can be approximated by [37]

$$a_{\mathrm{sc}}(B) = a_{bg} + a_{bg}\frac{\Delta}{B - B_0}. \tag{2.17}$$

Here, B_0 is the magnetic field of the resonance position at which the scattering lengths diverges, Δ is the width of the resonance and a_{bg} is the scattering length far away from the resonance, i.e. the scattering length of the open channel without the coupling of the internal states.
For ^{6}Li the open and closed channel are given by the molecular triplet and singlet potential, respectively.[4] They have a different magnetic moment and tuning the magnetic offset field allows us to change the position of the bound state in the singlet potential relative to the threshold of the open channel.
This results in broad Feshbach resonances between the lowest 3 hyperfine states, which we are using in the experiment. The different resonances lie at magnetic fields between $B = 690\,\mathrm{G}$ and $B = 832\,\mathrm{G}$ [39]. Their large width of $\sim 200\,\mathrm{G}$ makes them very convenient to use. The scattering length as function of the magnetic field is shown in Fig. 2.4.

[4]This refers to the electron spin. The two atoms still differ in their nuclear spin such that s-wave scattering is possible.

Bound States

For positive scattering lengths, there exists also a solution of the scattering problem with negative energy. Thus, in addition to the free particle solutions with positive energies, there exists also a bound state for $a_{\mathrm{sc}} > 0$. The binding energy of the molecule is [35]

$$E_{\mathrm{B}} = \frac{\hbar^2}{2\mu_r a_{\mathrm{sc}}^2} = \frac{\hbar^2}{m a_{\mathrm{sc}}^2}. \tag{2.18}$$

This equation holds if the scattering length is larger than the effective range of the potential. The size of a molecule with an energy given by equation (2.18) has to be comparable to the scattering length a_{sc} [22]. Remarkably, this size of the bound state is much larger than the range of the potential. Thus, these bound states are also called halo molecules. Such loosely bound halo states exist also in nuclear matter, as for example in ^{11}Li [41].

2.3.3. Mean-Field Interactions

The microscopic interaction potential between alkalies is of van-der-Waals type and thus always attractive. However, for the effective low energy interactions parametrized by the scattering length a_{sc} this is not the case. The mean field interaction energy shift a particle obtains in a medium of density n is [36]

$$E_{\mathrm{int}} = \frac{4\pi\hbar^2 a_{\mathrm{sc}}}{\mu_r} n = gn, \tag{2.19}$$

where the interactions are repulsive (attractive) for positive (negative) scattering length and g is an effective coupling strength. For a (bosonic) scatterer identical to the medium the interaction shift is twice as large, due to symmetrization of the wavefunction.

2.3.4. Scattering in 2D

Since all experiments presented in this thesis are performed in a quasi-2D geometry, we summarize the most important results for 2D scattering. More details can be found in the following review articles [13, 38]. We will only consider the case of an attractive short range potential, as this yields a very accurate description of the physics investigated throughout this thesis. As in 3D it is convenient to expand the scattering amplitude $f(k)$ in spherical waves [38]

$$f(k) = \sum_{l=0}^{\infty} (2 - \delta_{l0}) \cos(l\theta) f_l(k) \tag{2.20}$$

The scattering amplitude for the different partial waves in 2D is given by [38]

$$f_l(k) = \frac{-4}{\cot \delta_l(k) - i}. \tag{2.21}$$

We again are interested in low energy scattering and thus only obtain a non-trivial phase shift for $l = 0$. Expanding the s-wave phase shift for low momenta yields

$$f_0(k) = \frac{-4}{\frac{2}{\pi} \ln(k a_{2D}) - i}, \tag{2.22}$$

with the 2D scattering length a_{2D}. Note that in 2D the s-wave scattering amplitude becomes zero in the small momentum limit, as opposed to 3D, where it converges to the scattering length. Nevertheless, the 2D s-wave scatting cross-section given by $\sigma_0 = |f_0(k)|^2 / 4k$ diverges, as opposed to the results for higher partial waves, where not only the scattering amplitude but also the cross-section converges to zero at low momenta [38]. Thus, as in 3D only s-wave interactions are important at low temperatures. In 2D the scattering length a_{2D} is always positive and there is no unitary limit, where the scattering of the particles depends solely on their wavelength and the system is scale invariant.
This is an interesting point, because when looking at the Hamiltonian of the two-particle problem for contact interactions

$$\hat{H} = -\frac{\hbar^2}{2m} \nabla^2 + \frac{\hbar^2 g}{2m} \delta^{(2)}(r), \tag{2.23}$$

one finds from dimensional analysis that the interaction strength g is simply given by a number and the system appears to be scale invariant. However, when naively quantizing the theory this results in diverging scattering amplitudes and the interactions have to be renormalized [38]. Most conveniently this is done by introducing a finite energy bound state, which exists for any attractive interaction and thus all scattering lengths in 2D. The energy of this bound state is given by [38]

$$E_{\mathrm{B}} = \frac{\hbar^2}{2\mu_r a_{2D}^2}. \tag{2.24}$$

The length (energy) scale associated with this dimer breaks the scale invariance of the Hamiltonian.
The interaction parameter describing 2D scattering is proportional to $-1/\ln(k a_{2D})$ [42, 43] and explicitly depends on the momentum of the colliding particles. As in 3D, the nature of the mean-field interaction in 2D depends on the sign of the interaction parameter and mean-field interactions are attractive for positive $\ln(k a_{2D})$. Note that in 2D the nature of the mean-field interactions can be tuned

by changing the characteristic momentum of the system (as opposed to 3D, where the nature of the mean-field interactions depends on the sign of the scattering length).

Quasi-2D Scattering

All experiments are obviously performed in a 3D world. Reaching a quasi-2D regime can be achieved by tightly confining the particles along one dimension. In the experiment the tight confinement is harmonic and $\hbar\omega_z$ is (much) larger than all other energy scales of the system. Hence, all dynamics along the z-direction are frozen out when the temperature T and the chemical potential μ are smaller than the energy of the first excited state $\hbar\omega_z$. This is the so-called quasi-2D regime, where the dynamics take only place in the plane perpendicular to the tight harmonic confinement and the low energy physics is essentially 2D. Note that in our experiment, the harmonic oscillator length of $l_z \approx 500\,\mathrm{nm}$ is much larger than the van-der-Waals range of approximately 3 nm and locally scattering is always 3D. Nevertheless, the low energy scattering physics can effectively be described using the 2D expressions, where the effective 2D scattering length a_{2D} can be obtained by integrating out the tightly confined direction of the wavefunction. The effective 2D scattering length a_{2D} is connected to the harmonic confinement along the third direction and the 3D scattering length a_{sc} via [13, 38, 44]:

$$a_{2D} = l_z \sqrt{\frac{\pi}{A}} \exp\left(-\sqrt{\frac{\pi}{2}}\frac{l_z}{a_{\mathrm{sc}}}\right), \tag{2.25}$$

where $A = 0.905$ and l_z is the harmonic oscillator length. This holds for scattering energies smaller than the axial confinement energy scale and hence, across a Feshbach resonance.

Importantly, as this renormalization of the scattering includes a second length scale l_z, the energy of the bound state is not directly linked to the 2D scattering length $a_{2\mathrm{D}}$. This is especially the case, when the size of the bound state is (much) smaller than the axial harmonic oscillator length l_z. The quasi-2D bound state energy is given by the implicit expression [38]

$$\frac{l_z}{a} = \int_0^\infty \frac{du}{\sqrt{4\pi u^3}} \left(1 - \frac{\exp(-\frac{E_{\mathrm{B}}}{\hbar\omega_z}u)}{\sqrt{(1-\exp(-2u))/(2u)}}\right). \tag{2.26}$$

This formula interpolates, between the two limiting cases of a 2D and 3D molecule and the obtained bound state energy is shown in Fig. 2.5.

For small negative 3D scattering lengths a_{sc} the binding energy is small compared

to the axial confinement. Thus, the molecule is spread out in the plane transverse to the tightly confined axis and the molecule behaves as a 2D object. Due to the 2D character of the molecule, the binding energy obtained from equation (2.26) matches the result for inserting the 2D scattering length calculated from equation (2.25) into the formula for the 2D binding energy (2.24). Here, the emergence of a bound state is due to the confinement of the particles along the axial direction. In the other limit, where the 3D scattering length a_{sc} is small and positive one obtains a deeply bound 3D molecule. The binding energy is much larger than the axial confinement energy scale $\hbar\omega_z$. Thus, the size of the molecule is much smaller than l_z and the molecule wavefunction contains a superposition of many excited harmonic oscillator states along the tightly confined direction. In this limit the molecule wavefunction is 3D and not affected by the confinement. Here, it is obvious, that using the result for the 2D scattering length together with equation (2.25) does not yield the right energy for the bound state as it is a 3D object. Note, however, that the interaction between a pair of molecules is still 2D. The correct energy of the confinement induced bound state for all interaction strengths is given by equation (2.26).

2.3.5. Two Particles in a Harmonic Trap

For our experiments with mesoscopic samples we have to confine the particles to small volumes in order to have sufficient densities to observe interesting many-body physics. As discussed in the last section the confinement can strongly affect interactions and even result in the emergence of bound states. Here, we will discuss the influence of a harmonic confinement on the interaction of two particles. For a delta type interaction and isotropic harmonic traps in 1D, 2D and 3D this problem was solved in Ref. [45]. An analytic solution for harmonic 3D traps with an axial symmetry was found in Ref. [46]. Recently, also a solution for traps with arbitrary aspect ratios $\omega_x \neq \omega_y \neq \omega_z$ has been found [47]. However, as for our experiment, the case of a round quasi-2D trap with an aspect ratio $\eta = \frac{\omega_r}{\omega_z}$ is relevant, we use the result of Ref. [46], which is simpler to implement.
For a harmonic trap the center of mass and relative motion separate. The Hamiltonian for the center of mass motion is given by a harmonic oscillator (equation (2.1)), with the corresponding eigenstates and eigenenergies. The Hamiltonian for the relative motion is

$$\hat{H}_{rel} = \frac{-\hbar^2}{2\mu_r}\nabla^2 + \frac{1}{2}\mu_r(\omega_r^2 r^2 + \omega_z^2 z^2) + \frac{2\pi\hbar^2 a_{\mathrm{sc}}}{\mu_r}\delta(r)\partial_r r. \tag{2.27}$$

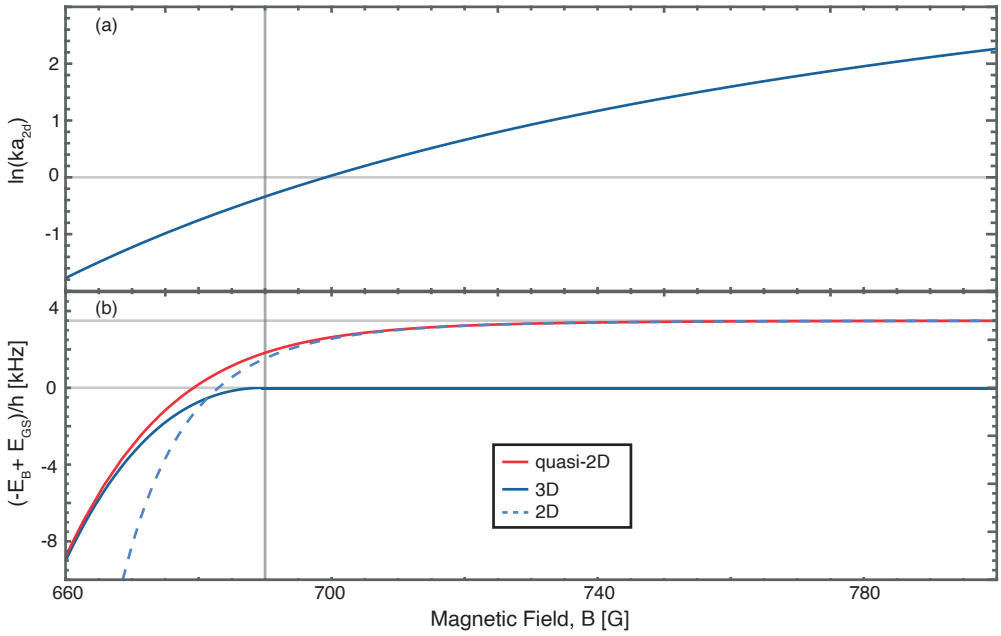

Figure 2.5.: **Bound state energy of a $|1\rangle|3\rangle$-mixture as function of the magnetic field.** (a) Interaction parameter $\ln(ka_{2D})$ for a typical radial momentum of $k = 7.7\,\mu\text{m}^{-1}$ (corresponding to the harmonic oscillator momentum for $\omega_r = 2\pi \times 1\text{kHz}$). (b) Energy of the bound state, offset by the harmonic oscillator ground state energy for the quasi-2D and 2D case. The solution for the quasi-2D case (equation (2.26)), interpolates between the energy of the 3D molecule for small magnetic fields and the the 2D solution calculated from equations (2.25) and (2.24), which is valid for weak attractions at large magnetic fields. The tight axial confinement is a harmonic oscillator with $\omega_z = 2\pi \times 7\text{kHz}$. The Feshbach resonance for the $|1\rangle|3\rangle$-mixture (Fig. 2.4) is at $B = 690\,\text{G}$ (gray line).

Since the contact interactions can only influence states with finite relative wavefunction at $r = 0$, it is clear than only states with zero angular momentum projection along the z-axis obtain an interaction shift. We are interested in the quasi-2D regime, where $\eta = \omega_r/\omega_z < 1$. For integer inverse aspect ratio $1/\eta = j$ the energy levels are given by [46]:

$$\frac{\sqrt{2\pi}\, l_z}{a_{\text{sc}}} = \frac{2\sqrt{\pi}}{j} \sum_{m=0}^{j-1} \frac{\Gamma\left(\frac{\mathcal{E}}{2} + \frac{m}{j}\right)}{\Gamma\left(\frac{\mathcal{E}}{2} - \frac{1}{2} + \frac{m}{j}\right)}. \tag{2.28}$$

Where Γ is the Euler gamma function and all energies are given in units of the axial trapping frequency $\hbar\omega_z$ and $\mathcal{E} = E - E_0$, is the energy measured relative to the ground state of the harmonic oscillator, which has an energy $E_0 = \frac{1}{2} + \eta$.
The energy spectrum for the case of an aspect ratio of $1/\eta = 7$ is shown in Fig. 2.6. Compared to the energy spectrum of interacting particles in free space, the spectrum for trapped particles is discretized. The second consequence of the

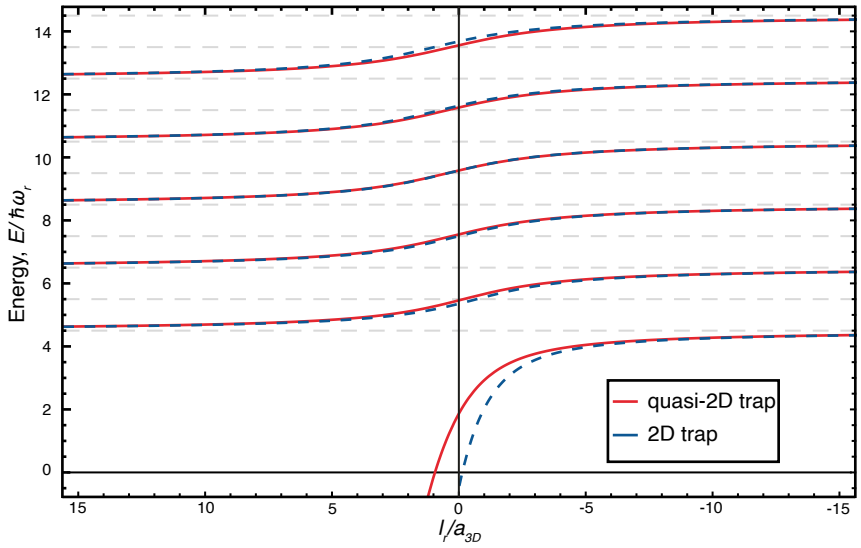

Figure 2.6.: **Spectrum of two harmonically-trapped interacting particles.** The confinement is a quasi-2D trap, with an aspect ratio $\omega_r : \omega_z = 1 : 7$. The spectrum in red shows the result calculated with equation (2.28) in the full quasi-2D potential. The gray dashed lines give the energy levels of the unperturbed harmonic oscillator levels. The result for the quasi-2D case can be compared to true 2D calculations. The result for a true 2D trap is is obtained by first calculating the effective 2D scattering length $a_{2\mathrm{D}}$ (equation (2.25)) and then calculating the energy spectrum of the harmonic 2D trap using $\Gamma\left(\mathcal{E}/2\right) = \ln(l_r^2/a_{2D}^2)$ [45]. To compare to the quasi-2D calculations, we offset the 2D spectrum by the ground-state energy $\hbar\omega_z/2$ of the harmonic oscillator along the z-direction. The 2D spectrum is shown as dashed blue line. The two results show remarkable agreement considering the small aspect ratio of the trap frequencies which results in a ratio of the size the of the wavefunction along the different directions of only $\sqrt{7} \approx 2.7$. The largest deviations are observed for the bound state, where the 2D solution does not take into account the deformation of the z-wavefunction for large interaction and thus predicts a much larger binding energy. Note that the x-axis is flipped, in order to easily compare to the plot for the ^{6}Li Feshbach resonances.

trapping potential is that the energy of the states now explicitly depends on the interaction strength. This can also be easily understood, as a change of the scattering length changes the boundary condition at a relative distance $r = 0$ between the atoms and the energy of the eigenstates in the trap explicitly depends on this boundary condition as it determines the wavefunction curvature. For the infinite homogeneous case the phase shift of the particles at a relative distance $r = 0$ does not change the energy. This is a consequence of the scattering of free particles and of course changes if one considers scattering of particles in a finite size homo-

geneous box,[5] as now changing the boundary condition for the wavefunction at relative distance $r = 0$ together with the boundary condition at the edge of the box changes the wavefunction curvature and hence the energy. From the energy shift of two particles in the (finite volume) harmonic oscillator we also find that the effective interaction is attractive for $a_{\mathrm{sc}} < 0$ and repulsive for $a_{\mathrm{sc}} > 0$, as the energy of the interacting states is lower (higher) for $a_{\mathrm{sc}} < 0$ ($a_{\mathrm{sc}} > 0$) than for the corresponding non-interacting state.
For weak interaction $a_{\mathrm{sc}} \to \pm 0$, the energy levels approach the spectrum of the non-interacting harmonic oscillator, given by $\hbar\omega_z(1/2+\eta(n+1))$ for the n^{th} level. Here and in the following, we only consider states below the first excited state along the z-axis. For all interaction strengths there is a state below the lowest non-interacting state. Again, the confinement results in a bound state for negative scattering lengths, as opposed to the free 3D result, where the bound state only exists for positive scattering lengths. Only even harmonic oscillator states obtain a shift, as these are the only levels, where the 2D harmonic oscillator has eigenstates with $L_z = 0$. On the 3D resonance ($1/a_{\mathrm{sc}} = 0$), the energy of the shifted states is close to the energy of the non-interacting odd harmonic oscillator levels.

Next, we discuss how the confinement affects the binding energy E_{B} of a pair of particles. The binding energy is defined as the difference between the ground-state energy of two particles at a given interaction strength and the ground-state energy of two non-interacting particles in the same trapping geometry (Fig. 2.7). We compare the bound state energies (Fig. 2.7) for the 3D case, the homogeneous quasi-2D case and the additionally radially confined quasi-2D case. We find that for weak attraction (high magnetic fields) the binding energy of the harmonically confined quasi-2D system is much larger than that of the continuous quasi-2D system. In this regime the binding energy is (much) smaller than the radial trap frequency. Hence, the size and thus also the energy of the bound state is strongly affected by the additional radial confinement.
For stronger attraction the size of the pair is comparable to the radial harmonic oscillator length l_r and the radial confinement does not have a large effect on the binding energy and the bidding energy calculated for the two quasi-2D cases coincides.
For very strong attraction (for magnetic fields $B \lessapprox 660\,\mathrm{G}$) the binding energy is larger than the harmonic oscillator energy $\hbar\omega_z$ of excitations along the third

[5] In a box the two-body problem does not separate in relative and center of mass motion. But one can place an (infinitely) heavy scatterer at the center of the box and study the change of the wavefunction of the second particle when changing the scattering length.

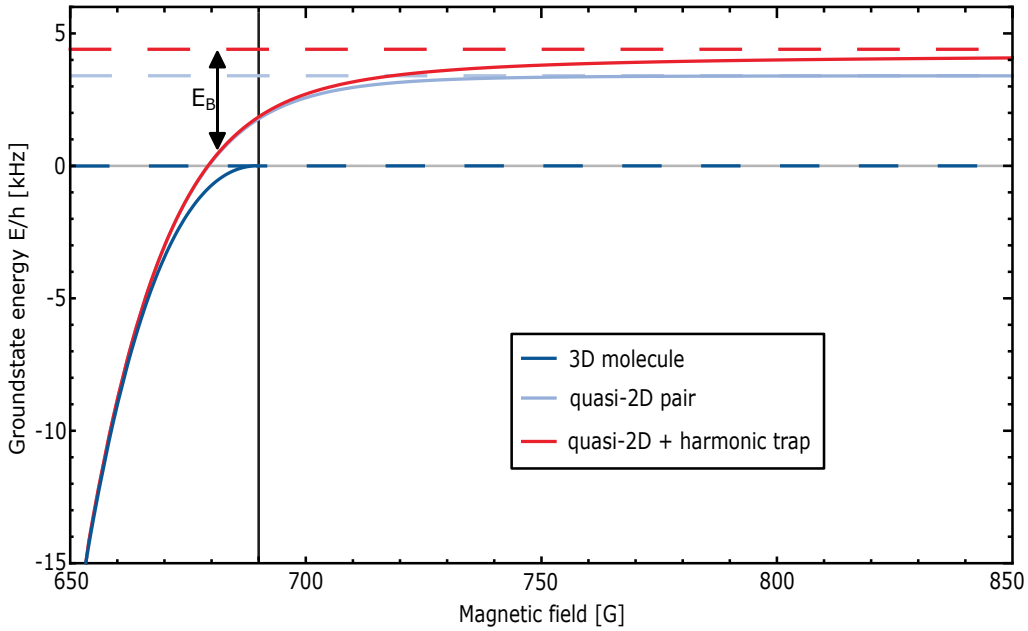

Figure 2.7.: **Binding energy of two atoms in state $|1\rangle$ and $|3\rangle$ as function of the magnetic field.** The energy of the bound state is compared for different trap geometries and for two particles in 3D without any confinement. In the latter case a molecule only exists below the Feshbach resonance at 690 G. The light blue curve corresponds to a confinement of the atoms along the axial (z-)direction with $\omega_z = 2\pi \times 7\,\mathrm{kHz}$. The red curve gives the energy of the atoms additionally confined in the radial (xy-)plane with a trap frequency $\omega_r = 2\pi \times 1\,\mathrm{kHz}$. The dashed lines indicate the energy of the respective non-interacting ground state. E_B gives the binding energy of the pair.

direction. Thus, the molecule is a 3D object and only weakly affected by the discrete level spectrum of the trap.

2.4. Many-Body Physics

After the discussion of the two-body problem we proceed to more complicated systems and summarize the experimentally relevant properties of fermionic many-body systems. We start with a short overview of the general properties of phase transitions and the associated mode spectrum. This is followed by a summary of the properties of the specific system used in the experiment, i.e. attractively interacting two-component fermions. After a general overview more details on the special case of the BEC-BCS crossover in a harmonic trap are given.

2.4.1. Phase Transitions

On a macroscopic scale matter is classified by its phase. The essential properties of a material change only slightly within a phase and drastic changes of the behavior are related to transitions between different phases. Phase transitions can be classified by the form of the free energy. A phase transition is of n^{th} order if the n^{th} derivative of the free energy is discontinuous [33]. First order transitions involve latent heat. Higher-order phase transitions do not involve latent heat and are referred to as continuous phase transitions. Here, a short summary of the relevant aspects of second-order phase transitions, that are required to understand the measurements presented in this thesis, is given. In general, the physics of phase transitions is described using the framework of quantum field theory. For our purpose it suffices to consider a mean-field picture. More details on the full theoretical treatment can be found in several books (e.g. [4, 5, 31]).
Phase transitions are described in terms of spontaneous symmetry breaking. The ground state in the ordered (or symmetry broken phase) has less symmetry than the underlying Hamiltonian and thus violates (breaks) the symmetry of the system. The different phases can be distinguished by the order parameter, which is zero in the symmetric phase and obtains a finite value in the symmetry broken phase. This finite value of the order parameter breaks the symmetry of the Hamiltonian.
Landau developed an effective phenomenological theory for second-order phase transitions [48], where close to the critical point the order parameter changes continuously. The idea is to guess a low-energy (large length scale) theory, capturing the relevant behavior close to the phase transition. The free energy F, which is linked to the action S of the system by $F = \frac{T}{V}S$, is expanded in powers of the order parameter, where only terms respecting the symmetry of the Hamiltonian are kept. The expansion coefficients are phenomenological and depend on the system properties, like temperature or interactions. This expansion enables us to predict some properties of the system. Since the free energy depends only on the symmetry of the system the predictions are independent of the microscopic details and universal. This phenomenological theory has the advantage, that it does not require a precise knowledge of the microscopic theory. However, the assumption of the physics only being determined by the symmetry of the Hamiltonian is often too strong and there are correction to these predictions. For example, an effective theory for superconductors [49] was developed several years before the correct microscopic description was discovered [50].

In the following, we discuss the experimentally relevant case of a $U(1)$-symmetric Hamiltonian. The order parameter is given by the the macroscopic wavefunction $\Psi(r) = |\Psi|e^{\imath\theta}$. In the symmetry broken phase the order parameter 'picks' a phase θ, which breaks the underlying $U(1)$ symmetry. The static part of the action to lowest order in $\Psi(r)$ is [5, 51]:

$$S_{\text{static}}[\Psi] = \int d^3r \left(\xi^2|\nabla\Psi|^2 - r|\Psi|^2 + \frac{u}{2}|\Psi|^4\right). \tag{2.29}$$

The constants ξ, r and u depend on the microscopic theory and are a priory unknown in our effective theory treatment. However, we know that $u > 0$, as the action has to be bound from below. The expectation value of the order parameter $\langle\Psi\rangle$ is found by minimizing the free energy ($\frac{\partial F}{\partial \Psi} = 0$). The ground state of the system (minimum of the action) depends on the sign of r. We obtain $\langle\Psi\rangle = 0$ for $r < 0$ and $\langle\Psi\rangle = \sqrt{\frac{r}{u}} = \Psi_0 = n_0$ for $r > 0$, where n_0 is the condensate or superfluid density. Hence, the phase transition happens at $r = 0$ and for $r > 0$ the finite value of the order parameter breaks the $U(1)$ symmetry. Note that as the phase of the order parameter is arbitrary, we have set it to zero here.
From the free energy, we can calculate different (thermodynamic) quantities. For example, if the temperature dependence of the expansion coefficients is known, we can compute the heat capacity [4, 31]. Also correlation functions of the order parameter can be calculated and one finds that the correlation length diverges close to the critical point. It is even possible to extract the critical exponents of how the correlation length diverges, when approaching the critical point [4]. However, as already mentioned above, in Landau theory the exact values of the exponents depend only on the symmetry of the problem, which results in wrong predictions. To obtain better values for these quantities, fluctuations have to be considered and one has to connect the effective low-energy description to the underlying microscopic model. A way of systematically doing this is provided by renormalization group theory, where one starts with the microscopic Hamiltonian and integrates out short-length scales one by one until one arrives at an effective low-energy long-wavelength theory to describe the phase transition [4, 52].
We will now take a look at the low energy excitations of the system. The potential for the order parameter is given by $V(\Psi) = -r|\Psi|^2 + u/2|\Psi|^4$ and has in the symmetric phase ($r < 0$) a single minimum at $\Psi = 0$. In the symmetry broken phase the minimum of the potential is at the finite value Ψ_0 and the potential has the famous so-called 'Mexican hat' shape. The potential for both cases is depicted in Fig. 2.8. From the shape of the potential one would expect, that excitations in the normal (symmetric) phase cost finite energy, as the potential has a finite

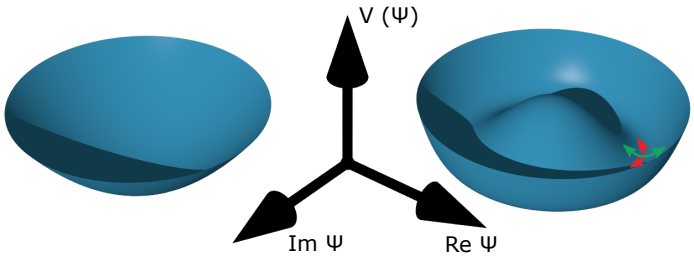

Figure 2.8.: **Effective potential for the order parameter.** In the symmetric phase the potential has a single minimum at $\Psi = 0$ and all excitations cost a finite energy. In the symmetry broken phase the potential has an infinite number of degenerate ground states around the minimum of the Mexican hat potential. There are two types of excitations of the order parameter around its finite average value. The phase excitations (red) along the rim of the hat and amplitude excitations (green) orthogonal to the rim of the hat correspond to the massless Goldstone and massive Higgs mode respectively.

curvature around the minimum. This is indeed true and the excitations have a finite energy gap proportional to r and the gap closes, when approaching the critical point. This mode softening is a general feature of phase transitions [5].
In the symmetry broken phase one would naively expect two modes with quite different properties. An excitation along the minimum of the 'Mexican hat', which costs zero energy, as the potential is flat in this direction. This massless phase mode is a so-called Goldstone mode, which generally arises in systems with a broken continuous symmetry [31, 53]. The second mode corresponds to amplitude changes of the order parameter and due to the curvature of the potential should have a finite mass.
However, in reality things are not as simple and we cannot deduce the excitation spectrum from the time independent static action only, but we have to consider the time dependence of the fields. The low-energy spectrum is obtained by considering Gaussian fluctuations of the order parameter around the potential minimum [4, 51]. The two lowest orders of time derivatives consistent with the $U(1)$ symmetry of the Hamiltonian yield the following equation for the time evolution of the order parameter [51]:

$$K_2\partial_t^2\Psi + \imath K_1\partial_t\Psi = -\xi^2\nabla^2\Psi - r\Psi + u\Psi^3. \tag{2.30}$$

The term proportional to K_2 corresponds to a system with a relativistic dispersion relation and the K_1 term describes a non-relativistic system. This non-relativistic case with $K_2 = 0$ corresponds to a simple ultracold Bose gas and equation (2.30) reduces to the time dependent Gross-Pitaevskii equation [34].

We now consider excitations of the order parameter around the ground state in the symmetry broken phase and expand the wavefunction in terms of amplitude and phase excitation $\Psi - \Psi_0 = \delta\Psi + \imath\delta\phi$. Linearizing the problem yields

$$K_2\partial_t^2(\delta\Psi - \imath\delta\phi) + K_1\partial_t(\imath\delta\Psi - \delta\phi) = \xi^2\nabla^2(\delta\Psi + \imath\delta\phi) + 2r\delta\Psi. \tag{2.31}$$

The phase and amplitude excitations are coupled by the first-order time derivative and are not independent excitations. Hence, for $K_1 \neq 0$ it is not possible to split equation (2.31) into two independent equations for the real and imaginary part. Thus, there is no stable well-defined amplitude excitation of the order parameter in the BEC limit. Fourier transforming gives [51]:

$$(2r + \xi^2k^2 - K_2\omega^2)\delta\Psi + \imath K_1\omega\delta\phi = 0, \tag{2.32}$$

$$(-\xi^2k^2 - K_2\omega^2)\delta\phi - \imath K_1\omega\delta\phi = 0. \tag{2.33}$$

In the non-relativistic case of the Bose gas ($K_2 = 0$ and $K_1 = 1$) this reduces to Bogoliubov dispersion relation [34]:

$$K_1^2\omega^2 = \xi^2k^2u|\Psi_0|^2 + (\xi^2k^2)^2. \tag{2.34}$$

This excitation is massless as expected on general grounds from the Goldstone theorem [53]. For long wavelengths the dispersion relation is linear and excitations correspond to sound modes, whereas at short wavelengths the dispersion becomes particle like $\omega \propto k^2$. There is no independent second stable mode with different dispersion, as amplitude and phase degrees of freedom are coupled by the first order time derivative. For the relativistic dispersion ($K_1 = 0$) on the other hand, we obtain two modes with the following dispersions

$$\omega_G^2 = \frac{\xi^2k^2}{K_2} \quad \text{and} \quad \omega_H^2 = 2r + \xi^2k^2. \tag{2.35}$$

The dispersion relation of the gapless phase mode has a linear dispersion relation $\omega_G \propto k$, as expected for a massless relativistic mode and required by the Goldstone theorem. The amplitude mode has a finite energy gap (mass) of $\omega_H = 2r/\sqrt{K_2}$. The massive amplitude mode is known in particle physics as the Higgs mode [54].

As the observation of an amplitude mode requires a relativistic theory, we might be out of hope that it can be observed in condensed matter systems such as studied in this thesis. However, we will find later, that there exist condensed matter systems, which are well described by a second-order time derivative ($K_2 \neq 0$ and

$K_1 \approx 0$), due to particle-hole symmetry [51]. Indeed, the amplitude mode was observed in several condensed matter systems [55–62]. Even if this additional symmetry is not perfectly fulfilled a small admixture of a first-order time derivative ($K_1 \neq 0$) does not result in a complete loss of the amplitude mode, but only broadens the resonance as is causes the two modes to mix. The higher energy amplitude mode becomes unstable and damped as it can decay into Goldstone modes.
After this discussion of the excitation spectrum of symmetry broken phases, we will move to the system at hand in the experiment and discuss the BEC-BCS crossover.

2.4.2. The BEC-BCS Crossover

Here, we summarize the relevant properties of a many-body system consisting of two-spin components of fermions interacting via attractive s-wave interactions. We first discuss the case of a 3D system and will afterwards summarize the special aspects of the 2D case. We start with the two limiting cases of very strong and weak attraction between the fermions. For strong attraction between the fermions the system is in the molecular BEC (mBEC) limit, where the fermions form repulsively interacting molecules. In the opposite limit of weak attraction the system is at low temperatures described by the so-called Bardeen-Cooper-Schrieffer (BCS) theory. The 3D interaction strength is characterized by the dimensionless quantity $1/k_\mathrm{F}a_\mathrm{sc}$, where k_F is the Fermi momentum. The two limiting cases are reached for $k_\mathrm{F}a_\mathrm{sc} \to \pm 0$, where the different signs correspond to the BEC- and BCS-limit for positive and negative scattering length respectively. The existence of Feshbach resonances in cold atom experiments makes it possible to smoothly connect the two limits and explore the full BEC-BCS crossover. More details can be found in the following review articles and books [4, 5, 22–24].

Molecular Bose Einstein Condensate

In section 2.3.2, we have seen that for positive scattering lengths two particles can form a molecule with binding energy $E_\mathrm{B} = \frac{\hbar^2}{m a_\mathrm{sc}^2}$. Thus, when cooling the system to temperatures below the binding energy, the fermions start to pair and form bosonic molecules by three-body recombination. At low temperatures the system consists of molecules only [63]. In the limit, where all other energy scales (temperature and Fermi energy) are much smaller than the binding energy of the molecule, the molecules can be treated as bosons with no internal structure. The scattering length of these molecules is given by $a_\mathrm{mol} = 0.6\, a_\mathrm{sc}$ [64]. Since the

excitation of the fermionic degrees of freedom requires an energy on the order of the binding energy all fermionic degrees of freedom are frozen out and the low-energy excitations are bosonic.
When cooling the sample further the molecules form a condensate [65–67]. The condensate wavefunction has a well-defined phase and spontaneously breaks the $U(1)$ symmetry of the Hamiltonian. We can easily connect the mean-field theory discussed in the last section, with the microscopic picture of the theory. The parameters of the mean-field description are $\xi^2 = \hbar^2/(2m_{\text{molecule}})$, $K_1 = \hbar$, $r = \mu$ and $u = g = \frac{4\pi\hbar^2 a_{\text{mol}}}{m}$. The chemical potential of the fermions is negative and differs by $-E_{\text{B}}/2$ from the bosonic chemical potential μ, which is positive in the condensed phase. As the Bose gas has no additional symmetries it has a non-relativistic dispersion and is described by the Gross-Pitaevskii equation [34]. Thus, the low energy excisions of the system are Bogoliubov quasi-particles, with a dispersion as given in equation (2.34). Hence, there is no well-defined amplitude (Higgs) excitation mode in the BEC limit.

BCS Limit

It is well known that the ground state of a gapless Fermi gas with attractive interactions is a superfluid for any attraction. However, for weak attraction there exists no two-body bound state in 3D. This raises the question of the origin of the bosonic degrees of freedom required for superfluidity. The problem was solved by Bardeen, Cooper and Schrieffer [50]. They considered the effect of Pauli blocking due to the Fermi sea on the interaction of two particles close to the Fermi surface. They showed that the inaccessibility of states within the Fermi sphere results in a bound state for arbitrarily weak attraction. This scattering problem with a reduced number of available states is similar to the two-particle problem in 2D (see section 2.3.4), where there exists a bound state for any attraction [22]. Due to the assumed weak interactions scattering is only relevant for a small shell of states close to the Fermi surface. These states have an approximately constant density of states, which will become important later. The free energy for the two spin components is [23, 24]:

$$\hat{H} - \mu\hat{N} = \sum_{}(\frac{\hbar^2 k^2}{2m} - \mu)\hat{c}^\dagger_{\text{k}\sigma}\hat{c}_{\text{k}\sigma} + \frac{g}{V}\sum \hat{c}^\dagger_{\text{k}\uparrow}\hat{c}^\dagger_{\text{k'}\downarrow}\hat{c}_{\text{k+q}\uparrow}\hat{c}^\dagger_{\text{k'-q}\downarrow}. \tag{2.36}$$

Where $\hat{c}^{(\dagger)}_{\text{k}\sigma}$, is a fermionic annihilation (creation) operator removing (creating) a particle with momentum k and spin σ and $\hat{N}$ is the number operator. The last (quartic) term describes the attractive ($g < 0$) interactions between opposite spin

particles.
In order to obtain a mean-field solution of the problem one replaces the operator $\frac{g}{V}\sum \hat{c}_{\text{-k}\uparrow}\hat{c}_{\text{k}\downarrow}$, with its finite expectation value Δ [4], which describes the superfluid gap and serves as the order parameter. The choice of this order parameter already tells us that the superfluid is a condensate of 'bosonic' Cooper pairs, which are composed of two fermions with opposite momentum and spin. This transformation removes the four-fermion interaction term in equation (2.36) and gives the quadratic Bogoliubov-de Gennes Hamiltonian (free energy) [23]:

$$\hat{H}_{BCS} = \sum \Psi_{\text{k}}^{\dagger} \begin{pmatrix} \xi_k & \Delta \\ \Delta & \xi_k \end{pmatrix} \Psi_{\text{k}} + \sum \xi_k - \frac{V\Delta^2}{g}. \tag{2.37}$$

The kinetic energy relative to the chemical potential is given by $\xi_{\text{k}} = \frac{\hbar^2 k^2}{2m} - \mu$ and we introduced the Nambu spinor $\Psi_{\text{k}}^{\dagger} = \left(\hat{c}_{\text{k}\uparrow}^{\dagger}, c_{\text{-k}\downarrow}\right)$. This quadratic Hamiltonian is easy to solve, but is not particle conserving. This can be intuitively understood from the coupling of a pair of opposite spin and momentum fermions to a bosonic pair and vice versa via the interactions.
The Hamiltonian is diagonalized by defining new fermionic operators $\alpha_{\text{k}\uparrow} = \cos\theta_{\text{k}}\hat{c}_{\text{k}\uparrow} + \sin\theta_{\text{k}}\hat{c}_{\text{-k}\downarrow}^{\dagger}$ and $\alpha_{\text{-k}\downarrow}^{\dagger} = \sin\theta_{\text{k}}\hat{c}_{\text{k}\uparrow} - \cos\theta_{\text{k}}\hat{c}_{\text{-k}\downarrow}^{\dagger}$ [4]. Note that these quasi-particles are superpositions of a particle and a hole in the original Fermi sea with well-defined spin and momentum. Due to the mixing of particles and holes the dispersion relation (Fig. 2.9 (a)) splits in two branches. The energies of the branches are $\pm E_{\text{k}}$, where the lower branch is completely filled and the upper branch is empty. The dispersion relation of the quasi-particle excitations is given by [4]

$$E_{\text{k}} = \sqrt{\Delta^2 + \xi_{\text{k}}^2}. \tag{2.38}$$

Excitations have always positive energy, as they either create a quasi-particle in the empty upper branch or a hole in the lower occupied branch. Note that the creation of a quasi-particle also changes the number of real particles by one [22]. Thus, the energy of adding or removing a single particle is also given by E_{k}, which has a minimum gap of Δ at the Fermi surface ($\xi_{k_{\text{F}}} = 0$). Exciting the system at constant particle number, however, requires two quasi-particle excitations and thus costs an energy $2E_{\text{k}}$. So staring from a gapless non-interacting state turning on an arbitrarily small attractive interaction creates a gapped state. The minimal excitation energy is given by the superfluid order parameter. These minimal energy excitations have a finite momentum due to the underlying Fermi sea. The gap and hence the binding energy of pairs is exponentially small in the interaction strength. The value of the superfluid gap is self-consistently determined to be [24]:

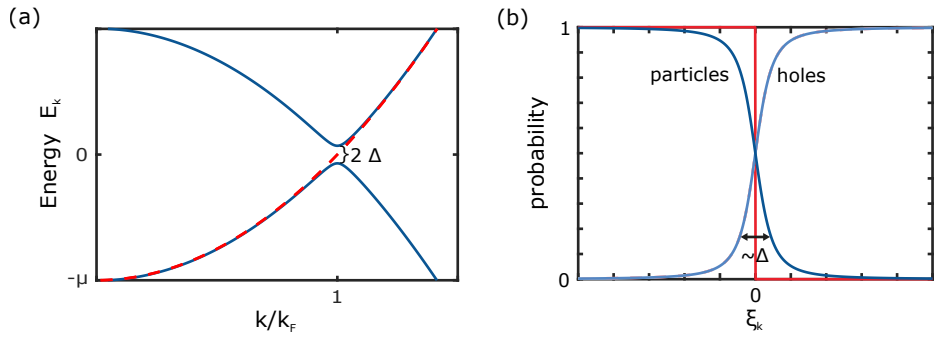

Figure 2.9.: **Particle and hole character of different momentum states in BCS theory.** (a) Fermionic dispersion relation for the non-interacting gas (red) and in BCS theory (blue). (b) The occupation probability of states with energy ξ_k for the non-interacting Fermi gas is given by a step function(red). For weakly interacting systems the occupation probability (blue) of states close to the Fermi surface smoothly goes from 1 to 0 and the Fermi surface is smeared out, by interactions. The dark blue curve shows the result for the occupation probability within BCS theory given by $\sin^2\theta_k$. Comparing the hole and the particle occupations one can see that BCS theory has a particle hole symmetry close to the Fermi surface.

$$\Delta = \frac{8}{e^2} E_F e^{\pi/2k_F a}. \tag{2.39}$$

The ground state of the interacting system contains no quasi-particle excitations and is annihilated by all $\alpha_{k\sigma}$. This is the famous BCS state [4, 50]

$$|BCS\rangle = \prod_k \alpha_{k\uparrow}\alpha_{k\downarrow}|\Omega\rangle = \prod_k (\cos\theta_k + \sin\theta_k\, \hat{c}^\dagger_{-k\uparrow}\hat{c}^\dagger_{k\downarrow})|\Omega\rangle\,. \tag{2.40}$$

It gives the ground state wavefunction in terms of the original fermions, where the amplitude prefactors are determined by $\sin^2\theta_k = (1 - \frac{\xi_k}{E_k})/2$ and $|\Omega\rangle$ is the vacuum of the original fermions. The probability of a state being occupied by a fermion is given by $\sin^2\theta_k$, which is 1 for states deep within the Fermi sea and 0 for states far outside the Fermi sea. The occupation probability is plotted in Fig. 2.9 (b). The interactions smear out the Fermi surface and the occupation probability is smoothly going from 1 to 0, as opposed to the zero interaction case, where the occupation probability is a step function at zero temperature. The attractive interactions mix higher lying initially unoccupied momentum states into the ground state to make optimal use of the attractive interaction to lower the overall energy.

This is similar to what we have discussed for the two-body problem, where higher lying momentum states are admixed to form a molecule and lower the overall en-

ergy. Note that the BCS Hamiltonian (2.37), is symmetric under the exchange of particles and holes. This relies on the constant density of states in a small region around the Fermi surface. This assumption is justified, as long as interactions are small and paring only affects states in a small shell around the Fermi surface. In BCS theory this is well fulfilled, as the gap is exponentially small.

The BCS spectrum shown in Fig. 2.9 (a) is gapped. However, on general grounds we would expect a gapless Goldstone mode due to the breaking of the $U(1)$ symmetry in the superfluid phase [53]. This observation of a gapped spectrum is due to the fact that so far we only considered the fermionic degrees of freedom and ignored the excitations of the superfluid order parameter. The action of the order parameter is obtained by promoting the superfluid gap Δ in equation (2.37) to a bosonic operator and integrating out the fermionic degrees of freedom [4]. Expansion of the resulting action up to fourth order in the gap gives the famous Ginzburg-Landau equation (2.29). In the BCS limit the time dependence of the fields is second order ($K_2 \neq 0$ and $K_1 = 0$) due to particle-hole symmetry [68]. Thus, we expect both a massless Goldstone mode and a massive amplitude mode.[6] The dispersion relation of the sound mode is $\omega_G = v_\mathrm{F}/\sqrt{3}\,k$, where v_F is the Fermi velocity [22, 69]. The sound mode is well defined only for momenta, such that its energy is lower than the onset of the single particle continuum and it becomes strongly damped for larger momenta [23]. The massive amplitude/Higgs mode has a gap of $\omega_H = 2\Delta$ [51, 70, 71]. In the particle–hole symmetric case the amplitude mode is stable against the decay into Goldstone modes. However, the energy of the amplitude mode coincides with the onset of single particle excitations (see equation (2.38)). This immersion of the amplitude mode in the single particle continuum offers additional decay channels and can possibly result in an overdamping of the excitation.
If the amplitude mode exists at all and the cases in which it is stable are discussed at length in several theory publications (see e.g. [51, 70–75]). An example for a solid state system, where the Higgs mode exists as a well-defined excitation is a weakly interacting superconductor with additional charge-density wave order. Here, the charge-density wave shifts the single particle spectrum upwards such that the Higgs mode is not immersed in the single particle spectrum and becomes a well-defined excitation [51, 70, 75] as observed in experiments [55].
In Ref. [71] the complex dispersion relation (including damping) and the quasi-

[6] The massless Goldstone modes exists only for the neutral BCS superfluid discussed here. In (charged) superconductors the charge of the electrons results in coupling to electromagnetism, which is a $U(1)$ *gauge* symmetry. This coupling of the order parameter to the gauge field gives the Goldstone mode a finite mass by the Anderson-Higgs mechanism [54, 69].

particle residue of the amplitude mode have been calculated in the whole BEC-BCS crossover. In the BCS-limit, the amplitude mode exists as a damped excitation inside the single-particle continuum [71]. For increasing interactions (that is in the crossover region discussed below) the single particle gap E_k is pushed to larger energies than the energy of the amplitude mode, but here particle-hole symmetry is violated and the amplitude mode couples to the massless Goldstone mode. Thus, in this region the amplitude mode is also damped, but, nevertheless, gives rise to an excitation peak [71, 76]. For negative (fermionic) chemical potential, i.e. in the BEC limit, there exists no amplitude mode as expected and only the sound mode remains. Experimentally, the amplitude mode in the BEC-BCS crossover was studied in [62], where it was found to be a strongly damped excitation for all accessible interaction strengths.
After a brief discussion of the crossover region, we will summarize the properties of trapped BCS systems. There, we will find that the modified single-particle spectrum in the trap can stabilize the amplitude mode of the order parameter.

The Crossover and the Unitary Fermi Gas

Using a Feshbach resonance offers the possibility to tune the scattering length and thereby connect the two limiting cases of a molecular BEC and a fermionic BCS superfluid. Already before the experimental realization in ultracold quantum gases, it was shown that these two limiting cases are smoothly connected and the system is superfluid for any attraction [19, 77].
For weak attraction the system is a BCS superfluid, consisting of pairs of opposite momentum, which are much larger than the interparticle spacing. Upon increasing the attraction the pair binding energy increases and the pair size shrinks, until the attraction is so strong that the pairing energy is the largest energy scale of the system and the ground state is a molecular BEC. Thus, there is a region in the crossover where the pair size is comparable to the interparticle spacing and the system is a strongly interacting resonance superfluid [22].
For increasing interactions larger parts of the Fermi sphere are influenced by the interactions until it is completely washed out and the chemical potential becomes negative (at $1/k_\mathrm{F}a_\mathrm{sc} = 0.41$) [78]. The strongly interacting crossover region[7] is reached for $1/|k_\mathrm{F}a_\mathrm{sc}| \lessapprox 1$. In this region the critical temperature for the transition to the superfluid is largest indicating the increased stability of the superfluid in the presence of strong interactions [23].
For diverging scattering length ($1/k_\mathrm{F}a_\mathrm{sc} = 0$) the only remaining scale of the sys-

[7] The fermionic character of the systems limits three-body losses and the system is stable.

tem is the Fermi momentum. Thus, the unitary Fermi gas is scale invariant like the ideal gas and the physics is the same on all length scales. More formally upon changing the length scale $x \to \lambda x$ the Hamiltonian transforms as $\hat{H} \to \hat{H}/\lambda^2$. The scale invariance allows to make strong predictions about the systems properties. For example, all thermodynamic quantities are described by universal functions [25]. This symmetry also determines the dynamics of the system [79] and, for an isotropic harmonic trap, gives rise to a breathing mode frequency of exactly twice the trap frequency [25, 80, 81]. A deviation from this value for the breathing mode frequency, thus signals a breaking of the scale invariance. Note that in the 3D case the system has to be fine tuned to a special point (unitarity), whereas in two dimensions the classical theory is scale invariant for any interaction, as discussed above [80]. However, in 2D this symmetry is anomalously broken in the quantized theory, as for example seen from the finite energy bound state in the quantized theory. This anomalous breaking of the scale invariance in 2D results in interaction dependent shifts of the breathing mode away from twice the trap frequency [82] as observed in experiment [83, 84].

2.4.3. Finite Temperature

After the discussion of the ground state properties, we will give a brief overview of the finite temperature properties. In the mBEC limit the critical temperature T_c for the transition into a superfluid is nearly constant and given by the value for an interacting BEC [22]. Here, the thermal low-energy excitations are molecules occupying excited motional states and above the critical temperature the system is a thermal Bose gas. The critical temperature increases inside the crossover region, where excitations both contain bosonic and fermionic degrees of freedom. In the BCS limit the excitations at low temperatures are fermions excited across the superfluid gap. Thus, the energy scale before supefluidity is lost should be comparable to the zero temperature gap. This is indeed the case and the critical temperature is given by $k_B T_c \approx 0.57\,\Delta$ in the BCS limit [4]. Thus, in the BCS limit the critical temperature is exponentially small, which limits the experimental accessibility of a BCS superfluid in cold atom systems. In BCS theory pair formation and the transition to a superfluid happen at the same temperature [50] and above the critical temperature the system at weak attraction is described by a Fermi liquid.

2.4.4. BEC-BCS Crossover in 2D

We have discussed the BEC-BCS crossover in 3D, however, as our experiments are performed in quasi-2D, we quickly review the main features and differences of the 2D case. The Mermin-Wagner theorem states that there is no spontaneous symmetry breaking for continuous symmetries at finite temperature in 2D [85]. This is due to the mode spectrum of Goldstone modes, which would destroy any true long-range order at finite temperature in 2D. However, there is still a phase transition to a superfluid with quasi-long-range order at low temperatures [17, 18]. This so-called Berezinskii–Kosterlitz–Thouless (BKT) phase transition is a topological phase transition. It can be understood as a vortex[8] binding-unbinding transition [86]. Above the transition temperature free vortices proliferate in the system and destroy any quasi-long range order. At the transition point free vortices of opposite winding bind to pairs, whose dipole phase field does not destroy the phase coherence at long distances [86]. The superfluid density jumps to a finite universal value at the critical temperature [87], but all other thermodynamic observables are smooth. In the superfluid phase the mode spectrum of the phonon destroys the true long-range order. The first-order correlation function $g_1(r) = \langle \Psi^\dagger(r)\Psi(0)\rangle$ has the following functional form [86]

$$g_1(r) \propto e^{-r/\xi} \qquad \text{for } T > T_c, \tag{2.41}$$

$$g_1(r) \propto r^{-\eta} \qquad \text{for } T < T_c, \tag{2.42}$$

for large distances. Above the transition the first-order correlations decay exponentially with distance, whereas at low temperatures the correlations decay only algebraically with distance. The exponent η of the algebraic decay of the correlations in the superfluid phase is linked to the superfluid phase space density and has a universal critical value of $\eta_c = 0.25$ at the the transition temperature T_C [86].

In addition to this absence of true long-range order at finite temperature, there exists a two-body bound state for any attraction in 2D (section 2.3.4) and its binding energy E_B can be used to characterize the interaction strength. Nevertheless, there is a BEC-BCS crossover in 2D. For very weak attraction the two-body bound state, with energy $E_\mathrm{B} \ll E_\mathrm{F}$ is irrelevant compared to the BCS superfluid gap $\Delta = \sqrt{2E_\mathrm{F}E_\mathrm{B}}$ and pairing is due to Cooper pairing [38]. The relevant crossover (interaction) parameter in the 2D is $\ln(k_\mathrm{F}a_{2D}) = \ln\left(\sqrt{2E_\mathrm{F}/E_\mathrm{B}}\right)$ [38]. The interaction parameter compares the interparticle spacing $d \propto 1/k_\mathrm{F}$ to the size of the

[8] A vortex is a topological defect with a phase winding of $\pm 2\pi$ of the wavefunction around its core.

two-body bound state $\sim a_{2D}$. The BEC limit corresponds to $\ln(k_\mathrm{F} a_{2D}) \ll -1$ and thus tightly bound molecules, which are much smaller than the interparticle spacing. In the opposite BCS limit the pair size is much larger than the interparticle spacing and $\ln(k_\mathrm{F} a_{2D}) \gg 1$. When the pair size is comparable to the interparticle spacing, i.e. $\ln(k_\mathrm{F} a_{2D}) \approx 1$, the system is in the strongly interacting crossover region [38].

2.4.5. BCS Theory for Trapped Fermions

In section 2.4.2 it was shown that the ground state in the BEC-BCS crossover is a superfluid for any attraction. This is due to the finite density of states at the Fermi surface and the gapless spectrum of the underlying non-interacting system. When considering interactions on top of a non-interacting system with a single-particle gap at the Fermi energy this behavior changes. The single-particle gap adds another energy scale to the system. In order to lower the energy of the system by forming pairs, the interactions have to admix higher lying single particle states (as for BCS theory). However, for the gapped system these states have a finite energy gap and their admixture is energetically costly in contrast to the case for a gapless state. This was first investigated for the case of superconductivity arising from an insulating host material. In this system a critical interaction strength comparable to the single-particle gap is required for superfluidity [88, 89].

For the rest of the chapter, we will consider ultracold fermions in a harmonic trap, which has been extensively discussed for the 3D case [26, 90–92]. We only summarize the experimentally relevant properties of trapped isotropic 2D systems at zero temperature, where we follow the discussion of Ref. [27, 28]. For a round harmonic trap, there exist two different cases: If the Fermi energy coincides with the energy of a harmonic oscillator shell, this shell is partly filled and the single-particle spectrum is gapless. These are so-called open-shell configurations. If, however, the Fermi energy is placed in between the energy of two shells, the highest occupied energy shell is completely filled. In this so-called closed-shell case the single-particle spectrum has an energy gap of $\hbar\omega$.
Depending of the relative strength of the gap Δ, compared to the harmonic oscillator spacing $\hbar\omega$, the system is in different paring regimes. For $\Delta \gg \hbar\omega$ pairing takes place between fermions of different shells and the system is in the so-called intershell-paring regime of a bulk superfluid. Here, the pair coherence length at the trap center $\xi = k_F/\pi m\Delta$ is smaller than the size of the trap [91] and the trap level spacing plays only a minor role for the dynamics of the order parameter.

Up to now all ultracold atom experiments studying superfluidity have been performed in this bulk superfluid regime. This is due to the fact, that the critical temperature is comparable to the gap at zero temperature [4] and superfluity in the weak pairing regime cannot be reached. For a realistic trapping frequency $\omega \approx 2\pi \times 100\,\mathrm{Hz}$ a gap comparable to the harmonic oscillator level spacing would correspond to a critical temperature of $T_c \approx \Delta/k_B \approx 5\,\mathrm{nK}$, which is colder than what currently can be achieved in ultracold fermionic quantum gases at a sufficiently large density (for $\Delta \ll E_\mathrm{F}$).

For weak attraction and thus a small gap $\Delta \leq \hbar\omega$ the discreteness of the single-particle spectrum is important. Here, the system is in the so-called intrashell-pairing regime, where pairing takes predominantly place between particles in the same shell [92]. In a harmonic oscillator all angular momentum states in a single shell are degenerate and theres is no substructure within the shells. For the 2D case this degeneracy also persists for weak attraction, since in 2D the mean-field Thomas-Fermi interaction potential is also harmonic [27].
In this regime, there is a difference between closed- and open-shell configurations, as the attraction giving rise to paring is weaker than the finite single-particle gap for closed shells. For open-shell configurations the system is superfluid for any attraction. In contrast, for closed-shell configurations pairing is suppressed for weak attraction and there is a critical interaction strength [27]

$$\frac{E_\mathrm{Bc}}{\hbar\omega} = \frac{\gamma + 4\ln 2 + \ln n_F}{2\zeta(2)} \left(\sqrt{1 + \frac{4\zeta(2)}{(\gamma + 4\ln 2 + \ln n_F)^2}} - 1 \right) \propto \frac{1}{\ln n_F}, \qquad (2.43)$$

where ζ is the Riemann zeta function. For the 2D system, we characterize the interaction strength by the energy of the two-body bound state E_B and n_F is the shell index corresponding to the Fermi energy $E_\mathrm{F} = (n_F + 3/2)\hbar\omega$, i.e. there are n_F occupied shells (where the lowest shell corresponds to $n = 0$).
In the second step, we assumed a large Fermi energy ($n_F \gg 1$) and we find that the critical interaction strength approaches zero for a large Fermi energy. This is as expected from the increasing Fermi energy and density of states at the Fermi surface, such that the relevance of the single-particle gap decreases and the ground state is paired for all attraction strengths (apart from a logarithmically small range of interactions).
Nevertheless, for finite but large Fermi energies this results in a normal to superfluid phase transition upon increasing the attraction. As discussed above, this quantum phase transition is accompanied by a mode softening with a gap closing

at the critical point [5]. In the superfluid phase ($E_{\mathrm{B}} > E_{\mathrm{Bc}}$), the gap is given by [27]

$$\Delta = \frac{\omega}{\sqrt{7\zeta(3)}}\sqrt{\frac{\omega}{E_{\mathrm{Bc}}} - \frac{\omega}{E_{\mathrm{B}}} + \zeta(2)\left(\frac{E_{\mathrm{B}}}{\omega} - \frac{E_{\mathrm{Bc}}}{\omega}\right)}. \tag{2.44}$$

The gap closing at the critical point signals the instability of the system towards the formation of Copper pairs. In the trap the Cooper pairs correspond to coherent time-reversed pairs with zero total angular momentum, i.e. a coherent superposition of pairs of two particles with $|L_z, \uparrow\rangle$ and $|-L_z, \downarrow\rangle$ [27].
Remarkably, the trapping geometry stabilizes the amplitude mode of the order parameter against a decay into other modes in the vicinity of the phase transition point [27]. In the superfluid phase the amplitude mode has an energy $\hbar\omega_H = 2\Delta$. For large n_F and an interaction close to the critical point the system is approximately particle hole symmetric, as paring takes predominantly place within a single shell and the number of states in neighboring shells is (nearly) equal. However, even if there is a substantial violation of particle hole symmetry (for small n_F) the trap results in a discrete spectrum of the Goldstone modes with spacing $\sim \hbar\omega$ [80]. This limits possible decay channels of the amplitude mode. Since the Fermi energy lies between two shells, the lowest single-particle excitations require to excite a particle to a higher shell. Their energy is $\sqrt{\omega^2 + 4\Delta^2}$ and, thus, larger than the energy of the amplitude mode [27]. This is different to the open shell case, where there exist pair breaking fermionic excitations within the highest shell and the amplitude mode can decay to these states. The energy of the amplitude mode as function of the interaction strength is shown in Fig. 2.10 (a).

The existence of a phase transition and a well-defined amplitude mode in a controlled system of trapped 2D fermions with an accessible few-body limit allows us to investigate how this collective behavior arises when increasing the system size. This was theoretically investigated in Ref. [28], where, the energy spectrum for $n_F = 1$ and $n_F = 2$, i.e. 6 and 12 particles was obtained by numerically diagonalizing the Hamiltonian. The monopole spectrum they obtained is shown in Fig. 2.10 (a). In the spectrum they observe several excitation branches, that for zero interaction are degenerate and have an of energy of $2\hbar\omega$. This is as expected for monopole excitations, which do no change angular momentum and thus only couple states with the same symmetry. For increasing attraction all monopole modes, but the lowest, increase in energy. This increase in energy is explained by the larger mean-field shift (see section 2.3.3) for the denser ground state. These excitations correspond to excitations of a single particle (Fig. 2.10 (b)).

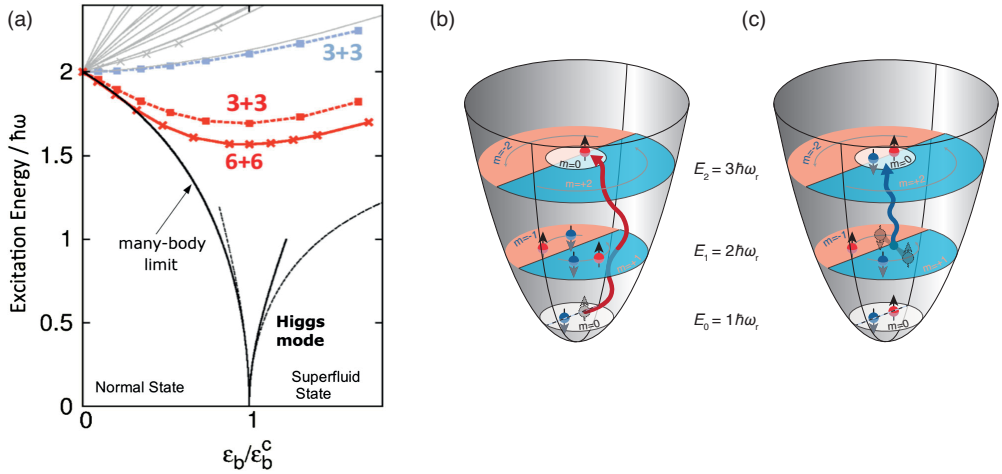

Figure 2.10.: **Numerically calculated monopole excitation spectrum for 6 fermions in a harmonic 2D trap.** (a) The excitation spectrum is shown as function of the interaction strength. The higher lying monopole modes corresponding to the excitation of a single particle monotonously increase with interaction strength. The lowest monopole mode corresponds to the exciation of coherent pairs and shows a non-monotonous interaction dependence. It is the few-body precursor of the amplitude mode of the order parameter (black). The non-monotonous behaviour of the amplitude mode arises from the normal to superfluid phase transition in the thermodynamic limit. The curve for 12 particles (6+6) indicates the deepening of the minimum, when approaching the thermodynamic limit. Note that the interaction axis is scaled by E_B/E_{Bc} such that the minima for different particle numbers fall on the same point. The critical interaction strength E_{Bc} is defined by the minimum of the pair excitation mode and depends on the system size [27, 28]. Sketch of single particle (b) and pair excitations (c) for the 6 atom system. Panel (a) taken from Ref. [28]. Panel (b) and (c) adapted from Ref. [93].

The lowest mode, however, has a non-monotonous interaction dependence and an energy below twice the trap frequency. It consists mainly of the excitation of time reversed pairs of (opposite spin) particles (Fig. 2.10 (c)). The two excited particles are taken from the highest occupied shell and are each transfered one shell up. The excited particles can use all states in the otherwise empty shell and efficiently form a pair even for weak attraction and thereby reduce their total energy (compared to two non-interacting particles in this shell). Hence, the energy of this excitation is decreasing with increasing attraction. However, once the interaction strength is comparable to the single particle gap $\hbar\omega$, it is energetically favorable to form pairs already in the closed-shell ground state by admixing higher lying single-particle levels. Here, the ground state has already significant pair correlations and the energy of the lowest monopole mode is increasing with increasing attraction. This transition from an unpaired state at weak attraction

to a paired ground state at strong attraction is exactly the few-body precursor of the phase transition from a normal to a paired superfluid state in the many-body limit. The pair excitation mode is the few-particle precursor of the amplitude mode of the order parameter discussed above. The finite size of the system prevents a complete gap closing and makes the crossover smooth and differentiable. The minimum energy of the pair excitation mode deepens when going from 6 to 12 particles as expected for the approach towards the many-body limit, where the gap closes completely at the critical point. Note that the minima for 6 and 12 particle fall on the same point in Fig. 2.10 (a). This is due to the fact that in this plot the interaction strength is scaled by the critical interaction strength E_{Bc} for each particle number. It is defined as the interaction strength at the minimum of the pair excitation mode, which in the many-body limit signals the phase transition. As discussed above, the critical interaction strength depends on the system size (equation (2.43)) and approaches zero for increasing system size. For the 6 and 12 particle system the critical interaction strength are $E_{\mathrm{Bc6}} = 0.86\hbar\omega$ and $E_{\mathrm{Bc12}} = 0.78\hbar\omega$ [28].

The amplitude mode of the superfluid order parameter corresponds to changes of the pair density. This pair character is retained in the few-body limit, as can be seen from the large pair correlations in the few-body precursor of the amplitude mode [28]. These theoretical findings demonstrate that already small systems consisting of only 6 particles can show collective behavior and modes, that can qualitatively be understood from many-body theory and phase transitions.

3. Experimental Tools and Setup

In this chapter we give a brief overview of the 'old' experimental setup and how we use it to create and probe large samples of roughly 50000 fermions in a quasi-2D geometry. More details about the setup are found in the respective master and PhD theses [94–98].

3.1. Properties of Lithium

All our experiments are performed with ^{6}Li, which is the lightest alkali. Its electronic ground state is $2\,^2S_{1/2}$. Since it has electron spin $S = \frac{1}{2}$ and nuclear spin $I = 1$ the total spin is half integer and ^{6}Li is a fermion. At zero magnetic-field the electronic ground state splits into a total spin $F = 1/2$ and $F = 3/2$ manifold. In the high field regime, where we perform our experiments the hyperfine states split into two triplets corresponding to $m_s = \pm 1/2$. The states of each triplet correspond to different m_I and are split by approximately 80 MHz. The resulting hyperfine structure as function of magnetic field is shown in Fig. 3.1. We work with the three high-field seeking states with $m_s = -1/2$. Due to the small hyperfine spitting of the ground state the Paschen-Back regime is already reached for magnetic fields on the order of 100 G.
The lowest electronic excited states are the $2\,^2P_{1/2}$ and $2\,^2P_{3/2}$ states, which are coupled to the ground state by the D1 and D2 line respectively. In the experiment we only use the D2 line at 670.977 nm. The excited state has a line width $\Gamma = 5.872$ MHz. Since the excited state hyperfine splitting of 4.4 MHz is smaller than the line width, it cannot be resolved at zero field. For more details we refer to the extensive summary of the properties of ^{6}Li given in Ref. [99].

3.2. Vacuum Chamber and Experiment Control

The creation of an ultracold quantum gas requires a sophisticated sequence of magnetic field as well as laser power and frequency ramps. In our experiment, this sequence is controlled by a real-time processor (ADWIN pro II) with each 16 analog inputs and outputs. This allows us to run digital feedback loops with a

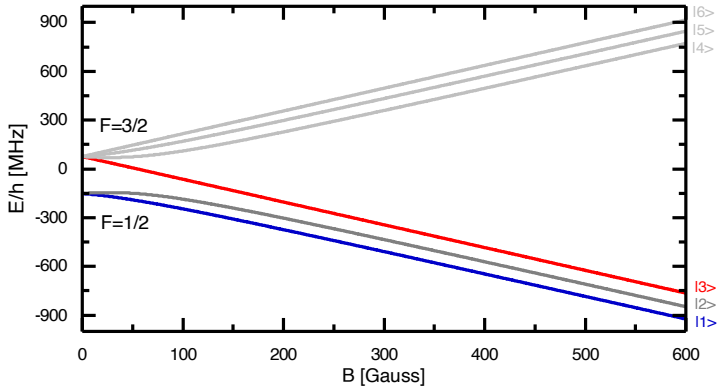

Figure 3.1.: **Electronic ground state energy of ^{6}Li as function of the magnetic field.** At zero magnetic field the electronic ground state is split into two levels with total spin $F = 1/2$ and $F = 3/2$, which are two- and four-fold degenerate respectively. At large magnetic fields, in the Paschen-Back regime, the levels split into three high-field seeking states with $m_s = -1/2$ and three low-field seeking states with $m_s = 1/2$. We label the states according to their energy at large magnetic fields from $|1\rangle$ to $|6\rangle$. Figure adapted from Ref. [98].

cycle time of 2 μs. The 128 digital channels are slightly faster and can be set every 500 ns. The timing table for the sequence is created on an external computer, where we use a LabView interface to communicate with the Adwin and all other devices (such as function generators, cameras, etc.).

The low temperatures $T \approx 100$ nK needed to reach degeneracy in a dilute quantum gas require an extremely good isolation from the environment and all our experiments are performed in an ultra-high vacuum environment. A drawing of the vacuum system is shown in Fig. 3.2. In the main chamber, where all experiments are performed the pressure can be estimated to be below $1.3 \cdot 10^{-11}$ mBar. More details on the vacuum system are found in [94]. The ^{6}Li atoms in the oven are heated to a temperature of $T_{\text{oven}} = 350°$C. This results in a high vapor pressure in the oven and a large flux atomic beam towards the main chamber.

3.3. Dissipative Cooling

The initial cooling steps are performed by scattering resonant light on the D2 line. First, the atoms are slowed in a Zeeman-slower, before they get captured in a magneto optical trap (MOT) inside the main chamber.

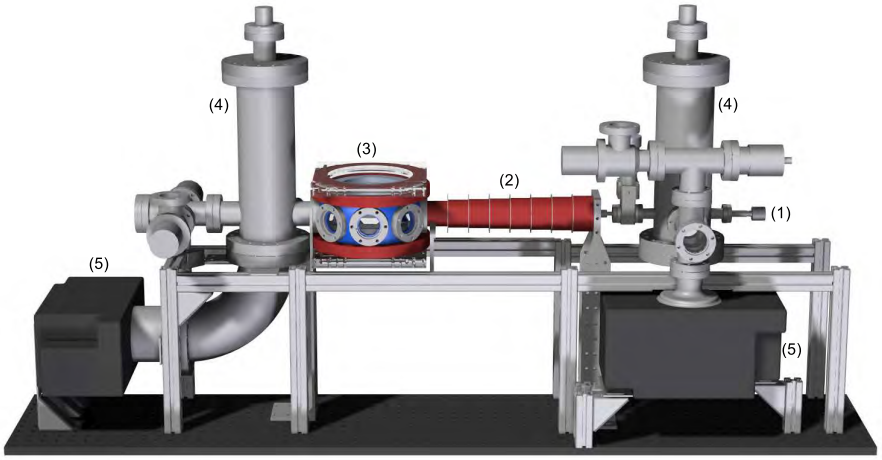

Figure 3.2.: **Drawing of the vacuum chamber.** The heated atoms leaving the oven (1) are slowed by a resonant light in the Zeeman-slower (2). All experiments are performed in the main chamber (3), which offers good optical access by two reentrant viewports with an numerical aperture NA of 0.88 above and below the camber. The vacuum is maintained by titanium sublimation (4) and ion pumps (5). Taken from Ref. [94].

Zeeman-slower We use a circularly-polarized near-detuned light beam counter propagating to the atom beam from the oven. Thus, the atoms only absorb light, which has momentum in the opposite direction compared to their movement. Absorbing a photon transfers a momentum of h/λ onto the atoms, slowing down their movement. Since the spontaneous emission from the excited state is isotropic, the momentum transfer to the atoms due to the emission of photons averages to zero. This slows the atoms on their way from the oven to the main chamber. To compensate the position dependent Doppler shift of the atoms a spatially varying magnetic offset field along the Zeeman-slower is used. This ensures that the slowed atoms are resonant to the light over the whole length of the slower. Note that the Zeeman-slower only slows atoms with sufficiently low initial velocity, as atoms which are too fast are never resonant to the used light. Thus, they have only a small scattering rate with negligible momentum transfer. More details on the setup used in the experiment are found in Ref. [94, 100].

Magneto Optical Trap After the Zeeman-slower, the slow atoms are trapped and cooled in the MOT, whose working principle is, for example, explained in Ref. [101]. The MOT consist of 3 pairs of counter-propagating circularly-polarized light beams. They are slightly red-detuned with respect to the atomic resonance, such that atoms are more likely to absorb light from a beam counter propagating to them. This results in a dissipative force, that cools the atoms. Since the optical

transitions of ^{6}Li are not closed at low magnetic fields, we use two laser frequencies in each beam. They are near-detuned to the transitions for the $F = 1/2$ and $F = 3/2$ hyperfine states of the ground state and are called 'repumper' and 'cooler' respectively.
Spatial confinement is provided by the addition of a magnetic field gradient, that is produced by a pair of coils in anti-Helmholtz configuration. In combination with the near-detuned beams this results in a restoring force trapping the atoms. The dissipative cooling of the atoms using near-detuned light is very fast and efficient. However, due to the presence of resonant light the maximal possible density is limited to an interparticle spacing on the order of the wavelength of the light and the minimal achievable temperature is limited due to the photon recoil. Since we use only a MOT to pre-cool the atoms, the minimal achievable temperature is even higher and given by the Doppler temperature ($T \approx 140\,\mu$K for ^{6}Li) [101]. Thus, in order to reach quantum degeneracy, we have to use different confining and cooling techniques.

3.4. Optical Dipole Traps and Evaporative Cooling

Resonant scattering of light limits the achievable temperature of the atoms. We, thus, transfer the atoms into a far-detuned optical dipole trap, which provides a nearly conservative potential. Before discussing how we use optical dipole traps in the experiment, we provide a quick overview of their working principle.

3.4.1. Conservative Potentials and Light Shifts

Far from any resonance the atom-light interaction is dominated by the dispersive term and the scattering rate is suppressed. The atoms are polarized by the far-detuned light field. Since this is a second order effect the resulting energy shift of the atomic energy levels is proportional to the light intensity I. The scattering rate and energy shift of the ground state of a two-level atom are given by [102]

$$\Gamma_{\mathrm{sc}}(r) = \frac{3\pi c^2}{2\hbar\omega_0^3}\left(\frac{\omega}{\omega_0}\right)^3\left(\frac{\Gamma}{\omega_0-\omega}+\frac{\Gamma}{\omega_0+\omega}\right)^2 I(r), \tag{3.1}$$

$$U_{\mathrm{dip}}(r) = -\frac{3\pi c^2}{2\hbar\omega_0^3}\left(\frac{\Gamma}{\omega_0-\omega}+\frac{\Gamma}{\omega_0+\omega}\right) I(r). \tag{3.2}$$

Here, ω_0 is the frequency of the atomic transition and ω the frequency of the light. For large detuning $\Delta = \omega - \omega_0 \gg \Gamma$ the scattering rate scales as $\Gamma_{\mathrm{sc}} \propto 1/\Delta^2$ and is much smaller than the potential shift $U_{\mathrm{dip}} \propto 1/\Delta$. Therefore, the created

potential is mostly conservative. For the creation of ultracold quantum gases one works with far-detuned traps to reduce off-resonant scattering and heating. However, this comes at the price of requiring large intensities and laser powers to create sufficiently deep traps. The potential shift depends on the sign of the detuning and is repulsive for blue-detuned laser beams ($\Delta > 0$) and attractive for red-detuned beams ($\Delta < 0$). As the potential depth is directly proportional to the intensity it is possible to create (nearly) arbitrary potentials by shaping the light field as will be discussed in chapter 4.1.

3.4.2. Experimental Realization

In the experiment we transfer the atoms from the MOT into a crossed-beam dipole trap (ODT). We turn the repumper MOT beam off shortly before the transfer and all atoms accumulate in the state $F = 1/2$, which creates the required two component mixture of atoms in state $|1\rangle$ and $|2\rangle$, when increasing the magnetic field. Creating a large and sufficiency deep trap for the 'hot' atoms after the MOT stage requires a power of 200 W at the used wavelength of 1068 nm [95, 98]. Since in the conservative potential no dissipative force is present, we have to rely on evaporative cooling to reach temperatures cold enough to access interesting many-body physics [101]. For forced evaporative cooling the potential depth is slowly lowered, in order to lose the most energetic atoms while staying in thermal equilibrium. Thus, high thermalization/scattering rates are required for efficient evaporation.
We increase the interactions, by ramping the magnetic field to $B = 795\,\mathrm{G}$, below the Feshbach resonance at 832 G (Fig. 2.4). At this magnetic field the scattering length is large and positive and at low temperatures the sample consist predominantly out of molecules. By lowering the depth of the ODT by more than 4 order of magnitude, we create a BEC of ~ 100000 molecules, with small thermal fraction [98]. Due to the low density and thus long thermalization times in the large ODT, the evaporation takes approximately 3 s. These samples are the starting point for our experiments on large quasi-2D Fermi gases.

3.4.3. The 2D Trap

Experiments in a quasi-2D geometry require a large aspect ratio of the trapping potential. In our experiment such a trap is created by interfering two 1064 nm laser beams under an angle of 14° (Fig. 3.3). This results in a stack of 2D-layers of traps spaced by 4.4 μm. Each layer has an aspect ratio of $\omega_z/\omega_r \sim 300 : 1$ and axial trap frequencies of up to $\omega_z \approx 2\pi \times 7\,\mathrm{kHz}$ can be reached.

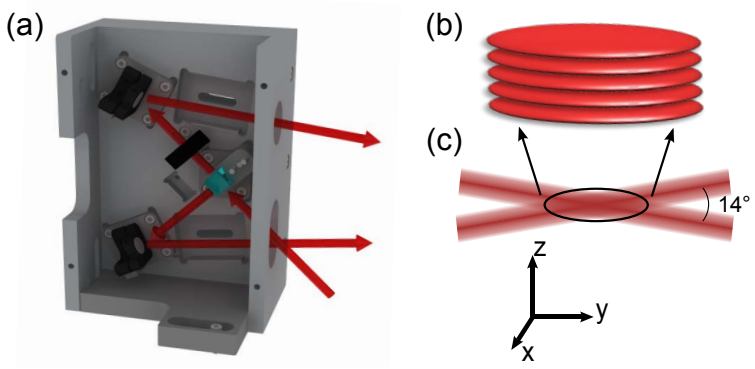

Figure 3.3.: **Drawing of the SWT setup.** (a) White light interferometer used in the experiment to produce the pair of interfering lases beams creating the SWT. The two laser beams cross at an angle of 14° (c). This creates a interference pattern and a stack of quasi-2D traps (b). Figure taken from Ref. [97].

We use a white light interferometer to create the standing wave trap (SWT) [95, 96, 98]. With this setup we achieve a high stability, which results in a small drift of the interference pattern of less than 0.5 μm over 6 days [98].
The quasi-2D sample is created by transferring the mBEC into a single layer of the optical lattice [98]. By compressing the sample in the vertical direction and ramping the magnetic field to $B = 730\,\mathrm{G}$, where the system consist of weakly interacting molecules, over 90 % of the molecules can be transferred into a single layer [98]. The fraction of the atoms in a single layer can be determined by applying a tomographic rf measurement [96, 98]. In recent experiments (after summer 2018) we used a new method, which was developed in the group of Henning Moritz [103], to determine the occupation of the different layers in a single experimental run. This method relies on pulsing on the ODT for at short time at the release of the sample from the SWT. Thereby atoms in different layers obtain a position dependent momentum kick such that atoms initially residing in different layers are clearly separated after a short time of flight expansion.
Loading only a single layer is a prerequisite for well-controlled experiments and probing of the sample, as it avoids averaging over clouds with different temperatures and densities. By a second evaporation step in the quasi-2D geometry we can create a sample of approximately 40000 molecules at temperatures as low as $T/T_F \approx 0.05$ [98].

3.5. Magnetic Fields for State Manipulation

Magnetic Offset Field We can tune the interactions between the different hyperfine states using the available Feshbach resonances (see Fig. 2.4). This requires

magnetic fields of up to 1400 G. These large offset fields are created by a set of small coils ('Feshbach coils') [98]. They are placed slightly further apart than Helmholtz configuration and thus provide an offset-field dependent additional radial confinement ($\omega_r \approx 2\pi \times 10\,\mathrm{Hz}$) for the high-field seeking states [98].

Radio Frequency Fields We use AC-magnetic fields to manipulate the internal state of the atoms. A single-loop coil inside the vacuum chamber is used to drive radio frequency (rf) transitions from state $|1\rangle$ to $|2\rangle$ or $|2\rangle$ to $|3\rangle$. In the large magnetic field regime, where our experiments are performed this requires a frequency of approximately 80 MHz. Since these transitions correspond to flipping the nuclear spin, high powers of up to 100 W are required to achieve Rabi frequencies of $\Omega \approx 2\pi \times 8.8\,\mathrm{kHz}$ [95]. We also use rf transitions to create a $|1\rangle\,|3\rangle$-mixture by a Landau-Zeener sweep transferring the atoms in state $|2\rangle$ to state $|3\rangle$ after the transfer of the atoms from the MOT [104].

3.6. Absorption Imaging

At the end of the experimental cycle, we obtain information about the sample by extracting its density distribution via absorption imaging. This works by illuminating the atoms with resonant light and imaging the shadow cast by the atoms onto a camera. By taking two images, one with atoms and one without atoms, we can extract the optical density of the sample. From the scattering cross-section for the atom-light interaction one can then calculate the column density of the atoms.
In the experiment we have implemented absorption imaging along three different axes. The main imaging is along the vertical direction and thus allows us to extract the full density distribution of the atoms in the quasi-2D geometry while it integrates out the trivial tightly confined direction. For diagnostic purposes, we also have implemented absorption imaging along the two horizontal MOT axes. We use σ_- light resonant with the D2 line. In the high-field region the optical transition for the different hyperfine states are (almost) closed. Since the imaging transitions of the different hyperfine states are roughly split by their energy difference ($\sim$ 80MHz $\gg \Gamma$) our imaging scheme is spin sensitive. A detailed characterization of the absorption imaging used in our experiment is found in Ref. [104].

Momentum Space Imaging As we can only extract information about the density of the sample with our imaging scheme, we have to play a trick to obtain the

momentum distribution of the atoms or molecules. In cold atom experiments one usually uses a time of flight expansion of the atoms in free space to access the momentum distribution. In our experiment, we use a slightly more elaborate method and employ a so-called matter-wave focusing technique [105, 106]. For the expansion the SWT is switched off. This results in a fast expansion of the sample along the initially tight confined direction and a fast drop in density. This together with a fast magnetic ramp of the magnetic field, which converts the sample to weakly interacting molecules [107], reduces the interactions during the expansion. Hence, the subsequent radial dynamics are basically non-interacting and we estimate that less than 10 % of the atoms scatter during the expansion [106].
After this interaction quench, the sample expands ballistically in the remaining radial harmonic confinement of the Feshbach coils. This maps the initial momentum p_0 of the particle to its position after a quarter trap period, without any effects from the initial cloud size. This can, for example, be seen from the trajectory $x(t)$ of a classical particle in a harmonic potential

$$x(t) = x_0 \cos(\omega t) + \frac{p_0}{m\omega} \sin(\omega t). \tag{3.3}$$

This matter-wave focusing technique can be viewed as the equivalent of a (thick gradient) lens in optics, which brings the far field (usually encountered at infinite distance or time of flight) to a finite distance or time.

3.7. Condensation in a Quasi-2D Fermi Gas

After this brief review of the experiment, we summarize some of our findings on quasi-2D Fermi gases obtained with the setup described above. More detail can be found in the respective PhD theses [98, 104, 108] and publications [109–111]. In Ref. [109], we studied the phase diagram of a macroscopic quasi-2D Fermi gas in the BEC-BCS crossover. Using the matter-wave focusing technique, we measured the momentum distribution of pairs (The system is projected onto tightly bound pairs by a fast magnetic field ramp.). We extract the fraction of excess pairs at low momentum, i.e. the number of pairs above the expectation from a thermal distribution. This quasi-condensate fraction is shown in Fig. 3.4 as function of temperature and interaction strength. We observe an increase of the quasi-condensate fraction at low temperatures and a transition into a superfluid state below a critical temperature T_c. Since in 2D there exists a quasi-condensate above the critical temperature [112], we cannot simply take the quasi-condensate fraction to determine the critical temperature. Instead, we extract T_c from the

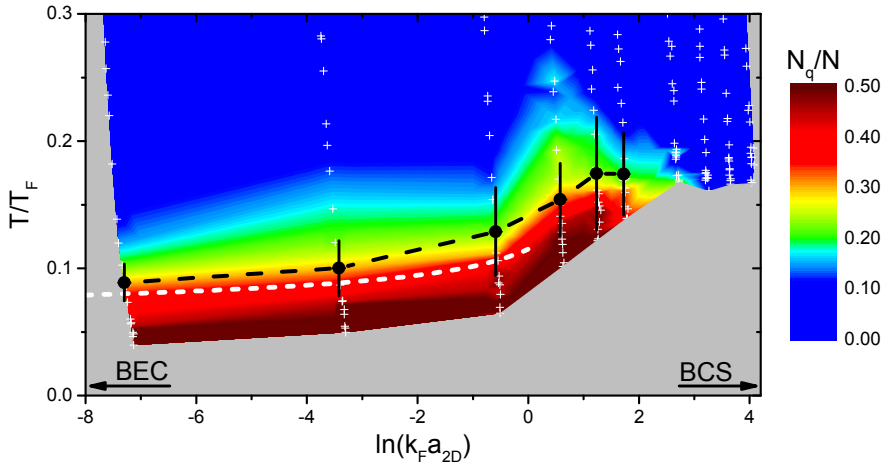

Figure 3.4.: **Experiential phase diagram of the quasi-2D fermi gas in the BEC-BCS crossover.** The quasi-condensate fraction is encoded in the color. The experimentally extracted critical temperature is shown in black and for positive $\ln(k_\mathrm{F}a_{2D})$ agrees well with the prediction for the BKT transition of an interacting Bose gas (white) [113]. In the strongly interacting crossover, where we observe an increase in critical temperature, there is no theory prediction for the critical temperature. Figure taken from Ref. [109].

number of atoms at zero momentum. This quantity is a measure for long-range coherence and shows a rapid increase when lowering the temperature below a certain temperature [109]. In the bosonic limit the critical temperature is nearly constant and agrees with the prediction for the BKT transition in an interacting Bose gas [113]. We observe an increase of the critical temperature in the crossover region. In this set of experiments we could observe superfluidity up to an interaction strength of $\ln(k_\mathrm{F}a_{2\mathrm{D}}) \approx 2$. Observing the decrease of the critical temperature in the BCS limit was not possible with the lowest achievable entropies.

By Fourier transforming the obtained pair momentum distribution, we can accesses the trap averaged first-order correlation function $g_1(r)$ [110]. The obtained first-order correlation functions for different temperatures are shown in Fig. 3.5. Remarkably, the low temperature first-order correlation function is algebraically decaying with distance as expected for an homogeneous system, despite the presence of the trap. According to BKT-theory the exponent of the algebraic decay at the critical temperature should be independent of the interactions and obtain an universal value of $\eta_\mathrm{theo} = 0.25$ [86]. Indeed, we find that the exponent of the algebraic decay at the critical temperature is independent of the interaction strength. However, we observe a larger critical exponent of $\eta_\mathrm{exp} = 1.4$ [110]. This can be explained by the presence of the trap [114]. The observation of a universal exponent shows that the transition is indeed a BKT transition to a 2D superfluid.

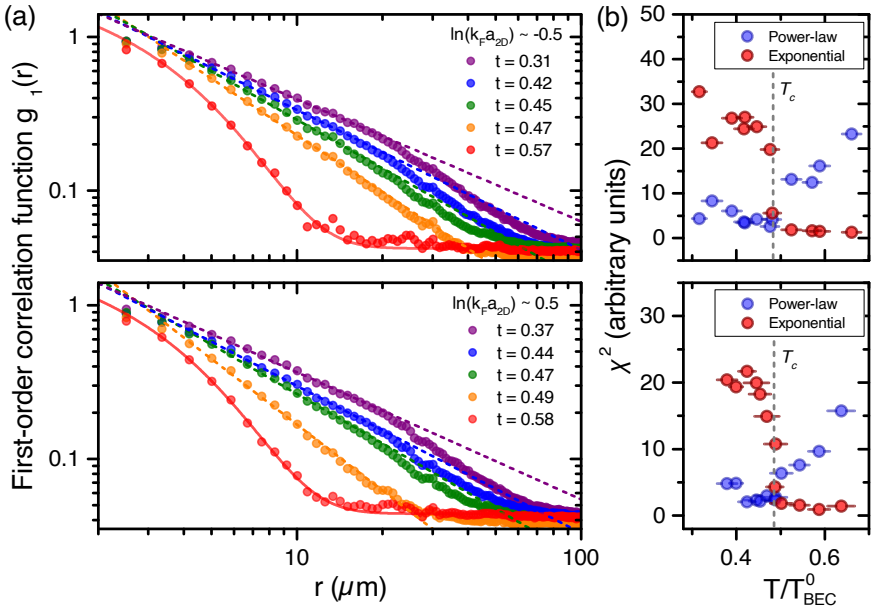

Figure 3.5.: **First order correlation function of the pairs.** (a) Trap averaged first oder correlation function for different temperatures and interaction strengths. For low temperatures, the first order correlation function shows an algebraic decay indicating a transition to a BKT superfluid. Above the transition the first order correlation function is decaying exponentially with distance as expected [86]. (b) χ^2 for the exponential and algebraic fit indicates the change of the shape of $g_1(r)$ as function of the temperature. This can be used to determine the critical temperature T_c. Figure taken from Ref. [110].

3.8. Many-Body Paring in the Normal Phase

After these experiments studying the low temperature phase of the system, we investigated the properties of the normal phase above the critical temperature in Ref. [111]. In the BEC limit, this normal phase consists of deeply-bound bosonic (two-body) molecules (as $k_\mathrm{b}T < E_\mathrm{B}$), whereas in the weakly interacting BCS limit the normal state above the superfluid transition temperature is an unpaired Fermi liquid and condensation and pair formation happen at the same temperature [50]. This raises the questions: How are these two limits connected at high temperatures? Can all pairs above T_c be explained by two-body physics or does a so-called pseudo-gap phase with many-body pairing exist for positive chemical potential [115]?

To experimentally address this problem, we measured the single-particle spectra of the interacting two-component Fermi gas. This is done by a rf transfer of atoms in one hyperfine state to a third (unoccupied) state and subsequent absorption

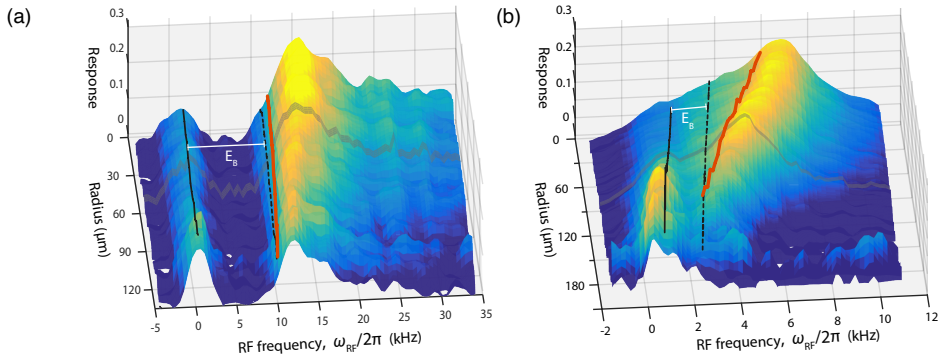

Figure 3.6.: **Observation of many-body paring in the normal phase of the 2D BEC-BCS crossover.** The fraction of transfered atoms as function of the trap radius (density) and rf frequency is shown in the BEC regime $\ln(k_\mathrm{F}a_\mathrm{2D}) \approx -0.5$ and in the crossover $\ln(k_\mathrm{F}a_\mathrm{2D}) \approx 1$ in panel (a) and (b), respectively. The peak position of the free quasi-particle branch is shown by the black line and the onset of the paired branch is given by the red line. In the BEC limit the energy difference between these two branches coincides with the two-body bidding energy (dashed back line) and is independent of the density. In the crossover, however, the energy between the different branches has a strong density dependence and exceeds the two-body binding energy at low temperatures indicating many-body paring. Panels (a) and (b) taken from Ref. [111].

imaging of the transfered atoms. Due to the different interactions for different hyperfine state combinations this results in a shift of the transition frequency compared to the bare frequency. This shift includes mean-field interaction shifts and, for paired particles, the energy required to break the pair. Since the origin of frequency shifts cannot be discerned, when only a single branch is visible, we use a slightly imbalanced sample, where the excess majority particles are unpaired and serve as a reference for the mean-field shift [116]. Then, the frequency difference of the two branches allows us to extract the pairing energy. To avoid averaging the spectra over different degeneracies T/T_F (different densities in the harmonic trap) a pulse short compared to the radial trap frequency is used to obtain a density dependent response.

The fraction of transferred atoms as function of the density and rf frequency is shown in Fig. 3.6 (a) and (b). In the BEC regime (Fig. 3.6 (a)) the energy difference between the two branches corresponding to the paired and excess quasi-particles is independent of the density and coincidences with the two-body binding energy E_B. In the crossover region ($\ln(k_\mathrm{F}a_\mathrm{2D}) \approx 1$), the distance between the two branches increases with density (degeneracy) and at large densities exceeds the two-body binding energy E_B by a factor of ~ 2. This strong density dependence and the large pairing energy compared to E_B shows that the pair

wavefunction is significantly affected by the surrounding medium even in the normal phase. This indicates many-body pairing far above the critical temperature ($T \approx 3\,T_c \approx 0.5 T_\mathrm{F}$) in the strongly interacting regime.

In conclusion, we have studied the properties of a macroscopic quasi-2D Fermi gas in the BEC-BCS crossover. At low temperatures, we observed the transition of the system to a BKT superfluid. Using rf spectroscopy we identified a region of many-body paring in the strongly interacting crossover above the critical temperature. While this allowed us to identify a strongly correlated regime, where the pairing energy depends on the surrounding medium, it does not provide further information about the important correlations in the system and how they arise from a microscopic model.

4. Experimental Tools to Study Mesoscopic Fermi Systems

The experiments presented in the last chapter have significantly improved our understanding of strongly-interacting fermions in 2D. Nevertheless, in the strongly-interacting crossover region a full theoretical description is still missing and it is not entirely understood what the relevant ingredients for a complete description are. A possible way forward is to extract more information from experiments and use the results as input for the development of new theories. However, using the large systems and experimental tools described above it is experimentally very challenging to obtain more complete information such as higher-order correlation functions.
In order to study strongly correlated systems in a more controlled and flexible way, we have performed a major upgrade of the experimental setup. Our idea has been to investigate fermionic systems using a bottom-up approach. Starting from the well understood two-particle limit, we are now able to assemble mesoscopic systems. This allows us to study the emergence of strongly correlated phases and gives access to different observables, which are experimentally not accessible in macroscopic systems. The upgrade has been carried out with the following goals in mind:

- **State preparation** The experiment has to be capable to prepare mesoscopic samples at low entropy, such that interesting phases of matter can be accessed. Ideally, it should be possible to deterministically initialize the system in a well-defined quantum state.

- **State readout** To extract a maximum amount of information about the created state each atom has to be detected with high fidelity.

- **Tunability** The setup should give the flexibility to tune the trapping geometry and interactions, such that different interesting Hamiltonians can be realized.

The remainder of this chapter gives an overview of the experimental tools implemented to achieve these goals. First, we will discuss our scheme to generate arbitrary potentials and its implementation in the setup. Then, the two imaging schemes suitable for the detection of low particle numbers are presented. At the end of the chapter, we review our new abilities to deterministically prepare small atom numbers in the ground state of a harmonic trap and give an example of our ability to manipulate the potential.

4.1. Creating Arbitrary Potentials

In optical dipole traps the potential experienced by the atoms is directly proportional to the light intensity [102]. Hence, by tailoring the light field one can produce arbitrary trapping geometries. In the last years, several groups have started to go beyond standard optical potentials of simple Gaussian traps and lattices created by interfering (at least) two laser beams.

There are two common approaches to generate more complex trapping geometries. One approach is to directly image an amplitude mask, e.g. created by a Digital Micromirror Device (DMD), onto the atoms [117]. This approach is especially suited for large scale, smooth potentials, as the finite resolution of the imaging system smears out small scale variations of the potential. Furthermore, the fraction of utilized light power is directly proportional to the ratio of the created structure size and the total drawing area.

For the generation of small scale structures the more popular approach is to manipulate the phase or amplitude of the light field in the Fourier plane of an objective, which focuses the light on the atoms. This so-called holographic beam shaping allows to create (arbitrary) holograms for trapping the atoms. Recently, both DMD [118] and liquid-crystal spatial light modulators (SLM) [119] have been used to generate tunable holograms for trapping of ultracold atoms. Since this approach allows to control the phase of the light field optical aberrations can be corrected to obtain diffraction limited performance and clean potentials. This makes it possible to realize precise small scale potentials. Furthermore, compared to direct imaging of a DMD, a larger fraction of the total power is utilized, when creating small scale structures using holograms. Since our setup is designed to investigate mesoscopic samples in either arrays of microtraps with tunable geometry or within a single small-scale trap we decided to use holographic beam shaping in the Fourier plane of the objective, that is used to project light onto the atoms (section 4.2.1), instead of direct imaging.

Both DMD and SLM have different advantages and disadvantages. A SLM is made of pixels filled with birefringent liquid crystals. Their refractive index depends on the relative angle between the liquid crystal and light polarization axis [120]. The liquid crystal alignment can be tuned by applying a voltage to the pixels. This changes the phase shift the light experiences when passing the liquid crystal. For the model used in our experiment (X10468-03 from Hamamatsu) the phase can be controlled from 0 to $2\,\pi$ in steps of $\sim 0.01\,\pi$ (216 different input levels values for a phase between 0 and $2\,\pi$). The polarity of the field used to align the crystals has to be switched at a fast rate, as otherwise the liquid crystals start to disintegrate. This switching happens with a frequency of 240 Hz and introduces 'flickering' noise to the trapping potential. Changing the pattern on the SLM is even slower than the switching time due to the relaxation time of the crystals to their new equilibrium position. This results in rise and fall times for the phase shift of up to ~ 80 ms. This makes changes of the trapping potential slow but also smooth.
In contrast, a DMD is an array of micron sized mirrors. Each pixel (mirror) can be in an on or off state. This allows to control both the amplitude and phase of the light field [118]. The binary control, resulting in a large fraction of the mirrors being in the 'off' position, reduces the light utilization efficiency of the generated holograms compared to the continuous phase control of the SLM and can produce larger discretization errors. Once set to the desired pattern the switching of the mirrors can be disabled [121]. Thus, there is no intrinsic unavoidable noise as opposed to a SLM. However, when changing the the displayed pattern all pixels have to be switched off and on again. This switching happens at a frequency on the order of ~ 10 kHz and results in a blinking of the trapping potential at this frequency, when dynamically changing the potential. Distortions at this frequency can result in heating for small scale potentials of light atoms such as ^{6}Li, whose trap frequencies lie in this range. In the end we decided to use a SLM over a DMD for our experiment.

4.1.1. Fourier Optics

Here, we give a short overview of Fourier optics and how we use it in our experiment to create (arbitrary) trapping potentials for the atoms. More details can be found in Ref. [122, 123]. The propagation of light is described by Maxwell's equations, however, in most cases a simplified description can be used. In the experiment we use monochromatic coherent light sources to create the trapping potentials. For the far-detuned trapping light at 1064 nm the atom–light interac-

tion is polarization independent and we can treat the light as a scalar field. This approximation of a scalar light field is also valid for the description of the light propagation, unless very large numerical apertures (angles) are considered and is used in the following. Under these assumptions light emitted by a source $u(\xi, \eta)$ is, at large distances z, described by Fraunhofer diffraction. The far-field light pattern is given by [122]

$$U_f(x, y) \propto \iint_{Aperture} u(\xi, \eta) \exp[-\imath \frac{2\pi}{\lambda z}(x\xi + y\eta)] d\xi d\eta. \tag{4.1}$$

This is equivalent to a Fourier transformation. Since this equation also describes the light field in the focal plane of a lens, the light distributions in the two focal planes of a lens are connected by a Fourier transform [122]. This connection allows us to derive some analytic properties of holographic beam shaping and gives an intuitive picture. Equation (4.1) shows that by using interference it possible to shape the final light field by manipulating only the phase of the initial field. On the one hand this allows us to use holographic beam shaping to create arbitrary trapping geometries. On the other hand this makes the use of monochromatic light for atom trapping susceptible to aberrations of the optical system, which can severely affect the shape of final light distribution and thus the trapping potential.

The phase pattern required to create the desired intensity distribution in the atom plane can be obtained by several different numerical algorithms [123–126]. However, for the measurements in this thesis we only apply simple intuitive potentials, with holograms that can be guessed or calculated analytically. In the experiment, we did not observe any improvement of the potential shape, when using numerically generated phase pattern instead of the simple analytic pattern. This might be due to residual uncorrected aberrations.

The SLM in the experiment consists of 792×600 pixels and is placed in the Fourier plane of the objective focusing the trapping light onto the atoms. Due to the finite filling factor of the pixels, there is always a zeroth order of undiffracted light. To avoid interference of this undiffracted light with the hologram, we shift the hologram position in the atom plane by adding a linear phase gradient to the phase pattern. From equation (4.1) we see that a change of the phase pattern from $u(\xi, \eta)$ to $u(\xi, \eta) \exp(\imath 2\pi\alpha\xi)$ results in the replacement $x \to x + \alpha\lambda f$ in the Fourier coordinates. For such a linear gradient the phase pattern on the SLM is equivalent to a blazed grating.

The pixel size of the SLM results in a discrete sampling of the phase gradient, which causes diffraction to different orders and for small grating periods the

diffraction efficiency in the desired first order decreases [127]. In the experiment, we use a phase gradient of $2\,\pi$ over 16 pixels, which gives a good compromise between a large separation from the undiffracted light and diffraction efficiency into the first order.
The switching frequency of the electrodes controlling the liquid crystal alignment and thus the phase shift is 240 Hz. This switching adds noise on the order of 0.5 % of the intensity [128]. The largest part of the switching noise results in common mode fluctuations of the total intensity of the light field [128], which at this low frequency can be easily suppressed using at PID loop. Furthermore, the fluctuations have a fixed phase relation to the clock of the graphics card displaying the pattern on the SLM. Hence, they can be compensated using a feed-forward, that is triggered on the graphics card output.

4.2. Physical Implementation

The optics setup for the implementation of the SLM in the experiment is shown in Fig. 4.1. The light is provided by a NUFERN fiber amplifier, seeded by a INNOLIGHT Mephisto-S 500 NE. We currently use a power of $P \approx 300\,\mathrm{mW}$ out of the fiber. This power is optimized for requirements of the current experiments and can, in principle, be increased, as the SLM can be illuminated with up to $P = 5\,\mathrm{W}$. The light polarization is cleaned using a polarizing beam splitter (PBS). Since potential manipulations by changing the SLM pattern are slow, we decided to implement an acusto-optical deflector (AOD), which is imaged onto the SLM. The response time of the AOD allows for simple, but fast, manipulations of the potential shape. Changing the frequency of the rf source driving the AOD shifts the angle of the beam in the SLM plane and thus displaces the intensity pattern in the atom plane. In addition, the AOD can be driven with two (or more) rf tones. This results in two beams impinging on the SLM under different angles and therefore creates multiple displaced copies of the hologram in the atom plane. The two copies have different frequencies. Hence, their interference averages out on all time scales relevant for the atoms and the total trapping potential is given by the incoherent superposition of the two displaced holograms. The beam is magnified by the two lenses f_1 and f_2 to a diameter of $\sim 13.6\,\mathrm{mm}$ resulting in a relatively homogeneous illumination of the SLM chip, which has a size of $15.8\,\mathrm{mm} \times 12\,\mathrm{mm}$. The lenses f_3, f_4 and the objective form a 6 f-setup, between the SLM and the atom plane. The first image plane of the hologram is at the focus of the lens f_3. Here we place an aperture , which blocks all light but the desired first diffraction order. This plane is imaged by lens f_4

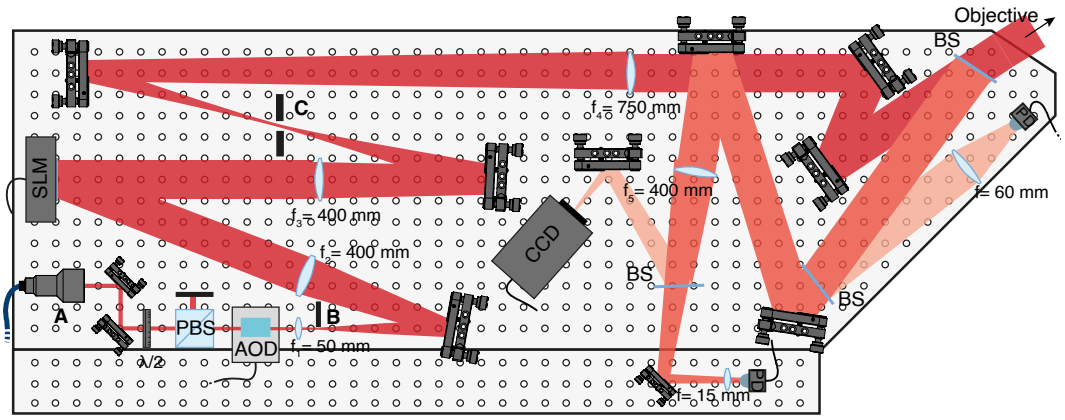

Figure 4.1.: **SLM breadboard of the extension setup.** The light is coupled out from a fiber (A). The polarization is cleaned using a polarizing beam splitter (PBS). Afterwards the beam passes trough an acoustic optical deflector, which is imaged onto the SLM. The undiffracted light is filtered by a beam dump (B). In the first image plane of the SLM (C) an aperture filters all light but the desired diffraction pattern. The lenses f_3 and f_4 form a telescope and image the SLM onto the Fourier plane of the objective on the vertical breadboard. Using a beam sampler (BS) 30 % of the light is split of for diagnostic purposes. This light is distributed between two different photo diodes (PD) and imaged on a CCD camera. Adapted from Ref. [129].

and the objective on to the atoms.

Before the light is transfered to the vertical imaging breadboard 30 % of the light is picked up by a beam sampler and used for feedback purposes. We use two different photodiodes, to stabilize the beam power over 4 orders of magnitude. The CCD camera is used for inspection of the shape of the created potentials. [1] The pattern on the camera is magnified by a factor $f_5/f_{objective} \approx 20$ compared to the atom plane. This magnification is chosen such that the smallest achievable spots created can be resolved on the camera.

The further path of the 1064 nm trapping light on the vertical breadboard is sketched in Fig. 4.2. The beam is focused by the objective on the atoms. The properties of the objective are discussed in detail in the next section. On the vertical breadboard, the infrared trapping light and the resonant beams along the vertical axis are combined/split by a dichroic mirror.

We use two different resonant beams along the objective axis for the MOT and the imaging, respectively. The MOT and imaging beams have orthogonal circular polarization. The two beams are separated using a $\lambda/4$ wave-plate and a PBS.

[1] Most aberrations are caused by the high resolution objective. Hence, the camera image shows large distortions and gives only a rough idea of the trapping potential, when aberrations of the objective are canceled with the SLM.

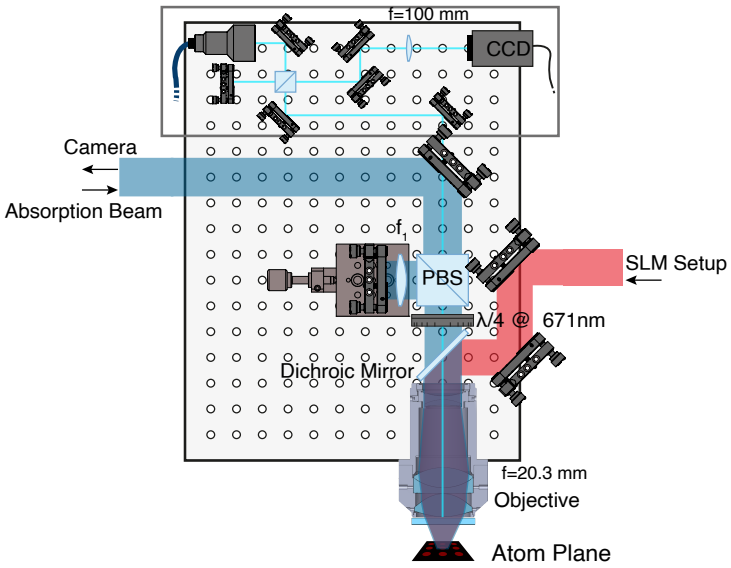

Figure 4.2.: **Vertical objective breadboard of the extension setup.** The 1064 nm light (red) from the SLM board is combined on the dichronic mirror with the resonant 671 nm light used for imaging and the MOT. The MOT and imaging light have different circular polarization and are split on the PBS. The MOT light is reflected from the mirror back onto the atoms. The imaging light is passed to the imaging breadboard. The optics in the gray box are used for aligning the objective [130]. Adapted from Ref. [129].

The MOT beam is coupled out below the vacuum chamber and after passing the atoms it is focused by the objective. It is reflected by the PBS, passes a lens and then is back reflected on itself with a mirror. The double pass of the objective and the lens acts as telescope and produces a collimated retro-reflected MOT beam on the atoms. Note that the lens is tilted to compensate for the astigmatism caused by focusing the beam through the dichroic.
The imaging light passes the PBS to the imaging breadboard shown in Fig. 4.3. We have two possibilities to image the system along the vertical axis. Inserting the flip mirror on the imaging breadboard in the beam path allows us to take absorption images with resonant light from above the chamber. The lens f_2 on the imaging breadboard forms a telescope with the objective creating a collimated beam in the atom plane. The absorption image is taken using optics below the chamber and is in detail explained in Ref. [104]. For the second imaging method, we can take advantage of the large numerical aperture of the objective and collect the fluorescence signal emitted by the atoms, when illuminated from the side. The collected fluorescence is focused on the EMCCD camera on the imaging breadboard. The details of this imaging method will be explained in section 4.3.2.
In order to have an (almost) closed imaging transition we image the atoms on

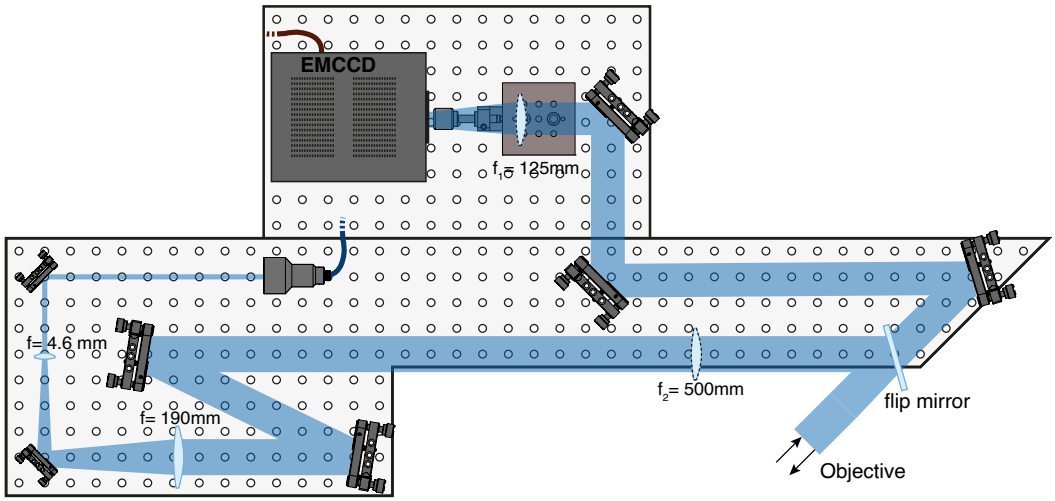

Figure 4.3.: **Camera breadboard.** The setup allows to switch between two imaging schemes. If the flip mirror is in the beam path, the imaging light is focused from this breadboard into the objective such that the beam is collimated in the atom plane. This allows us to use the low resolution absorption imaging discussed in chapter 3.6. Imaging single atoms is done with the flip mirror removed. The florescence from the atoms collected by the objective is imaged on the EMCCD camera. Adapted from Ref. [129].

a σ_--transition in both imaging schemes. Since the polarization of the imaging beams has to be orthogonal to the polarization of the MOT (due to the PBS) and the light is propagating along different directions (downwards in absorption imaging and upwards in florescence imaging), we have to invert the magnetic field direction, when switching between the two imaging schemes. This guarantees that the light propagating along different directions for the two imaging schemes has the correct polarization along the magnetic-field (quantization) axis.

4.2.1. The High Resolution Objective

The central component added to the experiment is a high resolution objective that has been designed by a former PhD student [131]. Due to the large distance of the atoms from the vacuum window it has a focal length of $f = 20.3\,\mathrm{mm}$. The large window of the reentrant viewport allows for a large numerical aperture despite the long focal length. The objective is designed to deliver a diffraction limited numerical aperture (NA) of 0.6. Chromatic shifts are compensated both for 1064 nm and 671 nm. Hence, it can be used to collect resonant light for imaging and to create off-resonant trapping potentials.

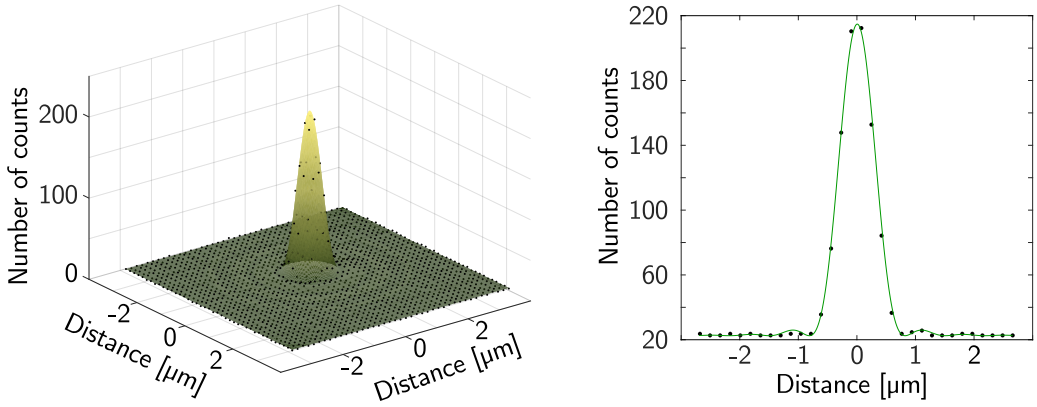

Figure 4.4.: **Pointspread function of the Objective** measured at 671 nm using a gold foil with 650 nm holes. The resolution is $0.86 \pm 0.01\,\mu$m. Taken from Ref. [130].

To test the performance of the objective and to determine its optical axis (which is tilted, with respect to the axis of the objective mount), it was tested outside the experiment setup with a mock-up window. We used a gold foil with an array of 650 nm wide holes, spaced by $20\,\mu$m. After optimizing the objective tilt, we measured the point spread function shown in Fig. 4.4 and found the resolution (maximum to minimum of the point spread function) at 671 nm to be $0.86 \pm 0.01\,\mu$m. This is on one hand considerably larger than then nominal design value of $0.68\,\mu$m, but smaller than the value of $1.01 \pm 0.1\,\mu$m measured in Ref. [132]. This could be due to a better alignment of the objective in our test setup. As we were mainly interested in finding the optical axis and the correct alignment position of the objective we did not measure the resolution at 1064 nm, but the value of $1.21 \pm 0.1\,\mu$m obtained in Ref. [132] serves as a reference. However, the perfect alignment of the objective for 1064 nm light is also not necessary in our case, as we can correct small aberrations using the SLM. The details of the objective test and the protocol used to obtain the correct tilt of the objective inside the experiment can be found in Ref. [130]. The results of the different measurements are summarized in Table 4.1. In the next section we discuss how we use the large numerical aperture of the objective for single atom detection.

4.3. Single Atom Detection

Obtaining information from samples consisting of a few atoms requires to detect each atom with high fidelity. This is not easily possible with the absorption imaging which we used to probe large samples. Thus, we implemented two new

wavelength	nominal values	measurements by [132]		recent measurement
		x-profile	y-profile	
1064 nm	1.08 μm	1.61 (1) μm	1.51 (1) μm	
671 nm	0.68 μm	1.51 (1) μm	1.21 (1) μm	0.86 (1) μm

Table 4.1.: **Comparison of measured and nominal resolution of the objective.** The nominal value is taken from Ref. [131]. The details of the recent measurement can be found in Ref. [130]. The measurement performed in the course of this thesis is closer to the nominal design value than previous measurements [132]. Adapted from Ref. [130].

imaging schemes especially tailored to detect single atoms. The first method relies on recapturing the atoms in the MOT, where we can count the atom number with very high fidelity. However, no information on the spatial and spin distribution is obtained in this method. In the second method, the atoms are illuminated with resonant light for a short time in free space. Thus, only a few photons per atom are collected, but this allows us to obtain information about the spatial distribution and the spin of the atoms.

4.3.1. MOT Imaging

For most of the experiments performed during the course of this thesis it is necessary to count the number of trapped atoms with the highest possible fidelity. This is achieved best by recapturing the atoms in the MOT and collecting the fluorescence signal using a CCD camera (Grasshopper3 GS3-U3-15S5M). Counting of single atoms in a MOT was first demonstrated in Ref. [133] and has been extended to hundreds of atoms [134]. The background limited lifetime of atoms in our MOT was measured in Ref. [94] to be approximately 1300 s. This allows for long imaging times in order to collect thousands of photons per atom. We image the atoms for 1 s which, for samples of less than 20 atoms, limits the probability of having a single atom lost at the end of the imaging process to less than 1.5 %. Capturing atoms from the background gas is even less likely due to the low vacuum pressure of ^{6}Li in the main chamber and because we block the atom beam from the oven using a mechanical shutter.
The effect of background light is minimized by using a large magnetic field gradient of 250 G/cm to compress the MOT. Furthermore, we chose a detuning of about 1.5 linewidth away from the resonance, where the MOT is robust against fluctuations of the laser frequency but the scattering rate is still large. To extract the atom number, we subtract a scaled background image and sum up the signal.

After 1 s we obtain a signal corresponding to roughly 10500 detected photons per atom on the camera. From the quantum efficiency of 60% and the numerical aperture of 0.15 of the imaging system[2] we estimate a scattering rate of the atoms of $\gamma \approx 3.1 \times 10^6 \frac{\text{photons}}{\text{s}}$, which corresponds to $\sim 15\,\%$ of the maximal possible scattering rate.

We compensate for drifts of the fluorescence signal due to changes in the intensity or frequency of the MOT beams by scaling the signal by the mean fluorescence per atom over the last 50 shots. This is done by minimizing

$$\underset{\beta,\text{offset}}{\text{minimize}} \left[\sum_{\text{last 50 shots}} \underset{n=0,\ldots,18}{\text{minimize}} \left(\text{counts} - n\beta - \text{offset}\right) \right]. \tag{4.2}$$

We include an offset parameter, as even after the subtraction of the background image the zero atom signal fluctuates by roughly a tenth of the signal from a single atom. From the obtained single atom fluorescence β and the offset we calculate the atom number for each experimental realization. Here, we reject all runs where the scaled fluorescence signal differs by more than a third of the of a single atom fluorescence from its respective peak. By this procedure we remove approximately 1.0 % of the runs. Note, however, that when fitting the individual peaks with Gaussians, they are separated by more than 10 σ for 6 and 7 atoms indicating that the tails of the distribution are not described by Gaussians. This could be for example caused by technical fluctuations of the fluorescence signal on shorter time scales than the time for 50 experiments. Another possible source could be a loss rate higher than the one estimated from the single particle lifetime measured in Ref. [94], which is consistent with the number of rejected runs increasing for atom numbers above 10. However, as these runs are neglected before any further analysis this is not a problem and does not limit the detection fidelity. Detecting the correct atom number requires a perfect transfer from the microtrap to the MOT. We can estimate a lower bound for the fidelity of transferring atoms from the microtrap to the MOT from the best fidelity of 98.2 ± 0.1 % for initializing 2 atoms. This yields a minimum fidelity of 99 % for the transfer of an atom back to the MOT.

As the atoms are transfered back into the MOT and all hyperfine states are trapped in the MOT, this imaging technique only allows to count the total number of atoms. A way to obtain more information about the system is to remove atoms in one state (either in a spatial mode or spin state) and count the remaining atoms,

[2] We do not use the high resolution objective discussed above, as one of the MOT beams is propagating along this direction and would result in a large background exceeding the atom signal.

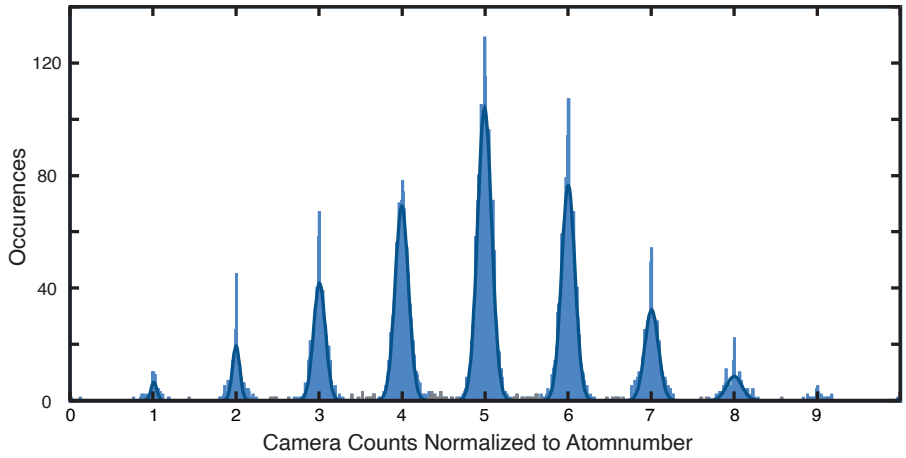

Figure 4.5.: **Histogram of fluorescence signal obtained in MOT imaging.** The peaks corresponding to different atom numbers (light blue) are clearly separated. The peaks are fitted by Gaussians (dark blue) and are spaced by more than 10 σ for 6 and 7 atoms. Rejected runs are shown in gray.

to obtain the occupation of certain modes [11, 14]. Thus, with this imaging technique it is only feasible to measure the occupations of a limited amount of modes, as measurement time increases linearly with the number of possible states. Furthermore, obtaining higher-order correlation functions is very challenging with this method.

4.3.2. Free Space Fluorescence Imaging

More information about the system can be extracted by using a spin and position sensitive imaging scheme [135]. Illuminating an atom with resonant light measures its position and thereby projects the atom to a certain position. Thus, this single-atom sensitive imaging scheme allows us to sample the wavefunction of the N-particle system. By repeating the experiment several times we can obtain all order density correlation functions of a few-particle system [136, 137].
As this method requires no confining potentials, information about the momentum distribution of the atoms can be obtained. This method was first developed at the other experiment of our group. Apart from the camera and a cube in the imaging path both setups are identical and we will only summarize the most important aspects and refer to [135, 138–140] for more details.

For the free space imaging we illuminate the atoms from the side using light resonant to the σ_--transition of the D2 line. The atoms are illuminated by two counter-propagating beams for 20 μs. The two beams are pulsed with a pulse duration of 200 ns with a duty cycle of 45 %. This guarantees that at each point

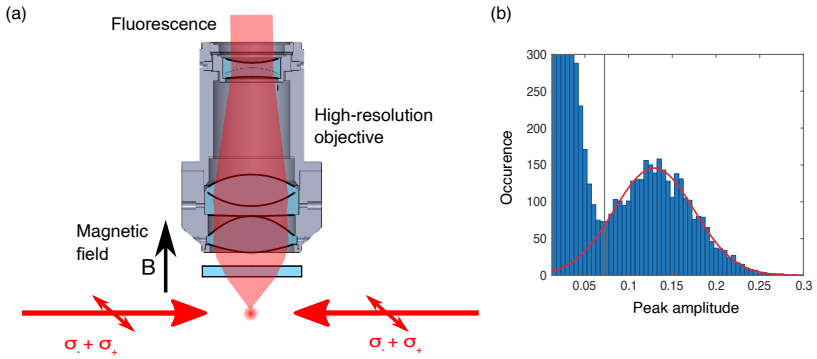

Figure 4.6.: **Imaging setup for free space florescence imaging.** (a) Sketch of the experimental setup. The atoms are illuminated by two counter propagating beams in the horizontal plane. We use light linearly polarized orthogonal to the magnetic field. Due to the different frequencies of the transitions at high magnetic fields, only the σ_--transition is driven. The fluorescence light is collected by the objective and imaged on a EMCCD camera. To avoid the creation of a lattice the two beams are pulsed. (b) Peak heights of binarized, low-pass filtered, images used for atom detection. Peaks above a threshold (gray line) are identified as atoms. Form the Gaussian fit (red) to the right part of the atom peak, we determine the fraction of detected atoms. Panel (a) taken from Ref. [139].

in time the atoms are illuminated only from a single side and avoids effects due to a fast varying light intensity distribution created by a standing wave pattern. The atoms are not trapped during the imaging and perform a random walk in momentum space, which results in a diffusive motion of the atoms limiting the achievable resolution of our imaging system to $\sim 6.5\,\mu$m [140]. In order to limit the diffusion of the atoms and to obtain the largest number of photons per unit time, we illuminate the system with approximately 8 times the saturation intensity. This gives a scattering rate of ~ 16 photons per microsecond, while limiting off-resonant scattering in the other hyperfine state to an average of a single photon in $20\,\mu$s.

The atom florescence is collected by the high resolution objective and imaged on a electron-multiplying charge-coupled device (EMCCD) camera (NüVü HNü 512). The high resolution objective allows to collect 11.4 % of the scattered photons [138]. The number of detected photons is reduced by the quantum efficiency of the chip (specified to be $\sim 90\,\%$) and absorption/reflection by optical elements in the beam path, which we estimate to add up to a transmittance of around 85 %. Thus, the approximately 330 scattered photons, result in an average of ~ 24 photoelectrons per atom.

As the read noise of standard electronics is on the order of a few electrons, it is clear that, this small signal, which additionally is spread over several pixels,

cannot be read out directly. Instead it has to be amplified beforehand. In an EMCCD camera this is done by shifting the pixels through a electron-multiplication register before the readout. This results in a stochastic amplification of the photoelectrons. This amplification shifts the signal of the photoelectrons out of the read noise. Due to the stochastic nature, it is not possible to distinguish between a single and two initial photoelectrons when reading out a single pixel. Hence, the magnification of the imaging is chosen such that the signal from an atom is spread over several pixels, with an average of about 1.5 photons on the brightest pixel.

The first step of the single atom detection is a binarization of the camera signal. A threshold of 5 times the read noise results in an extraction of 80% of the photoelectrons and negligible signal caused by the read noise. The main noise source are so-called clock induced charges (CICs), which result from shifting the signal to the gain register. This shifting can produce electrons on initially empty pixels, that cannot be distinguished from real photoelectrons. The shifting protocol is the biggest strength of the NüVü camera, which for this extraction efficiency has only 0.2 % bright pixels due to CICs. This is a factor 10 better, than the Andor camera used in the other experiment of our group [138].
Next, the binary image is low-pass filtered. This enhances the signal of the clustered photoelectrons compared to the randomly distributed CICs. A histogram of the different low passed pixel values is shown in Fig. 4.6 (b). We find a peak at zero caused by the CICs and a second peak at large values due to the atom signal. The maximum of each peak above a threshold is identified as an atom. This threshold is set as a compromise between good atom detection probability and a low rate of false positive signals due to CICs. Consequently, the imaging fidelity strongly depends on the size of the region of interest: For a larger region of interest the threshold for atom identification has to be increased to prevent large amounts of false atom detections. This reduces the detection fidelity. For the relevant case of 120 by 120 pixels discussed in chapter 6, we obtain a detection fidelity of 92 %. The different steps of the atom detection protocol for an image are shown in Fig. 4.7.

The atom diffusion during imaging in addition to the low-pass filtering result in an effective resolution of $\sim 6.5\,\mu$m. Two atoms have to be separated even further in order to reliably be detected as individual atoms. Thus, our imaging technique does not allow us to take in situ images but it is suitable to image few-fermion samples after a time of flight expansion, where densities are sufficiently

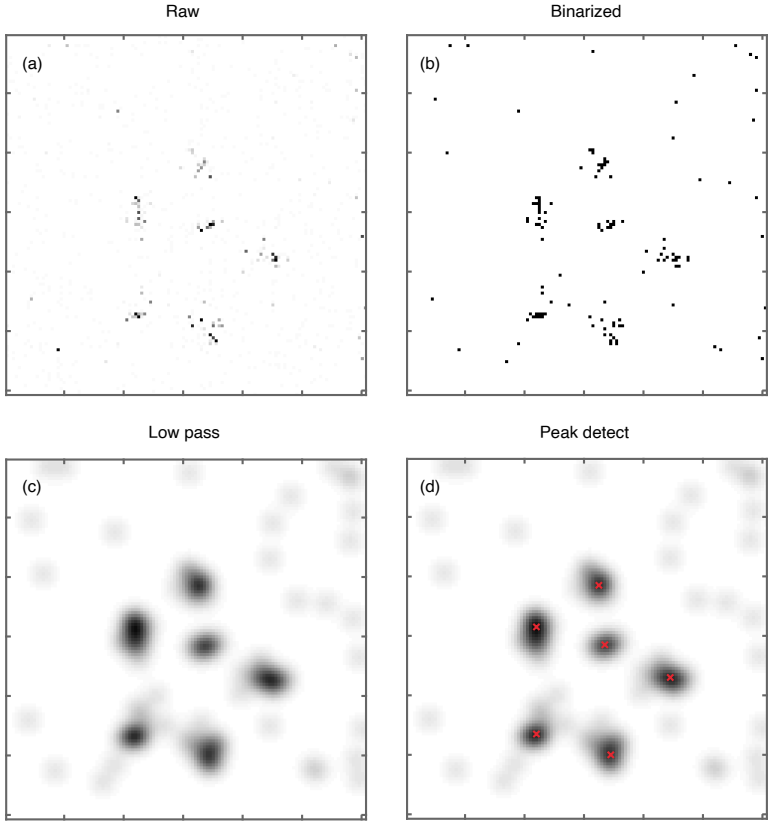

Figure 4.7.: **Single atom detection protocol.** The different panels show the processing steps of a raw florescence image (a). The raw image is binarized (b) and low pass filtered (c). Peaks above a threshold are assigned to atoms, with the atom position (red cross) at the maximum of the cluster (d).

low. The time of flight is not performed in free space but instead a matter-wave focusing technique is applied (chapter 3.6) inside the SWT trap. The tight axial confinement of the SWT guarantees that the atoms stay within the depth of focus of the objective.

Imaging is performed at high magnetic fields, where the imaging transitions for the different hyperfine states are different by approximately 80 MHz. Therefore the imaging scheme is spin sensitive. By illuminating the two used hyperfine states one after another, with a short pause in between to shift the image on the camera to a region covered by a mask, it is possible to image both spin states in a single experimental realization. This makes it possible to obtain information on correlations between the different spin states [135]. However, due to limitations of the NüVü camera, that will be resolved in the future, we are currently only able to take a single image in each experimental realization. Thus, for the measurements presented in chapter 6, we image state $|3\rangle$ only. This state has

a completely closed imaging transition and does not require a repumper, as opposed to the other hyperfine states [140].

In principle, the PBS allows us to count the total atom number after a free-space fluorescence imaging with much higher fidelity using the MOT. This would make the atom detection in the free-space imaging more robust as the total number of atom would be known and the atoms only have to be assigned to the most likely positions. We have not implemented this yet, as we only image a single spin component. Thus, obtaining the total atom number using MOT imaging does not help in the current situation as it only provides a upper bound on the number of atoms in a single spin state.

4.4. Deterministic Preparation

In this section we discuss our scheme to deterministically prepare mesoscopic samples in the ground state of a harmonic trap. More details about the method and theory considerations can be found in Ref. [11, 131]. The concept of this so-called spilling method is shown in Fig. 4.8. The idea is to start with a filled Fermi sea, such that the lowest trap levels are occupied by a single atom with probability close to one. Then, by manipulating the potential, we create a configuration where only a well-defined number of bound states remain in the trap. If the lifetime of these quasi-bound states is much larger than the time particles initially occupying the higher levels require to leave the trap it is possible to skim off all particles in higher states while retaining all particles in the lower states. Since these are occupied with a single atom (per spin state) this allows us to deterministically create a well-defined number of atoms in the trap. This method requires to control the potential depth (much) better than the level spacing and thus works best in tight traps with a large level spacing.

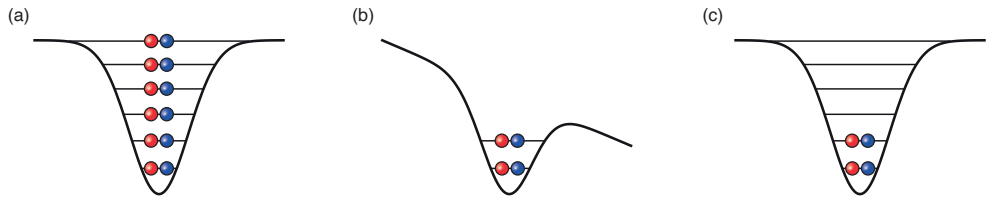

Figure 4.8.: **Scheme to prepare well-defined atom numbers.** Starting from a filled Fermi sea (a), the potential is lowered and tilted (b). This results in a finite number of bound states in the trap. Atoms in higher lying states leave the trap. This creates a well-defined number of atoms in the ground state of the trap. Adapted from Ref. [131].

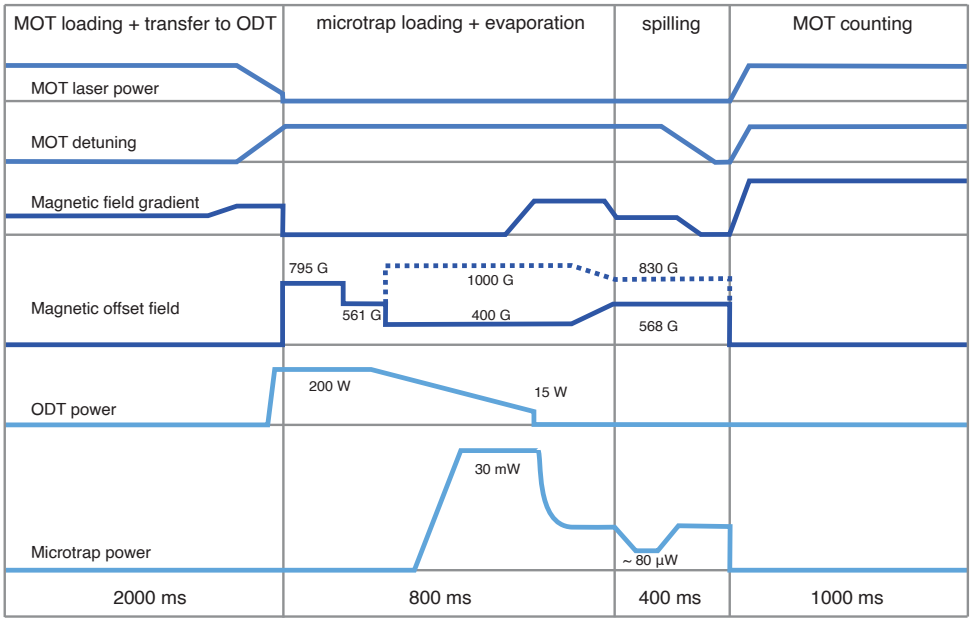

Figure 4.9.: **Sketch of the experimental sequence.** The sequence for the deterministic preparation of a few particles in the ground state of a harmonic trap takes 4 s. Hence, our setup allows for fast cycle times.

The experimental sequence is sketched in Fig. 4.9. It starts by loading the MOT and transferring the atoms to the deep large volume optical dipole trap (ODT). Here, we transfer the atoms in state $|2\rangle$ to state $|3\rangle$ using an rf pulse at a magnetic field of $B = 561\,\mathrm{G}$ [104]. The $|1\rangle\,|3\rangle$ mixture has more favorable scattering properties for the creation of repulsively interacting samples and is better suited for fluorescence imaging as discussed above. The relatively low density in the ODT limits the thermalization rate and evaporation to a degenerate Fermi gas would take several seconds as discussed in section 3.4.2. Thus, we transfer the atoms from the large ODT into a tight optical trap (microtrap) created by focusing light through the high resolution objective. This is done by ramping the power of the microtrap to $\sim 30\,\mathrm{mW}$ in 200 ms, while reducing the power of the ODT to 15 W. We set the magnetic field to $B = 400\,\mathrm{G}$ for the preparation of a repulsively interacting sample. This magnetic field for the loading of the microtrap is chosen as the moderate scattering length ($a_{\mathrm{sc}} = -840\,a_0$) gives a good compromise between a fast thermalization rate of atoms into the microtrap, while limiting atom loss due to three-body collisions in the tightly focused microtrap. Thermalization of atoms into the microtrap takes another 200 ms after the end of the ramp. After this point thermalization of atoms from the ODT into the microtrap and losses in the microtrap balance. We end up with approximately 1500 atoms in the microtrap. We extinguish the ODT and perform forced evaporation in the microtrap

by lowering the power in the beam to 500 μW in 20 ms at which point we obtain approximately 200 atoms.[3]

In the next step we create a well-defined number of atoms in the ground state using spilling method described above. To this end, we apply a magnetic field gradient of 24 G/cm along the axis of the microtrap beam and lower the microtrap depth for a spilling time of 40 ms. The mean atom number depends on the final microtrap depth and is shown in Fig. 4.10 (a). Clear plateaus for even atom numbers are visible. Since each trap level is occupied with one atom per spin state only even atom numbers can be initialized in a well-defined state. The atom number spacing of the plateaus of two atoms is the result of the quasi-1D structure of the lowest levels of our radially symmetric microtrap, which has a aspect ratio of $\omega_r/\omega_z = 3.40 \pm 0.03$. The deterministic initialization of samples with atom numbers larger than 6 becomes difficult in this configuration. This is due to the increased density of states in this energy range, which requires better control over the potential to place the trap barrier between two levels.
The enhanced stability of the even atom number configurations is also visible in the variance shown in Fig. 4.10 (b). For even atom numbers the variance is suppressed, reaching values as low as 0.03 (0.18) for 2 (6) atoms. The fidelity for initializing a system with 2, 4 or 6 atoms is $97 \pm 1\,\%$, $93 \pm 2\,\%$ and $85 \pm 2\,\%$, respectively. Where we define the fidelity as the probability of initializing the system with the correct atom number.

Assuming that the system is in the ground state after the spilling procedure allows us to calculate the entropy of the created system. The von Neuman entropy of a state, with density matrix ρ is given as [33]:

$$S_{\text{tot}} = -k_B \,\text{tr}(\rho \ln \rho) = -k_B \sum_j p_j \ln p_j. \tag{4.3}$$

In the second step, we have decomposed the system in an eigenbasis and the j^{th} eigenstate occurs with probability p_j. Assuming no excitations, the only fluctuations in our system are atom number fluctuations. Since we spill at a magnetic field of 568 G the system is non-interacting and the two spin states are independent. Thus, there are two different but equally likely states for odd atom numbers, as one atom of either of the two hyperfine states can be missing. For

[3] Achieving high densities for fast evaporation in the tight dimple is the main bottleneck when reducing the sequence duration. Loading the microtrap directly from the MOT does not help, as light assisted collisions limit the density in the MOT and thus the number of atoms transfered to the small volume microtrap.

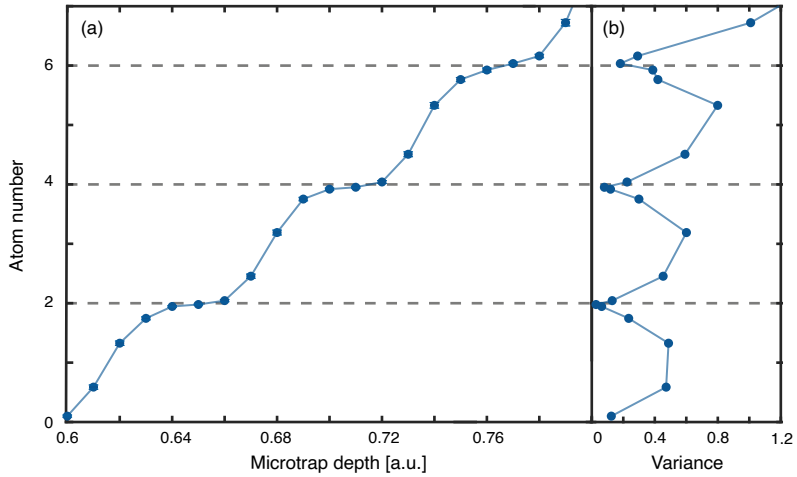

Figure 4.10.: **Deterministic preparation of ground state configuration of fermions.** (a) Mean atom number as function of the final microtrap depth during spilling. Plateaus are observed for even particle numbers. The variance (b) is reduced for even atom numbers indicating the enhanced stability of these configurations. Each point is the average of 368 measurements.

even particle number there is only one possibility and the total number entropy is

$$S_{\mathrm{tot}} = -k_B \sum_{n \text{ even}} p_n \ln p_n - k_B \sum_{n \text{ odd}} p_n \ln \frac{p_n}{2}. \tag{4.4}$$

Where p_n is the probability of detecting n atoms. This gives entropies per particle of $S = (0.08 \pm 0.02)\, k_B$, $S = (0.09 \pm 0.02)\, k_B$ and $S = (0.11 \pm 0.02)\, k_B$ for 2, 4 and 6 atoms respectively. This is comparable to what is achieved in other mesoscopic fermion systems, where for a band insulator entropies as low as $(0.016 \pm 0.003)\, k_B$ are reached [141]. However, when transforming this state to a non-trivial anti-ferromagnet they observe an entropy increases by $(0.46 \pm 0.02)\, k_B$ [141]. This estimate for the entropy is a lower bound, as we assumed the system to be in the ground state.

An estimate for the probability of initializing the system in the ground state can be obtained by following the reasoning of Ref. [131]. Here, we discuss the case of two atoms. The lowest energy excited state of two atoms consists of one atom in the ground state and one in the next higher trap level. A lower bound for the probability of a hole in the ground state can be estimated from the probability of obtaining a single atom P_1. At the same time, a lower bound on the probability of initializing an atom in the first excited state can be deduced from the probability of preparing three atoms P_3. Since for our non-interacting system

the probabilities for obtaining a hole in the ground state and for the preparation of an atom in the first excited state are independent, a lower bound for the probability of preparing two atoms in the excited state is given by $P_1 \cdot P_3 \approx 10^{-4}$.
A lower bound estimate for the probability of creating two atoms in the ground state can be found from spilling the trap to the same target atom number twice [131]. The resulting atom number distributions are shown in Fig. 4.11 for spilling to two atoms once (a) and twice (b). From the distribution after the first spilling we know that the second spilling removes all atoms in higher lying states, with a probability of $98.1 \pm 0.5\%$. Thus, systems consisting of three atoms after the first spilling will be spilled to two atoms in the second spilling. Hence, when assuming that the second spilling only removes atoms in excited states and introduces no noise, the probability of initializing two atoms in the ground state after the first spilling is $P_{N=2}(\text{second spilling}) - P_{N=3}(\text{first spilling}) = 91.7 \pm 1.0\,\%$. Thus, an upper bound for the initialization of two atoms in an excited state is $95.2\,\% - 91.7\,\% = 3.5 \pm 1.1\,\%$.
This value includes possible excitation of the atoms between the two spilling processes. We can estimate the amount of excitations due to non-adiabatic potential ramps during the spilling procedure [142]. We find that, under the assumption of a harmonic potential, excitations of the system due to the ramp can be neglected, as they result in an estimated excitation probability of less than 3×10^{-4} for the chosen ramp parameters. However, the shape of the potential during the spilling is significantly different from a harmonic oscillator and the excitation probability might be larger than this estimate. The obtained value of $3.5 \pm 1.1\,\%$ for the initialization of two atoms in an excited state is a upper bound, since we have assumed that the second spilling introduces no additional fluctuations. This is equivalent to assuming that all holes in the lowest trap level after the first spilling are due to thermal holes of the initial state or due to heating of the sample after the first spilling and before the second spilling.
In contrast to this estimate, another assumption would be that holes are created with equal probability during each spilling. This would give a probability of creating a hole in the lowest trap level of $P_{N=1}(\text{first spilling}) = 2.9 \pm 0.5\,\%$ during the spilling. Hence, the expected probability of obtaining two atoms after spilling twice is $1 - (P_{N=1}(\text{first spilling}))^2 = 94.3 \pm 1.0\,\%$ consistent with the measured probability of $P_{N=2}(\text{second spilling}) = 93.6 \pm 0.9\,\%$. Under this assumption there would be no excitations (at a level detectable with this number of realizations) in the system after the first spilling and all fluctuations of the system are due to number fluctuations (consistent with the first estimate).

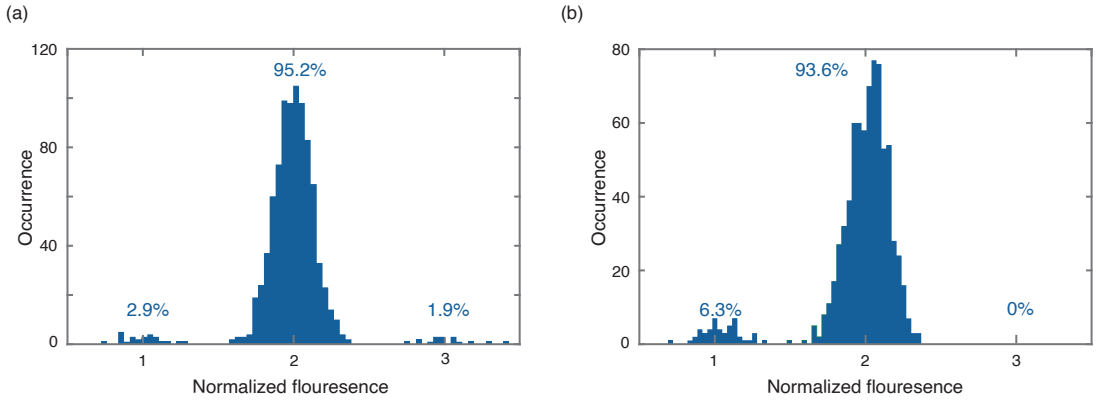

Figure 4.11.: **Atom number distribution for spilling once and twice.** Spilling to a target number of two atoms once and twice yields the atom number distributions in panel (a) and (b) respectively. The histogram contains data from 900 and 785 experiments for (a) and (b). Note that the fidelity of initializing 2 atoms when spilling once (a) is slightly lower than for the data shown in Fig. 4.10. Adapted from Ref. [130].

To sum up, we are able to prepare low-entropy mesoscopic samples of two component fermions in our micron sized dimple. These low-entropy samples are the starting point for all experiments described in the remainder of the thesis. After the preparation of a low-entropy sample, we (adiabatically) deform the trapping potential to access interesting Hamiltonians and quantum states.

4.5. Manipulating the Potential

In this section, we discuss how we use the SLM in our setup. First, we summarize our protocol of how we use the SLM to correct aberrations in order to achieve the smallest possible spot size of the microtrap. Since the deterministic preparation of few-fermion samples is very sensitive to trap size [131], this significantly improved the preparation fidelity and was one of the prerequisites to achieve the high preparation fidelities discussed above. Furthermore, we discuss how we dynamically change the phase pattern displayed on the SLM during an experimental sequence. This allows us to dynamically transform the trapping potential and engineer interesting Hamiltonians.

4.5.1. Correcting Aberrations

Aberrations of the optical system can strongly affect the quality of the trapping potentials and limit the smallest obtainable spot size. They are unwanted local

shifts of the phase of the light field and are caused by imperfections of the optical setup, like spherical lenses or off-center alignment. Aberrations are often quantified by Zernike polynomials which are orthogonal functions on a disc. Their first orders coincide with the typical aberrations in optical systems. Their representation on a rectangular shape like the SLM is given in Ref. [143].
Using the SLM we can actively correct the aberrations and reach a nearly diffraction limited performance for the creation of the microtrap. One approach to determine the aberrations of an optical setup is to utilize a Shack-Hartman algorithm [125, 144]. Here, traps are created from a small sample patch on the SLM. The position of the trap created in the atom plane depends on the linear phase gradient on the sample patch (see section 4.1.1). Thus, by measuring the position of the atoms, one can obtain the local phase gradient of the light field across the sample patch. Then, by integrating the phase gradients one obtains a map of the aberrations created by the optical system. An alternative method relies on interfering a moving sample patch on the SLM with a reference patch created in the center of the SLM in the atom plane [118]. Both methods can be used to determine and then correct aberrations to a level much better than λ [118, 126]. However, they require to measure the position of the atoms with high accuracy. In order to determine the aberrations to a level (much) better than λ one has to measure the atom position (much) better than 1μm. With the current resolution of our imaging method it would be very challenging to measure these small shifts of the large traps with sufficient accuracy. At this level it is even challenging to determine the center of the atom distribution over several runs with sufficient precision.
We found a different approach to correct aberrations which does not require in situ imaging of the atom position. Here, we make use of the fact that our scheme for the deterministic preparation of single atoms, is very sensitive to the size of the microtrap [131]. To determine the aberrations we employ a spilling sequence, where we keep the applied magnetic field gradient during spilling constant for all following measurements. We start by finding the optical power required for stable preparation of two atoms. Now we apply a phase pattern to the SLM corresponding to the fourth Zernike polynomial and optimize its amplitude, such that the optical power for stable preparation of two atoms is minimal. We keep the determined phase pattern and repeat this procedure by scanning the amplitude of the first 15 Zernike polynomials[4] one after another. This optimization of the displayed phase pattern reduces the required optical power for stable prepa-

[4]We do not scan the first three Zernike polynomials as they only displace the focal spot and do not alter the spot size.

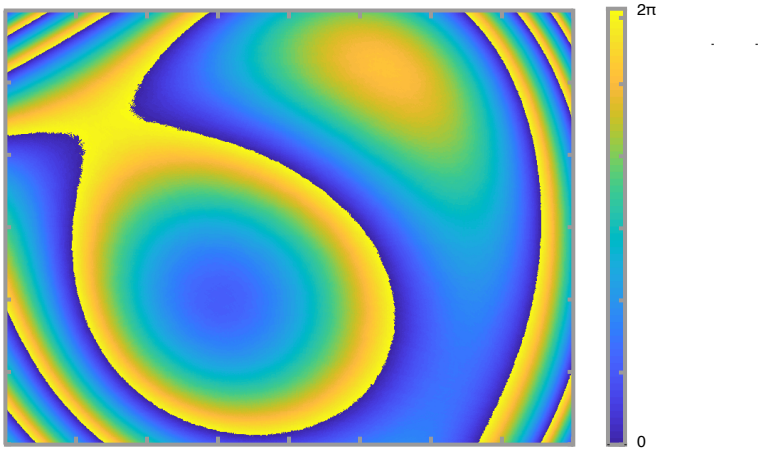

Figure 4.12.: **Map of the aberration of the optical setup.** SLM phase map obtained by scanning the Zernike polynomials in order to optimize the power required for the preparation of two particles. This map should compensate for most of the aberrations of the microtrap optical setup.

ration of two atoms by a factor of two. This indicates a significant decrease of the spot size. Using this method thus allows us to correct the aberrations of the optical setup. However, currently, we have no method to determine the residual aberrations.

Further indication that this protocol effectively reduces aberrations is obtained by measuring the aspect ratio of the microtrap, from which we extract a Gaussian spot size of $0.82 \pm 0.01\,\mu$m. This value is only 10% larger than the theoretical minimal spot size of $0.72\,\mu$m one would obtain for the design specifications of the objective. The measured spot size corresponds to a maximum diffraction limited NA of 0.54.

4.5.2. Measuring Trap Frequencies

Since we have no suitable scheme to either image the atom distribution in the trap or take an image of trap focus with sufficient resolution, we have to apply different methods to characterize the trapping potential. Information about the potential can be obtained by measuring the excitation spectrum of a (non-interacting) trapped sample. The potential of a dipole trap is proportional to the intensity distribution $I(r, z)$ of the light field (see equation (3.2)). For a Gaussian beam of waist w_0 the trap frequencies (in harmonic approximation) are [102]:

$$\omega_r = \sqrt{\frac{4U_0}{mw_0^2}} \quad \text{and} \quad \omega_z = \sqrt{\frac{2U_0\lambda^2}{\pi^2 m w_0^4}}, \tag{4.5}$$

where ω_r (ω_z) is the trap frequency for excitations orthogonal (along) to the beam propagation axis and $U_0 \propto I(0,0)$ is the central trap depth. From the aspect ratio of the trap it is possible to calculate the beam waist via

$$\eta = \frac{\omega_r}{\omega_z} = \frac{\sqrt{2}\pi w_0}{\lambda}. \tag{4.6}$$

Experimentally, we perform spectroscopy on the non-interacting two-atom system (at $B = 568\,\mathrm{G}$), as interaction modify the excitation spectrum (see Fig. 2.6). This is done by initializing two atoms in the ground state and exciting the system by modulating the power of the trapping beam. Subsequently, atoms in excited trap levels are removed by a second spilling procedure and the remaining atoms are counted in the MOT. Modulating the depth of the potential modulates the trapping frequency and the time dependent Hamiltonian (in harmonic approximation) is:

$$\hat{H} = \frac{p^2}{2m} + \frac{1}{2}m\omega^2(1 + \epsilon\sin(\omega_{\mathrm{ex}}t))x^2. \tag{4.7}$$

Where ϵ gives the strength of the modulation of the potential depth at a frequency ω_{ex}. This modulation $\propto x^2$ has the same symmetry as the trap, which is spatially symmetric around the origin. Hence, only states with the same parity are coupled and the lowest resonance consist of excitations of one atom from the ground state two levels up ($\Delta n = 2$) and (neglecting anharmonicity) its frequency corresponds to twice the trap frequency.
Fig. 4.13 shows the excitation spectrum for a power of $P \approx 120\,\mu\mathrm{W}$. The measured trap frequencies of $2\,\omega_z = 2\pi \times (5.29 \pm 0.04)\,\mathrm{kHz}$ and $2\,\omega_r = 2\pi \times (17.98 \pm 0.06)\,\mathrm{kHz}$ yield an aspect ratio of 3.40 ± 0.03 and a Gaussian beam waist of $0.82 \pm 0.01\,\mu\mathrm{m}$.

Tuning the Potential

For all our experiment we create the low-entropy sample in the smallest possible microtrap, as this trap offers the largest splitting of the energy levels $\omega_z \propto 1/w_0^2$ at a given trap depth U_0 (see equation 4.5). Thus, we have to dynamically deform the potential after initializing the low-entropy sample, to reach interesting systems beyond the quasi-1D harmonic trap. This is achieved by changing the phase pattern displayed on the SLM. The possible phase ramps are constrained by the properties of the SLM. The SLM controller is connected as a display to the graphics output of a computer. Its frame rate is 120 Hz and a new phase pattern (picture) can be displayed every 8 ms. Ramps of the phase pattern are displayed as a movie (series of pictures) on the SLM. Since the graphics output

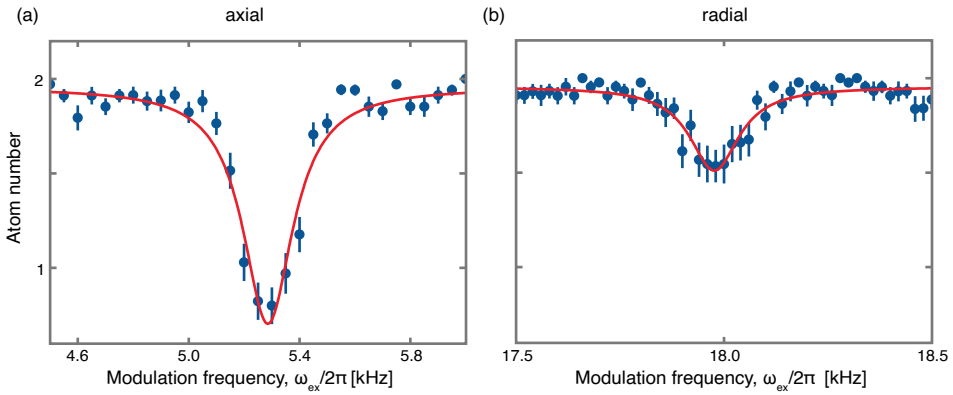

Figure 4.13.: **Excitation spectrum of two non-interacting particles.** When the modulation frequency matches the energy gap between the ground and the excited state atoms are excited and lost after a second spill. The dips in the spectra (a) and (b) correspond to axial and radial excitations, respectively. Fitting a Lorentzian (red line) gives excitation frequencies of 5.29 ± 0.04 kHz (a) and 17.98 ± 0.06 kHz (b). The data is obtained for a power of approximately 120 μW. Each data point is the average of at least 40 measurements.

of the computer cannot be triggered, we use the internal clock of the computer to time the phase ramps, which is sufficiently precise over the time of a single experimental run. The jitter of the displayed movie of 8 ms compared to the rest of the sequence is given by the frame rate of the SLM.

Another constraint on the ramps is the slow adjustment of the liquid crystals to the new equilibrium position after changing the voltage. This results in fall and rise times of the phase of 20 ms and 80 ms respectively. This sets the time scale for the adjustment to a new phase pattern. A measurement of the light intensity of the trapping beam during a phase ramp confirms the slow equilibration time of approximately 90 ms. Thus, we chose to wait for 100 ms after the end of a phase ramp, before we continue with critical parts of the experimental sequence (such as spilling or trap modulation).

In order to keep the ramps of the potential as short as possible, we use phase movies consisting of only 5 pictures which are displayed over a time of 20 ms, instead of waiting for the phase to settle after each newly displayed picture. Hence, we cannot control the intermediate phase pattern and potentials during the ramp. Note, however, that the ramp of the potential is smoothed out by the slow response time of the liquid crystals (longer than the time between different displayed images). In the experiment we do not observe excessive heating of the atoms during the ramps. This indicates that these slow ramps of the phase pattern result in sufficiently smooth potential transformations causing only negligible excitations (for the phase ramps studied in this thesis).

4.5.3. Transforming the Trap

Next, we discuss the transformations of the trapping potential that are necessary to create the quasi-2D samples, which are used for the measurements presented in the remainder of the thesis.[5]

The properties of both attractively and repulsively interacting fermions in the quasi-1D geometry of a single microtrap have already been extensively studied [12, 97, 145–147]. The goal of this thesis is to study quasi-2D few-fermion systems, as they offer richer physics, like quantum phase transitions [27, 28]. However, from equation (4.6) it is clear that the low-energy spectrum of a single beam optical trap is always quasi-1D. Thus, we combine the microtrap with a single layer of the SWT to create quasi-2D samples. The maximum axial trap frequencies we can achieve in the SWT are around $\omega_z \approx 2\pi \times 7\,\mathrm{kHz}$ (see section 3.4.3). This sets an upper limit for the radial trap frequencies of the microtrap if we want to create a quasi-2D geometry. Demanding a moderate aspect ratio of 7:1, requires a radial trap frequency below $\omega_r \approx 2\pi \times 1\,\mathrm{kHz}$. This frequency corresponds to a harmonic oscillator length of $l_{\mathrm{ho}} \approx 1.3\,\mu\mathrm{m}$. This is significantly larger than the size of our microtrap and we would not obtain a well-defined spectrum with several bound shells in the microtrap at this depth. This problem can be solved by increasing the size of the microtrap. This reduces the curvature of trap potential and thus results in smaller trap frequencies at the same depth of the potential. From equation (4.5), we obtain $\omega_r \propto 1/w_0$ for a constant potential depth U_0.

In the experiment, we tune the microtrap size by changing the diameter of the beam entering the objective. For this purpose we use the SLM as an amplitude mask. We block all light, but the first diffraction order created by a phase gradient on the SLM in the first image plane of the SLM (see section 4.2). Thus, when displaying the phase gradient on only a part of the SLM, we remove the light reflected from the other parts of the SLM before it hits the objective. We use a round mask for the region, where the gradient is displayed on the SLM. From the phase mask radius and the optics in the beam path one can calculate the expected size of the trapping beam as

$$w_0 = K\frac{\lambda}{2\mathrm{NA}}, \tag{4.8}$$

where the NA is determined by the size of the aperture displayed on the SLM. The constant K depends on the homogeneity of the illumination of the aperture

[5] We also worked on transferring systems initialized in the ground state of the microtrap into an array of microtraps to study Fermi-Hubbard systems. A summary of the first experimental results along these lines can be found in Ref. [130].

and for a Gaussian beam is given by [131, 148]

$$K = 0.82 + \frac{0.32}{(T - 0.28)^{1.82}} - \frac{0.53}{(T - 0.28)^{1.89}}. \tag{4.9}$$

Here, $T = w_{\mathrm{in}}/r_{\mathrm{ap}}$ denotes the truncation ratio of the beam and is given by the ratio of the beam waist in the aperture plane w_{in} and the aperture radius r_{ap}. For a truncation ratio of 2, we obtain $K = 0.85$ which only slightly larger than $K = 0.82$ obtained for homogeneous illumination.

Equation (4.8) shows that the trap size is (approximately) inversely proportional to the aperture radius in the SLM plane. From equation (4.5) we find that the radial and axial trap frequencies at fixed total beam power $P \propto U_0 w_0^2$ scale as $\omega_r \propto 1/w_0^2$ and $\omega_z \propto 1/w_0^3$. Due to this strong dependence of the axial trap frequency on the trap size, the SWT trap has to be turned on before ramping to small aperture radii (corresponding to spot sizes $\geq 3\,\mu$m). Otherwise the small axial trap frequency results in a non-adiabatic transformation of the potential and heating of the atoms. Since the diffraction efficiency and hence the available power in the atom plane is proportional to the area of the aperture in the Fourier plane, we are currently working with focal spot sizes of up to $w_0 \approx 4.8\,\mu$m, where we achieve radial trap frequencies of up to $\omega_r \leq 2\pi \times 1.5\,$kHz. These spot sizes and trap depths fulfill the requirements for the creation of a quasi-2D geometry, with several well-defined bound shells inside the potential and are used in the experiments described in the next chapter.

5. Observing the Few-Body Precursor of a Phase Transition

In the last chapters we have seen that (statistical) physics is very successful in describing the properties of macroscopic systems consisting of thousands of particles even in the strongly interacting limit. In order to understand these macroscopic systems, the experimental observations are connected to a theoretical description in the thermodynamic limit. Here, concepts like symmetry breaking, phase transitions [5] and thermalization are used. Often, one focuses on the important emergent (collective) degrees of freedom to derive effective models, which capture the essential physics. However, especially in a strongly interacting regime, finding the correct effective models is challenging as they cannot be derived by simply extrapolating from the two-body problem.

The question of how many-body physics emerges when the number of particles is increased is especially important for mesoscopic systems consisting of tens of particles. They are still far from the thermodynamic limit, but the exponential growth of the Hilbert space size with particle number prohibits an exact solution. Systems of this size are of interest in several fields of physics and paradigmatic examples of these strongly interacting mesoscopic systems are nuclei, whose spectra can exhibit collective excitations consistent with BCS theory [8]. However, in naturally occurring systems it is difficult to systematically study the emergence of many-body physics as in these systems it is not possible to freely tune the particle number or interactions.

Recently ultracold atoms have been used as artificial model systems to study the emergence of collective behavior in a more controlled and flexible fashion. Their big advantage is the full tunability of particle number, interactions and single particle spectra. So far, these experiments have been limited to quasi-1D systems [11, 12, 145, 147].

In this chapter we describe how we extend this capability to deterministically create a tunable number of atoms in the ground state of a quasi-2D trap. Here, symmetries of the potential give rise to degenerate energy levels and result in the formation of a shell structure for fermionic atoms. This shell structure results

in an enhanced stability of the closed-shell configurations, where all states up to some energy (shell) are occupied and all higher lying shells are empty. These deterministically initialized closed-shell configurations are the starting point for all further measurements. In these experiments we study the emergence of collective excitations and observe the few-body precursor of a quantum phase transition. The measurements along these lines are presented in the second part of this chapter. Parts of the results presented in this chapter have been published in Ref. [93].

5.1. Creating Closed Shells of 2D Fermions

The starting point for our measurement of the few-body precursor of a phase transition are low-entropy samples of quasi-2D Fermi gases. We prepare these using the tools discussed in chapter 4 and the procedure described below.

5.1.1. Transfer to a Quasi-2D Trap

We start with a $|1\rangle|3\rangle$ mixture of 20 ± 1 atoms in the tightly focused quasi-1D microtrap. This atom number is chosen such that it is possible to load a single layer of the SWT during the transfer to the combined quasi-2D trap. Since we are interested in attractively interacting fermions, we prepare the sample at a magnetic field of $B = 830\,\mathrm{G}$, above the Feshbach resonance.
As a first step, we have to transfer the atoms to a quasi-2D geometry (see Fig. 5.1 for a sketch of the protocol). To this end, we start by linearly increasing the depth of the SWT from 0 to 4 W in 20 ms. This power of 4 W results in an axial trapping frequency of $\omega_z(\mathrm{SWT}) = 2\pi \times (6.80 \pm 0.05)\,\mathrm{kHz}$. The axial confinement of the microtrap of $\omega_z(\mathrm{microtrap}) \approx 2\pi \times 3.8\,\mathrm{kHz}$ guarantees the adiabaticity of this fast ramp. Note that the system is still in a quasi-1D geometry after this stage. Loading a single layer of the SWT requires the mean width of the atom cloud trapped in the microtrap to be (much) smaller than half the spacing of the different layers of the SWT of $4.4\,\mu\mathrm{m}$. The root mean square width of the n_z^{th} harmonic oscillator level is

$$\sqrt{\langle z^2 \rangle} = \sqrt{\frac{\hbar}{m\omega_z}}\sqrt{n_z + \frac{1}{2}} \approx \sqrt{n_z + \frac{1}{2}}\,660\,\mathrm{nm}. \tag{5.1}$$

Thus, $n_z \ll 11$ is required for the highest occupied level of the microtrap. For approximately 10 atoms per spin state and an aspect ratio of ~ 4 of the microtrap, we obtain a sufficiently small $n_z = 5$ for atoms at the Fermi surface. Furthermore,

the transfer is performed at attractive interactions which decrease the size of the cloud further.
The transfer to a quasi-2D geometry is done by ramping the radius of the microtrap aperture, where the gradient on the SLM is displayed to 40 pixels in 20 ms. This changes the focal spot size of the microtrap to 4.8 μm. At the same time, we increase the power in the microtrap beam by a factor of 6 to keep the radial trapping frequencies above $\omega_r \approx 2\pi \times 1\,\mathrm{kHz}$. This transfers the atoms to a quasi-2D trap with an aspect ratio $\omega_r : \omega_z \approx 1 : 7$.

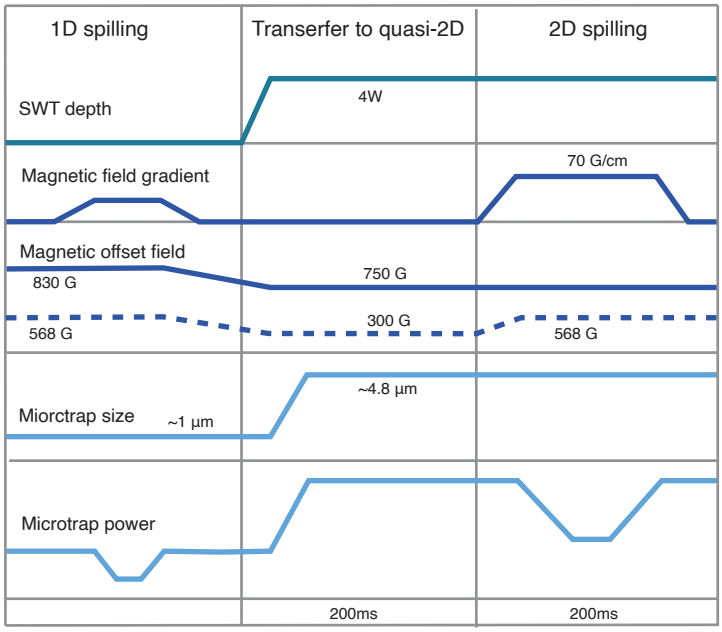

Figure 5.1.: **Sketch of the experimental sequence used to create low-entropy 2D samples.** We start with approximately 20 atoms after the 1D spilling (section 4.4). In a first step we transfer the atoms to a quasi-2D geometry by turning on the SWT and increasing the focal spot size of the microtrap. In a second step we create closed-shell configurations of the system by a 2D spilling procedure. The dashed line shows the magnetic offset field used for the creation of non-interacting samples.

During the transfer the energies of several occupied and unoccupied trap levels cross. This can create holes in the final atom distribution. Imperfections and the non-separability of the real trapping potential result in a coupling of the levels and avoided crossings. In order to increase the coupling between the levels, the magnetic field is tuned to 750 G, where the scattering length is $a_{\mathrm{sc}} = -5200\,a_0$. The strong interactions at this magnetic field result in an increased coupling of the levels. This gives rise to larger avoided crossings between the levels and hence reduces the probability of exciting the system, when changing the geometry from quasi-1D to quasi-2D. Indication for the enhanced coupling due to interactions

can be obtained from a measurement, where we initialized 6 atoms in the quasi-1D trap ramped to a quasi-2D geometry and back to the quasi-1D geometry and measured the number of atoms remaining in the lowest 3 levels. For this measurement, we used a sample created at a low magnetic field to directly compare the ramp for an interacting and a non-interacting sample. If we performed the transfer at magnetic field of $B = 350\,\mathrm{G}$ ($a_{\mathrm{sc}} = -883\,a_0$), we retained an average of 5.6 ± 0.2 atoms after the second spilling, compared to a much lower average of 3.2 ± 0.2 atoms, when the ramp was performed with a non-interacting sample at $B = 568\,\mathrm{G}$.

5.1.2. Observing the Shell Structure of a 2D Fermi Gas

We reveal the shell structure of fermions in a 2D harmonic oscillator and create a low-entropy sample by extending the spilling procedure discussed in section 4.4 to a quasi-2D geometry. To this end, we linearly reduce the power of the microtrap within 60 ms to a final trap depth V, where it is kept for 40 ms, before ramping the power up again. This final trap depth V results in a shallow trap with only a few bound levels. The number of remaining trap levels is given by the final power of the microtrap. Atoms in higher lying states become unbound and leave the small microtrap volume, but they remain trapped within the weak radial confinement of the SWT of $\omega_r(\mathrm{SWT}) \approx 2\pi \times 20\,\mathrm{Hz}$.
In order to remove atoms that have left the microtrap, but are still bound in the SWT, we apply a magnetic field gradient of $B'_z \approx 70$ G/cm along the z-axis at the same time. Note that this gradient is along the z-axis only and we do not apply a gradient in the radial direction. Thus, in contrast to the 1D spilling, we simply lower the depth of the microtrap until only a few energy shells remain bound and do not tilt the radial trapping potential. Consequently, the microtrap power required to create a certain number of atoms in the microtrap does not depend on the strength of the applied magnetic field gradient,[1] which is only used to remove atoms that have already left the microtrap from the SWT. Hence, the 2D spilling is a two-step process, with the atoms first leaving the microtrap and then the SWT at its edge. Further evidence for the absence of a sizable gradient in the radial plane is given by the observed shell structure discussed below. The degeneracy of the levels indicates a radially isotropic trap.

[1] We have measured the required microtrap power for stable preparation of 6 atoms in the quasi-2D geometry as a function of the magnetic field gradient B'_z and found only a very weak dependence on the gradient. For this measurement the atoms remaining in the microtrap after the 2D spilling were transfered back to a quasi-1D geometry. This is required since the SWT has to be extinguished before counting the atom number, in order to remove atoms still trapped in the SWT after the 2D spilling without gradient.

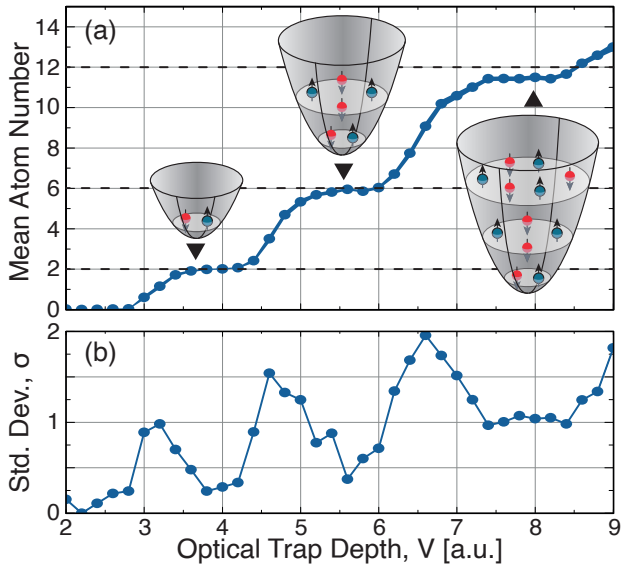

Figure 5.2.: **Deterministic preparation of a 2D Fermi gas.** (a) Mean atom number as function of the final microtrap depth during spilling. Plateaus are observed for 2, 6 and 12 atoms. Each point is the average of 85 measurements and errors are smaller than the symbol size. The inset sketches the corresponding occupations of the 2D harmonic oscillator levels. The enhanced stability of the closed-shell configurations is also seen from the standard deviation (b), which is reduced for closed-shell configurations. Figure adapted from Ref. [93].

The atom number distribution after the quasi-2D spilling procedure as function of the final microtrap power is shown in Fig. 5.2 (a). We observe stable atom number plateaus for 2, 6 and 12 atoms. These numbers correspond to the closed-shell configurations of the 2D harmonic oscillator, where the n^{th} shell contains $n+1$ atoms per spin state. Thus, the closed-shell configurations, where all states up to the n^{th} shell are occupied and all higher lying states are empty contain $(n+2)(n+1)$ atoms (including a factor of two for the spin). The reduced standard deviation of the atom number distribution at the plateaus (Fig. 5.2 (b)) gives further evidence for the enhanced stability of the closed-shell configurations. This enhanced stability is akin to the chemical stability of noble gases and 'magic' number nuclei.

In the experiment, we observe the third closed-shell configuration at an average atom number of 11.4 ± 0.1, below the expected value of 12 atoms. This can be explained by the presence of holes in the highest shell, due to non-adiabatic ramps or heating (atom loss) during the spilling.

The spilling is performed at a magnetic field of 750 G, where the system is strongly interacting. From the radial trapping frequency of $\omega_r \approx 2\pi \times 500\,\text{Hz}$ during

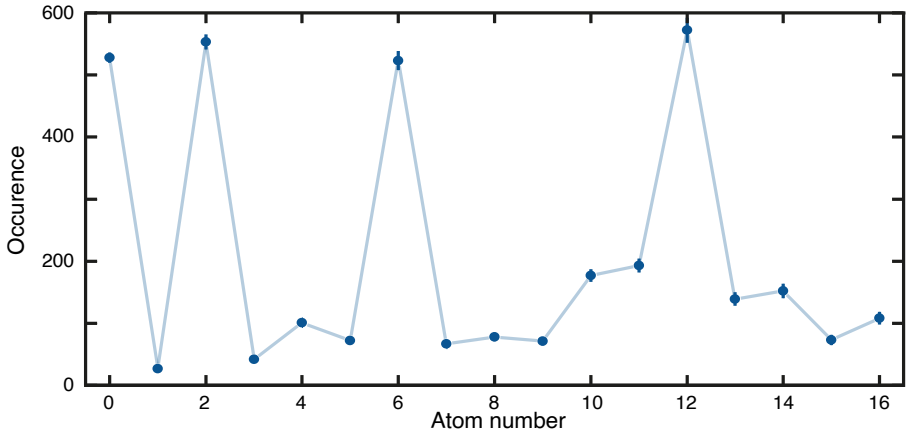

Figure 5.3.: **Histogram of atom numbers.** We plot the number of occurrences for the different atom numbers using the data of all final microtrap depth (data of Fig. 5.2). The atom numbers corresponding to closed shells are observed more frequently. This indicates their enhanced stability when scanning the potential depth in equal steps. Additional holes in the third shell are visible in the enhanced probability of obtaining 10 and 11 atoms. Comparing neighboring atom numbers shows that even atom numbers are more likely than odd. This indicates the presence of substructure in the shells due to the attractive interactions. Error bars give the error of the mean.

spilling, we can estimate the interaction strength[2] using equation (2.28). Within this approximation of a harmonic potential, we obtain a two-particle binding energy of $E_B \approx 0.7\hbar\omega_r$. Even though the interactions are comparable to the trap level spacing, the observed stable atom numbers are given by the shell structure of the non-interacting harmonic oscillator levels. However, when investigating the histogram (Fig. 5.3) of atom numbers over all the microtrap depth used in this measurement, we find some (weak) substructure. The atom numbers corresponding to closed shells of 2, 6 and 12 atoms are most likely. This again demonstrates the enhanced stability of these configurations, when scanning the depth of the optical trap in equal steps. Furthermore, the excess holes in the third shell are visible in the larger occurrence of 10 and 11 atoms compared to the other open shell configurations. In addition to these main features, there is a substructure present and even atom numbers occur more often than odd atom numbers. This provides first indication for the enhanced stability of paired states for attractive interactions, as predicted in [149]. However, we can not rule out that the observed substructure is caused by trap imperfections resulting in a trivial (single particle) splitting of the energy levels within a shell.

[2] As discussed in section 2.3.4, there exists a two-body bound state for any attraction in 2D and we use its binding energy to characterize the interaction strength.

Using this sequence for the preparation of the different shells we obtain preparation fidelities of $97 \pm 2\,\%$, $93 \pm 3\,\%$ and $76 \pm 2\,\%$, for 2, 6 and 12 atoms in the attractive branch (at high magnetic field) respectively.[3] For non-interacting particles the obtained fidelities of $57 \pm 1\,\%$ and $42 \pm 2\,\%$ for 6 and 12 atoms are significantly lower. There are two possible reasons for the reduced fidelities, when initializing the system at a low magnetic field: First, for the non-interacting sample the transfer to a quasi-2D geometry is performed at a magnetic field of 300 G, where the scattering length is maximal for a sample in the repulsive branch. However, interactions at this field are much smaller than at 750 G, which is used for the transfer, when creating a sample with attractive interactions. This results in a smaller coupling of energy levels, when changing the geometry from quasi-1D to quasi-2D and thus, creates additional holes in the lower states.
Second, the spilling procedure itself could be worse for non-interacting samples, which would result in additional atom number fluctuations. Attractive interactions enhance the stability of closed-shell configurations, since they add an attractive density dependent energy shift. This lowers the energy of the interacting system compared to the energy of the non-interacting system in the same external trap and results in a larger energy level splitting of atoms in the different shells [149].
The obtained fidelities for both attractive and non-interacting samples are sufficient for all measurements presented in the following. Non-interacting samples are only used to determine the trap frequencies. Furthermore, for attractive interactions the excitation spectrum for open shells is very different in the frequency range of interest [28]. Hence, experimental realizations with the wrong initial atom number will only contribute a constant background and not add any spurious resonances to the measured spectra.

The demonstrated high-fidelity deterministic initialization of closed-shell configurations of 2, 6 and 12 atoms in a quasi-2D confinement is the first main result presented in this chapter. The access to these ground-state configurations with a non-trivial shell structure opens up a completely new regime of quantum simulation with ultracold atoms, as we will see in the following.

Loading a Single Layer Above we have estimated that the atom cloud size allows us to load a single layer of the SWT. This is verified by the observed stable atom number plateaus, corresponding to the configurations expected for

[3] The data shown in Fig. 5.2 was taken with a slightly different sequence and the preparation fidelity is slightly worse than these optimized values.

the 2D harmonic oscillator. The observation that we load only a single layer can be further substantiated by displaying a Fresnel lens phase pattern on the SLM. This allows us to to shift the z-position of the microtrap focus relative to the SWT layers with sub-micron precision. To find out whether the atoms are transfered to a single or two layers, we employ the spilling sequence which prepares 6 atoms in the quasi-2D geometry. The obtained average atom number in dependence of the z-potions of the microtrap focus is shown in Fig. 5.4. It shows stable plateaus of 6 atoms for focal shifts, where the atoms are loaded into a single layer. If the atoms are split between two layers, the obtained average atom number is sensitive of the exact focal position of the microtrap. In this case a larger average atom number, than the stable closed-shell value of 6 atoms, is obtained. This is due to the independent spilling of atoms trapped in the microtrap in different layers of the SWT. The microtrap depth required for the preparation of 6 atoms is (nearly) the same for neighboring layers of the SWT, as the layer spacing is much smaller than the microtrap beam Rayleigh length of $z_r = \pi w_0^2/\lambda \approx 68\,\mu$m. Once the relative position between the microtrap and the SWT is set, it is stable for several days to weeks. In addition, any drifts are easily visible in the detected number of atoms. While for the experiments presented in this thesis loading a single layer is crucial, future experiments might take advantage of the possibility to create two identical copies for interference or tunneling experiments.

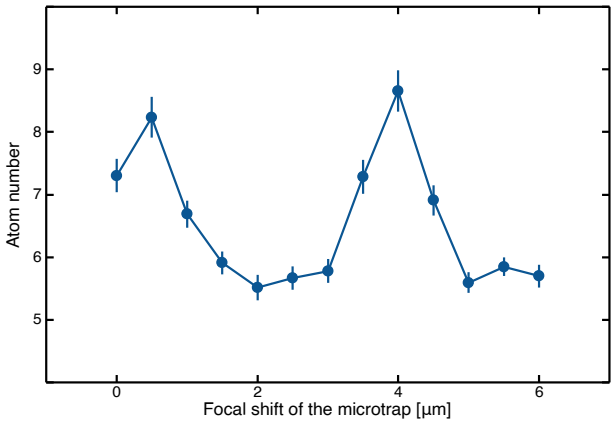

Figure 5.4.: **Shifting the microtrap focus relative to the SWT to load a single layer.** The plot shows the mean atom number after spilling in the quasi-2D configuration for different shifts of the focal position of the microtrap. For focal shifts corresponding to a transfer of the atoms in a single layer of the SWT, stable plateaus of the atom number slightly below the expected value of 6 are observed. This indicates the initialization of a closed-shell configuration in a single layer. For a focal shift such that two layers are loaded, the average atom number strongly depends on the focal position. Here, larger atom numbers are obtained for the same final microtrap depth due to the independent spilling of atoms in different layers. The periodicity of the SWT is clearly visible.

Characterizing the Potential We perform spectroscopy on non-interacting samples to characterize the final trapping potential. In the final configuration the axial trap frequency due to the microtrap is a factor of 100 smaller than the axial trap frequency of the SWT. Thus, the axial confinement is solely defined by the SWT and results in an axial trap frequency of $\omega_z = 2\pi \times (6.80 \pm 0.05)\,\mathrm{kHz}$. This value is measured by modulating the power of the SWT and counting the remaining atoms in the ground state as discussed in section 4.5.2.
The structure of radial trap levels is deduced from spectra taken by modulating the microtrap power. This modulates the radial trapping frequencies and results in excitations of particles two shells up ($\Delta n = 2$). We take spectra for 6 and 12 atoms, i.e. two and three filled shells. The spectra shown in Fig. 5.5 show several resonances. The presence of more than a single resonance is due to the anharmonicity of the trap, which results in an unequal energy spacing between the different shells and lifts the degeneracy of states in a single shell. The lifting of the degeneracy can be understood from the fact that states in the same shell, but with different absolute value of the angular momentum $|L_z|$ probe different regions of the anharmonic potential and are thus not degenerate in the anharmonic potential. Note that for the 12 particle system, it is not possible to excite atoms in the lowest shell as the states in the third shell are already occupied.
The radial trapping frequencies are $\omega_r \approx 2\pi \times 1.0\,\mathrm{kHz}$, with the excitation from the lowest shell (n=0) two shells up being approximately 10 % larger than the excitation from the second shell (n=1) two shells up. This value for the anharmonicity matches the spectrum obtained by numerically solving (by exact diagonalization on a grid) the 2D Hamiltonian, where we assume a Gaussian of width $4.8\,\mu\mathrm{m}$ for the confining potential. Due to the finite potential depth there are only five well-defined shells of bound states within the 2D Gaussian potential. In the following, we take the lowest monopole resonance of the 6 (12) particles system at 2001 Hz (1984 Hz), as the reference value for twice the trap frequency. Thus, for all spectra taken with 6 (12) atoms we normalize all excitation frequencies by $\omega_r = 2\pi \times 1001\,\mathrm{Hz}$ ($\omega_r = 2\pi \times 992\,\mathrm{Hz}$).

In addition, we measure the anisotropy of the trap, by modulating the trap center position. This is done by modulating the rf frequency of the AOD in the microtrap beam path (see chapter 4). The resulting time dependent Hamiltonian is

$$\hat{H} = \frac{p^2}{2m} + \frac{1}{2}m\omega^2(x + \epsilon\sin(\omega_{ex}t))^2 \approx \frac{p^2}{2m} + \frac{1}{2}m\omega x^2 + m\omega^2 x\epsilon\sin(\omega_{ex}t), \quad (5.2)$$

where ϵ describes the shift of the potential center due to modulation of the rf frequency. This perturbation has odd parity ($\propto x$) and thus results in excitations one shell up ($\Delta n = 1$). From the two resonances of exciting two non-interacting particles in the ground state one shell up, we obtain a trap anisotropy of $(\omega_x - \omega_y)/(\omega_x + \omega_y) = 0.02$. This small anisotropy has two effects: First, it gives rise to a small splitting of the energy levels within a shell. Second, it slightly breaks the rotational symmetry of the trap. As we will see below, this results in a coupling of the different angular momentum states and thereby gives spectral weight to excitations, which are forbidden in the round trap.

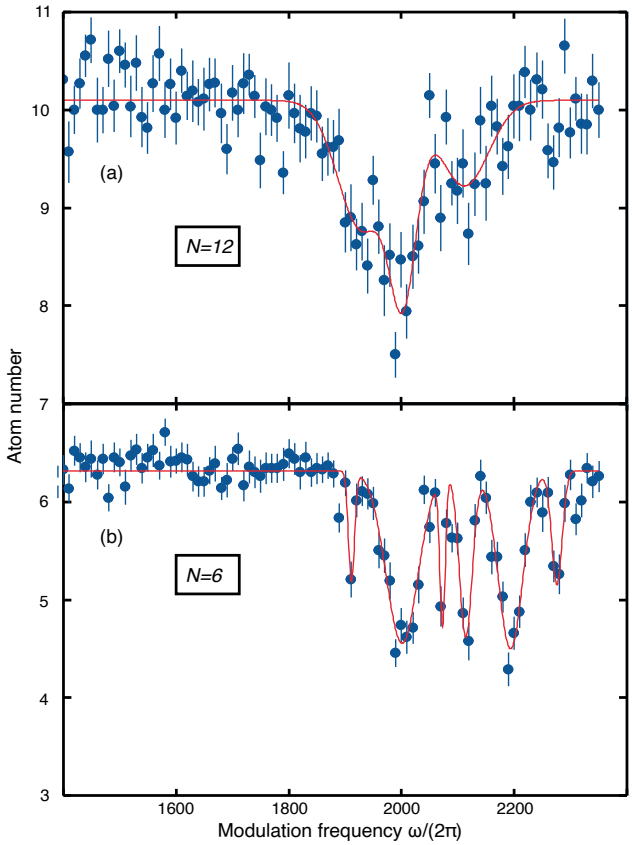

Figure 5.5.: **Excitation spectrum of non-interacting particles.** Mean atom number after modulating the radial confinement and removing excited atoms for a non-interacting sample ($B = 568\,\mathrm{G}$). The excitation spectra are measured for systems initialized with $N = 12$ (a) and $N = 6$ (b) atoms. The presence of more than one resonance is due to the anharmonicity and anisotropy of the potential. Each data point is the average of 27 (a) or 73 (b) measurements.

5.2. Emergence of Collective Excitations

The created closed-shell configurations, corresponding to miniature versions of a Fermi sea, are an interesting starting point to study the emergence of collective behavior due to attractive interactions. In contrast to open-shell systems, where the only relevant energy scale is given by the interactions, the physics of closed-shell configurations is determined by the interplay between the interactions and the gap in the single-particle spectrum. As discussed in section 2.4.5 the competition of these two scales results in a normal- to superfluid transition for attractive fermions, with observable precursors in the few-body limit [28]. We study this interplay experimentally by performing spectroscopy on the closed-shell configurations.

5.2.1. Excitation Spectrum

In cold atom experiments different types of excitation schemes are available to excite the system. Since, in the following, we are interested in pair excitations, we modulate the interaction strength. This perturbation couples strongly to collective pair excitations [28]. In principle, modulating the interactions can be done by modulating the magnetic field close to the Feshbach resonance. However, the required frequencies of up to 2000 Hz make a modulation of the magnetic field difficult due to the inductance of the coils. Additionally, the non-linear dependence of the interactions on the magnetic field close to the resonance further complicates this driving scheme. A more convenient way to modulate the effective 2D interactions is to change the depth of the axial confinement. The spectrum of two interacting particles in a harmonic trap is given by equation (2.28). One finds that the energy of the interacting two-particle states and, hence, the effective interaction strength depends on the ratio of the axial confinement length and the scattering length only. In the experiment, we modulate at frequencies close to the radial trapping frequency and, thus, far below the band gap of the system along the z-axis. Hence, the wavefunction along the z-axis follows the change of the potential adiabatically and the only effect is the modulation of the effective 2D interaction strength. We modulate the depth of the SWT by 5 %, which changes the binding energy by $\Delta E_\mathrm{B}/E_\mathrm{B} \approx 1.6\,\%$ (the exact value depends weakly on the magnetic field). As this modulation is spatially isotropic it does not add angular momentum and drives only monopole excitations.

We measure the excitation spectrum using the following procedure: First, we create a closed-shell configuration of 6 atoms as discussed above. We then ramp the magnetic field to set the interaction strength. Afterwards, we modulate the in-

teractions sinusoidally at a drive frequency f_{ex} for 400 ms. In the end, we remove all excited atoms by a second spilling procedure to the same microtrap depth as in the first spilling and count the remaining atoms in the MOT.

For each drive frequency, we repeat the experiment 45 times and obtain an atom number distribution as shown in Fig. 5.6 (c) and (d) for two different drive frequencies. The full spectrum for all measured frequencies is shown in Fig. 5.6 (e). This spectrum is taken at an interaction strength of $E_{\mathrm{B}} = 0.33\hbar\omega_r$. There are two resonances visible in the spectrum. The higher lying resonance (Fig. 5.6 (d)) at $\omega_{\mathrm{ex}} = 2\pi \times 2060\,\mathrm{Hz}$ is observed at a larger frequency than the lowest non-interacting monopole resonance at 2000 Hz. This can be explained by a mean-field shift due to the attractive interactions: At the mean-field level, the interaction energy is proportional to the interaction strength and the density (see section 2.3.3). Therefore, the gain in interaction energy is larger for the denser ground state than for the more dilute excited state. This results in the observed increase of the effective trapping frequency.
In addition to the resonance position, the obtained full counting statistics also reveals more details about the nature of the excitation. From the atom number distribution (Fig. 5.6 (d)), we can conclude, that the resonance at $\omega_{\mathrm{ex}} = 2\pi \times 2060\,\mathrm{Hz}$ consists of single particle excitations as the probability for both $N = 4$ and $N = 5$ atoms is enhanced. We find that $P_{N=4} \ll P_{N=5}$ and $P_{N=4} \approx P_{N=5}^2$. This indicates that the spectrum is linear and for the chosen drive strength and time it is possible to excite either one or two atoms.
The position of the lower resonance at $\omega_{\mathrm{ex}} = 2\pi \times 1890\,\mathrm{Hz}$ (Fig. 5.6 (c)) is not explained by the simple mean-field picture, as it lies below the lowest non-interacting resonance. Furthermore, the atom counting statistics are strikingly different and only the probability of obtaining $N = 4$ atoms is enhanced. Thus, at this frequency it is only possible to excite a pair of atoms!
Both the lower frequency and the pair character can be understood from the interplay of the attractive interactions and the finite single-particle gap of the closed-shell configuration. As the interaction strength $E_{\mathrm{B}} = 0.33\hbar\omega_r$ is smaller than the energy spacing between the different shells, pairing in the completely filled shell is suppressed by Pauli blocking. Considering two atoms in the highest shell, we see that there are no empty energy levels in this shell as all other states are blocked by the other atoms. Thus, there are no degenerate states available for the two atoms to increase their overlap and thereby gain additional pairing energy due to the attractive interactions. However, if a pair of particles is excited at the same time, the atoms remaining in the lower shell can use the now

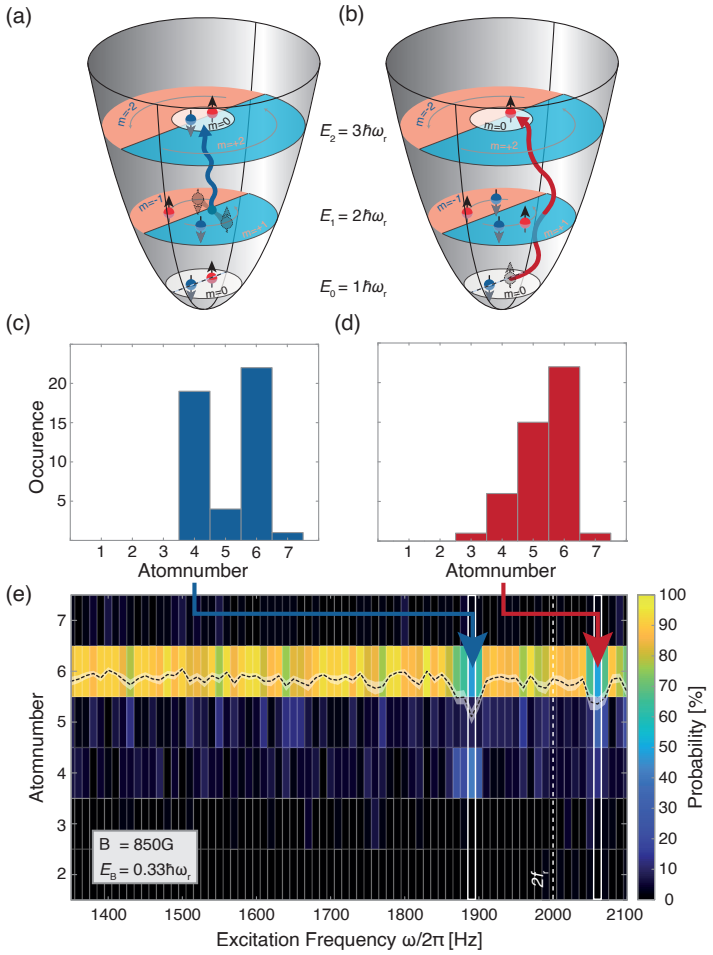

Figure 5.6.: **Excitation spectrum for a system initialized with 6 atoms.** The system is excited by modulating the effective 2D interaction strength. Excited atoms are removed by a second spilling step and the remaining atoms in the lowest two shells are counted. The spectrum in (e) shows the probability P_N of detecting N atoms as function of the modulation frequency. There are two resonances at 1860 Hz and 2060 Hz visible. The corresponding occurrences of different atom numbers for theses frequencies are shown in (c) and (d) respectively. These resonances correspond to pair and single particle excitations as clearly visible in the full counting statistics and sketched in (a) and (b). Panels (a), (b) and (e) adapted from [93].

free states to increase their overlap and gain pairing energy. Additionally, the excited particles can effectively form a pair in the otherwise empty shell and, hence, have a lower energy than two non-interacting particles in the same shell. Since this gain of paring energy supersedes the relative mean-field shift between the two configurations, the frequency of the pair excitation lies below twice the non-interacting trap frequency. This correlated nature of the excited state also explains why the response of the system is very nonlinear at this frequency. As there is no comparable energy gain due to pair correlations when exciting a sec-

ond pair, it is only possible to excite a single and not two pairs when driving the system at this frequency. Note that due the gapped single particle spectrum, the system has a reduced tendency to form pairs at weak attraction.

5.2.2. Tuning Interactions

In order to study the competition between the single particle gap and the interactions in more detail, we tune their relative strength by using the Feshbach resonance at 690 G and take spectra at different interaction strengths. The obtained spectrum as function of frequency and interactions is shown in Fig. 5.7. Since we are mainly interested in the evolution of the collective pair excitation, we plot the probability of detecting $N = 4$ atoms $P_{N=4}$ divided by the probability of retaining $N = 6$ atoms $P_{N=6}$. We normalize the spectra at each interaction strength to the maximum of the lower pair excitation at this interaction. Consequently, the spectrum contains no information about the relative strength of the pair excitation at different binding energies. But, as we discuss in more detail in section 5.3, the used modulation parameters are chosen to optimize the visibility of the pair excitation and do not allow for an extraction the coupling strength. The spectra for all atom numbers are shown in appendix A.

The spectrum in Fig. 5.7, allows us to track the evolution of the different peaks discussed above. The frequency of the higher lying (single particle) excited peak is monotonously increasing with attraction, as expected from the larger mean-field energy for increasing attraction. Interestingly, the two modes below the lowest monopole resonance show a *non-monotonous* frequency dependence on the interaction strength. Comparison to configuration interaction calculations shows, that they correspond to pair excitations with total angular momentum $L_z = 0$ and $L_z = \pm 2\hbar$. The energies of these modes decrease with attraction for weak interactions. This can be understood by considering the larger pair correlations in the excited state [28] and the increase in pairing energy with attraction.

When the two-body binding energy becomes comparable to the single particle spacing this picture breaks down. For these interaction strengths it becomes favorable to admix states from higher lying shells and thereby increase the overlap between the particles to gain additional interaction energy. Thus, already the closed-shell ground state has sizable pairing correlations.[4] This is also visible in the spectrum, where above an interaction strength of $E_B \approx 1.2\hbar\omega_r$, the frequency

[4] The admixture of higher lying single particle states could be measured directly in a future experiment by projecting the system on a non-interacting state. This can be achieved by removing one hyperfine state with a short resonant light pulse [150] and a subsequent spilling to the different trap levels before counting the remaining atoms.

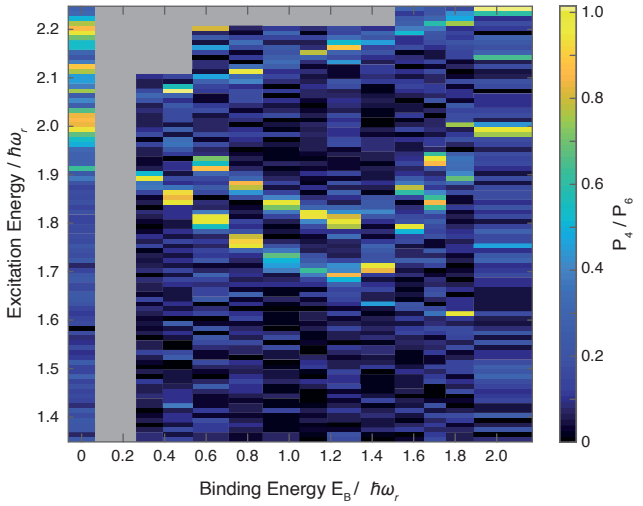

Figure 5.7.: **Six particle excitation spectrum as function of modulation frequency and interaction strength.** The excitation spectrum shows the probability of detecting $N = 4$ atoms $P_{N=4}$ divided by the probability of detecting $N = 6$ atoms $P_{N=6}$. Each column is normalized to its maximum. The spectrum is obtained by modulating the effective 2D interactions for all binding energies, except $E_\mathrm{B} = 0$, where the system is excited by modulating the depth of the radial confinement. For this interaction strength the color shows the normalized probability of exciting a particle. The energies of the two lowest pair excitation modes show a *non-monotonous* interaction dependence. The spectrum for all atom numbers can be found in appendix A and clearly corroborates the picture that the non-monotnous modes are pair excitations. Figure adapted from Ref. [93].

of the lowest modes starts to increase with increasing attraction. This position of the minimal excitation gap is used to define the critical binding energy (interaction strength).

In addition to this few-body picture, the behavior of the pair excitation mode can also be understood from a many-body perspective. As discussed in Ref. [27], closed-shell configurations of harmonically trapped 2D Fermi gases with attractive interactions undergo a quantum phase transition from a unpaired normal to a paired superfluid (BCS) state upon increasing the attraction. This phase transition results in the emergence of collective degrees of freedom corresponding to excitations of the order parameter (pair density). When approaching the critical point the excitation energy of these modes decreases and goes to zero exactly at the critical point, indicating the instability towards the formation of Cooper pairs. The order parameter (pair density) is zero in the normal phase and obtains a finite value in the symmetry broken phase. The energy of exciting

the amplitude of the pair density around its mean value has a non-monotonous interaction dependence, with the energy gap closing at the critical point [27]. In the superfluid phase this amplitude excitation of the order parameter (excitation of coherent pairs) is commonly referred to as a Higgs mode.
The experimentally observed pair excitations are exactly the few-body remnants of this amplitude excitation. In the finite size 6 atom system the critical region gets broadened to a crossover and one observes a non-monotonous energy dependence of the pair excitation mode on interactions instead of the non-analytic behavior in the thermodynamic limit. Due to the finite size, the excitation gap does not close at the critical interaction strength but retains a finite value for 6 particles. Furthermore, the non-monotonous excitation is a pair excitation as expected for the few-body precursor of the amplitude excitation of the order parameter (pair density). For the $N = 6$ atom system the minimum of the pair excitation is obtained for a binding energy of $E_{\mathrm{B}} \approx 1.1\hbar\omega_r$. Thus, the small system size shifts the critical interactions strength to a large value compared to the many-body limit, where the critical interaction strength approaches zero [27].

The interpretation that we observe the few-body precursor of a phase transition is further solidified by a numerical diagonalization of the microscopic Hamiltonian preformed in Ref. [28]. They solve the microscopic Hamiltonian for 6 fermions in a harmonic trap in 2D and observe a non-monotonous pair excitation mode corresponding to zero angular momentum pairs. To gain further insight into the spectra shown in Fig. 5.7, they also calculated the spectrum for an anharmonic and anisotropic trap. The resulting spectrum is shown in Fig. 5.8 (a) and shows two non-monotonous modes as observed in the experiment. While the numerical calculation is able to explain the presence of both excitation branches and the coupling strengths only qualitative agreement could be reached, when comparing the excitation energies to the experiment. This has several reasons: For the highest possible energy cut-offs (corresponding to approximately 10 million basis states) the numerical spectra are not fully converged,[5] even if harmonic oscillator levels up to the tenth shell are included and the calculation includes more shells than actually present in our finite depth trap. This shows that reaching quantitative agreement is difficult in any case due to the sensitivity to high lying states. In the experiment we do not know the spectrum for the high lying states in our trap very well. Close to the edge of the trap, the potential is very sensitive to experimental imperfections and could have a different shape than what we would naively assume. Furthermore, at these high energies, the third direction of our

[5]However, the pair excitation mode is robust and deepens for increasing basis set size.

trap with an aspect ratio of approximately 1 : 7 plays an important role, but calculations for a 3D geometry are currently not possible due to the much larger Hilbert space size. Nevertheless, the numeric spectra show all qualitative features observed in the experiment and confirm our interpretation.
The insensitivity of the qualitative features to the exact microscopic details of the potential (harmonic or anharmonic) is interesting, as it shows that the pair excitation and the few-body precursor of the phase transition are robust phenomena and do not depend on a fine tuning of the parameters.
Note that due to high degree of collectivity it is extremely challenging to numerically calculate the full spectrum for a system consisting of only 6 particles in a realistic trap. Hence, our experiments enter a regime of non-trivial quantum simulation.

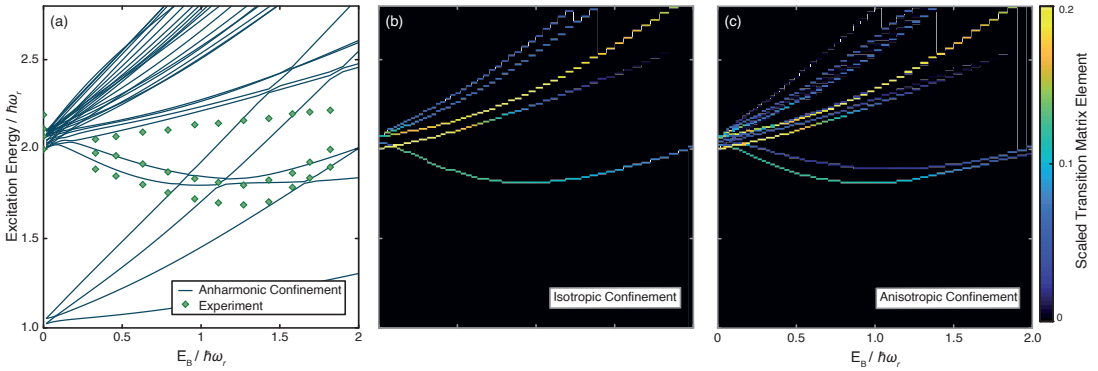

Figure 5.8.: **Numerically calculated excitation spectrum for 6 particles.** (a) Numerically obtained excitation spectrum for 6 particles in an anharmonic and anisotropic trap. As in the experimental data, we observe two non-monotonous pair excitation modes. For a comparison we plot the experimentally obtained peak positions of the different excitation branches (green diamonds). The numerically calculated excitation spectrum, weighted with the coupling strength of the respective state to the ground state for a modulation of the interactions, is shown for a round (b) and anisotropic (c) trap. The modes corresponding to excitation of a single particle one shell up do not couple to this probe, as they correspond to excitations with $\Delta L_z = \pm\hbar$. In the anisotropic trap both pair excitation modes are excited by an interaction modulation. The numerical data is obtained for a small anisotropy of 0.5 %. Due the demanding calculations of the transition matrix elements, the number of basis states in the calculations for panel (b) and (c) is smaller than in (a) resulting in different frequencies for the modes. The calculations are extracted from Ref. [93]. Figure adapted from Ref. [93].

From the numerical spectrum, we find that the experimentally observed pair excitation branches correspond to coherent pairs with total angular momentum $L_z = 0$ and $L_z = \pm 2\hbar$. The pair excitation branch higher in energy actually consists of two different states with $L_z = \pm 2\hbar$. The small anisotropy of the trap

results in a weak splitting of these two modes, below what we can experimentally resolve and the two modes show up as a single branch in the spectrum. In the many-body limit, these modes correspond to Cooper pairing at finite angular momentum. However, as these excitations have larger energy than the zero angular momentum pair excitation, the system becomes unstable to pairing at zero angular momentum first and the ground state of the superfluid, always consist of zero angular momentum Cooper pairs.
The modulation of the interactions does not impart angular momentum on the atoms. However, the anisotropy of our trap results in a coupling of the $L_z = 0$ and $L_z = \pm 2\hbar$ states. This results in the experimentally observed coupling to the different pair excitation modes and gives spectral weight to the non-zero angular momentum modes.[6] This is clearly visible in the numerically calculated excitation spectra in Fig.5.8 (b) and (c) for a round and an anisotropic trap. Comparing the two spectra shows that the higher angular momentum modes are only visible in the anisotropic trap. In the plot, the color encodes the coupling strength $\Gamma^E_{int} = |\langle G| \sum_{k,l} \delta(\mathbf{r}_k - \mathbf{r}_l)|E\rangle|^2$ of the excited states $|E\rangle$ to the ground state $|G\rangle$ when modulating the interactions.

5.2.3. Comparing Different Excitation Schemes

In solid state systems it is often challenging to excite the amplitude mode of the order parameter, as there is no first-order coupling to the probes conventionally used in these systems [51]. This is the big advantage of ultracold atoms, where one can directly modulate the interaction or pairing strength [62].
We compare the excitation of the system with a single-particle operator (modulating the radial trap frequency) to a excitation of the system with a two-particle operator (modulating the interaction strength). The obtained spectra at an interaction strength of $E_\mathrm{B} \approx 0.1\hbar\omega_r$ are shown in Fig. 5.9. Here, it is clearly visible that the interaction modulation couples strongly to the lowest pair excitation mode and only has a weak coupling to the single-particle excited states above twice the trap frequency. Conversely, modulating the radial trap depth results in a strong coupling to the single-particle excitations. This shows the special character of the pair excitation mode, which couples strongly to the interaction modulation.

[6] In the anisotropic trap, angular momentum is not a good quantum number anymore. For the small anisotropy of our trap we still label the states by the angular momentum that their corresponding states would have in the round trap.

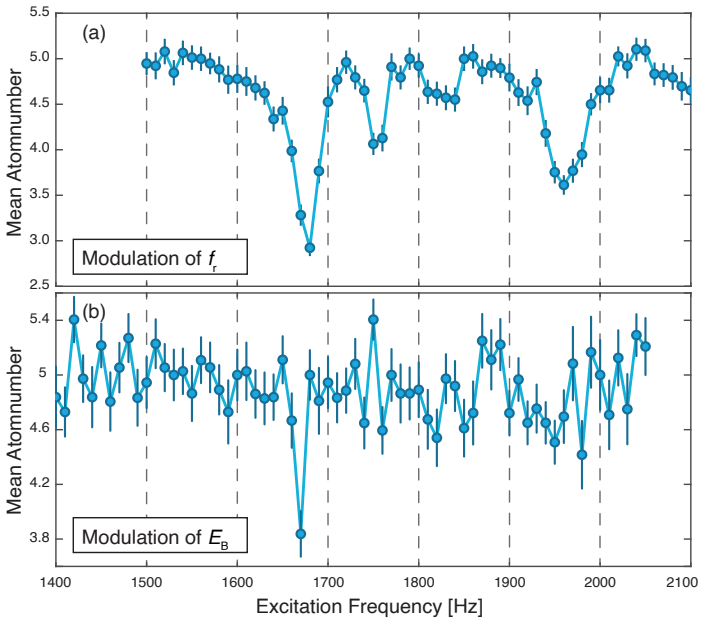

Figure 5.9.: **Comparing spectra for interaction and trap frequency modulation.** Excitation spectrum for a modulation of the radial trap frequency (a) and the 2D interaction strength (b). Modulating the trap depth couples strongly to the higher lying single particle excitations (a). The relative strength of the excitations for a modulation of the interaction strength shows the strong coupling to the pair excitation mode when modulating the interactions. Note that for the chosen modulation parameters (see section 5.3) one would expect a equal superposition of the excited state and the ground state, when resonantly driving the pair excitation mode. This equal superposition of the ground and the excited state should reduce the average atom number by 1, consistent with the amplitude of the resonance in (b). The radial trap frequency was $2\omega_r = 2\pi \times 1660\,\mathrm{Hz}$ for this measurement. Figure taken from Ref. [93].

5.2.4. Approaching the Many-Body Limit

In the last section, we found that already a system consisting of 6 particles shows collective excitations, which can be understood as few-body signatures of a quantum phase transition. To investigate how the excitation spectrum depends on the system size and how it approaches the many-body limit, we study the excitation spectrum for the other available closed-shell configurations.

First, we take a step back and study the smaller closed-shell system of only $N = 2$ particles. From the exact solution of equation (2.28) and since (in the harmonic trap) the two-particle problem can be mapped to a single-particle problem for the relative motion, we do not expect any non-monotonous pair excitation modes. This is experimentally verified by the spectrum shown in Fig. 5.10. We observe two modes that both have a monotonous dependence on the interaction strength. The higher lying mode corresponds to the excitation of the relative motion and

its energy is described by equation (2.28). Since the excited branch energy is also shifted by interactions, the excitation energy is significantly smaller than the sum of the non-interacting trap frequency plus the binding energy. Comparing the measured excitation energy to the excitation energy calculated from equation (2.28) (red line in Fig. 5.10) shows good agreement. This agreement between the harmonic theory and measurements in the anharmonic trap, shows that the harmonic theory can be used to calculate the two-body binding energy. Due to the anharmonicity of the potential, also the center of mass motion (lower branch) of the two particles can be excited when modulating the interactions. The slight increase of excitation energy with attractions can be understood from the decreasing size of the atom cloud for larger attraction. Thus, a smaller region of the anharmonic trap is probed for larger attraction. This results in an apparent increase of the trap frequency.[7] Above a binding energy $E_B \approx 1.2\hbar\omega_r$ the coupling to this mode becomes weaker. This might be due to a decoupling of the relative motion of the tightly bound molecule from the center of mass motion for large binding energies, even in the anharmonic trap.

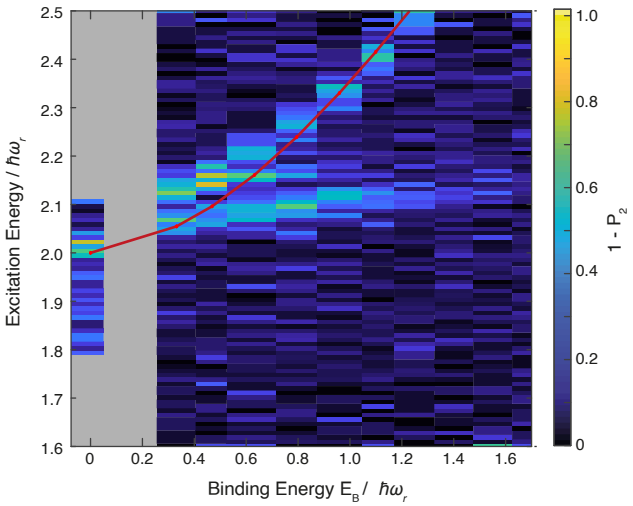

Figure 5.10.: **Excitation spectrum for two particles as function of interaction strength and modulation frequency.** The color map shows the probability of exciting the system during modulation. As expected, the excitation energies for all modes increase with increasing attraction. The red curve gives the excitation energies calculated from the magnetic field, the axial and radial trap frequencies by using equation (2.28). We observe good agreement between this theory for a harmonic trap and the measurement in an anharmonic confinement. The spectrum is obtained by modulating the effective 2D interactions for all binding energies, except the data for $E_B = 0$, where the system is excited by modulating the depth of the radial confinement.

[7] See Ref. [83] for the observation of the same effect in a many-body system.

Going to larger system sizes, we study the closed-shell configuration of 12 atoms. The excitation spectrum for the system initialized with $N = 12$ atoms is shown in Fig. 5.11 (a). The spectrum shows the same qualitative features as for $N = 6$ particles. However, there are two quantitative differences: First, the single particle excitation branch, above twice the trap frequency, is broadened due to the larger number (density) of excited states for 12 than for 6 atoms. This makes it impossible to resolve a single well-defined excitation for 12 atoms in this frequency range. Second, when comparing the minimum of the pair excitation for 6 and 12 atoms in Fig. 5.11 (b), we find that the minimum of the 12 atom pair excitation mode is much deeper than the minimum in the 6 particle measurement and that it shifts to smaller interactions. Both effects can be explained by referring to the many-body picture. Increasing the system size results in a smaller minimal exaction gap of the system, consistent with the complete closing of the gap at the critical point in the thermodynamic limit. Also the shift of the critical interaction strength to smaller values for larger systems is expected [27, 28]. Intuitively, this is understood from the increasing Fermi energy, which reduces the relative importance of the fixed single-particle gap. Hence, the critical point moves to smaller attraction for increasing system size until BCS theory is recovered and the system is superfluid for any attraction (larger than an infinitesimal small critical value, as can be seen from equation (2.43)).

5.3. Coherent Control of Strongly Interacting Fermions

For all interaction strengths shown in Fig. 5.6 and Fig. 5.11 the pair excitation is a well-defined mode with a small width compared to its frequency. We measure a width below 15 Hz for all interaction strengths and the chosen drive parameters. We probe the stability of the excited state in more detail, by driving the $N = 6$ particle system (at $E_{\mathrm{B}} = 0.57\hbar\omega_r$) for a variable time at the frequency of the lower pair excitation mode (1480 Hz). The drive strength used corresponds to a modulation of the binding energy of 3 %. We observe a coherent oscillation between the probability of detecting 4 and 6 atoms as a function of the drive time (see Fig. 5.12), whereas the probabilities for all other atom numbers are (nearly) flat. This demonstrates that we are able to control the *quantum state* of a strongly interacting mesoscopic fermionic system and can coherently create and annihilate a pair in the excited state. Since the combined probability of detecting either 4 or 6 atoms is constant and both probabilities decay to the same value, we

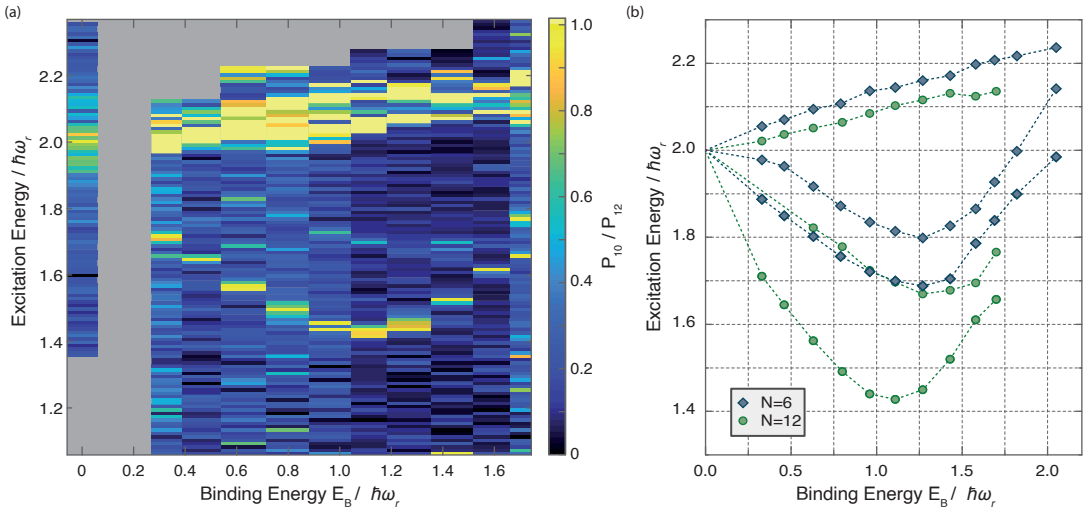

Figure 5.11.: **Excitation spectrum for 12 particles as function of interaction strength and modulation frequency.** (a) The excitation spectrum shows the probability of detecting 10 atoms $P_{N=10}$ divided by the probability of retaining 12 atoms $P_{N=12}$. Each column is normalized to the maximum of the lowest mode. The spectrum is obtained by modulating the effective 2D interactions for all binding energies, except for $E_\mathrm{B} = 0$, where the system is excited by modulating the depth of the radial confinement. For this interaction strength the color shows the normalized probability of exciting a particle. We observe two non-monotonous pair excitation modes below twice the non-interacting trap frequency. The spectrum for all atom numbers can be found in appendix A and clearly shows the pair character of the non-monotonous modes. For a quantitative comparison of the spectra obtained for the systems initialized with $N = 6$ and $N = 12$ atoms, we plot the positions of the different resonances for both systems in (b). The resonance positions are obtained by fitting a Gaussian to each resonance. The uncertainty of determining the peak position from the fit is smaller than the symbol size. The comparison shows that the minimum of the pair excitation deepens and moves to smaller interaction strengths, when increasing the system size. Figure adapted from Ref. [93].

can treat the lowest pair excitation and the ground state as a two-level system, with negligible coupling to other states. We fit the probability to detect 6 atoms $P_{N=6}$ with a damped Rabi oscillation[8]

$$P_{N=6}(t) = a + C \exp(-\gamma t) \cos^2(\Omega t/2), \tag{5.3}$$

and obtain a Rabi rate of $\Omega = 2\pi \times (8.0 \pm 0.1)\,\mathrm{Hz}$ and a damping rate of $\gamma = 4.5 \pm 0.5\,\mathrm{Hz}$. The long coherence time of $\tau = 1/\gamma = 222 \pm 25\,\mathrm{ms}$ exceeds the frequency of the excited state by more than a factor 300 and allows us to perform

[8] We also tested different envelope functions, as we do not know the exact line shape of the excitation (spectrum of the noise). However, we did not find any significant difference, between the different models.

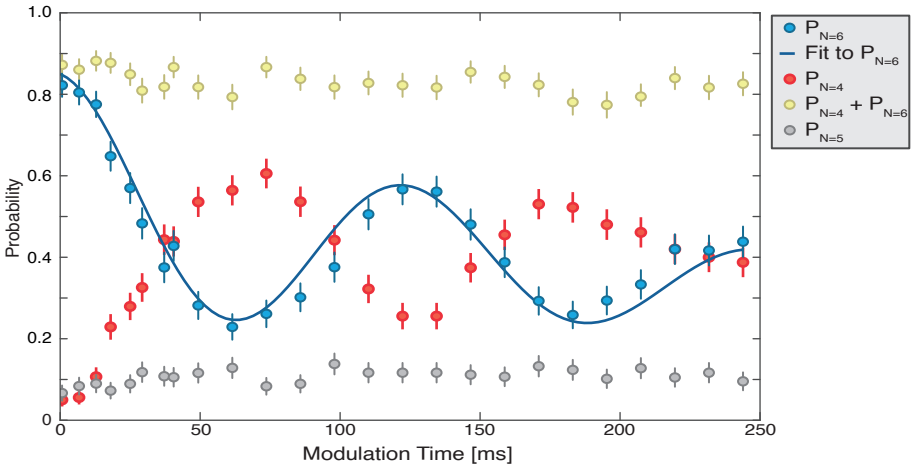

Figure 5.12.: **Coherent driving of the lower pair excitation.** The system initialized with $N = 6$ atoms is excited by modulating the interaction strength for a variable time. We drive the system at the resonance frequency of the lower pair excitation mode (1480 Hz). The coherent oscillation between the probability of detecting 4 and 6 atoms clearly shows the pair character of the excitation. We fit a damped Rabi oscillation (equation (5.3)) to the $N = 6$ atom data. The data is taken at an interaction strength of $E_B = 0.57\hbar\omega_r$. For each modulation time we take 180 measurements. Figure adapted from Ref. [93].

coherent manipulation of a interacting many-body system despite the small Rabi rates. The observed coherence time τ is consistent with the observed long time stability of the trap frequency. The stability of the excited state is due to the discrete level spectrum of the trap, which limits possible decay channels [27] and not due to the presence of additional symmetries of the system, which are usually required for the stability of the Higgs mode [68].

From the obtained parameters of the coherent oscillation, it is clear that the spectra discussed above (Fig. 5.7 and Fig. 5.11) do not contain much information about the coupling strength between the ground and lowest excited state. In these measurements the system was driven for 400 ms, which is a factor of approximately 2 times larger than the measured coherence time τ of the oscillation. Thus, for this data dephasing of the oscillation results in an incoherent superposition of both states with equal probability. This does not depend on the coupling strength (as long is the Rabi rate is large enough). This is confirmed by the full counting statistics shown in appendix A, where the probability for detecting 4 and 6 atoms are approximately equal for frequencies corresponding to the pair excitation mode. In order to obtain the coupling strength at each interaction strength, one could repeat the measurement of the Rabi rate for different interaction strength in a future measurement.

Conclusion In conclusion we have created low-entropy, few-fermion systems in a quasi-2D geometry. Combining these deterministically initialized systems with the tunability of the interactions allowed us to observe the few-body precursor of a quantum phase transition.

In a first set of experiments, we observed the enhanced stability of closed-shell configurations when scanning the depth of the confining potential. This enhanced stability allows us to initialize closed-shell configurations of 2, 6 and 12 atoms with high fidelity.

In a second step, we used these closed-shell configurations to investigate the interplay of the single-particle gap with the attractive interaction. The system is studied by modulation spectroscopy, where the full counting statistics reveal pair excitation modes with a non-monotonous interaction dependence. By comparing to numerical simulations and many-body theory, we identify them as the few-body precursors of the amplitude excitation of an order parameter. This identification as the few-body precursor of a Higgs mode allows us to observe the few-body precursor of a normal to superfluid phase transition. Comparing spectra for different atom numbers, allows us to investigate the transition for different system sizes. Here, we observe a deepening of the pair excitation mode for larger systems, which serves as a first indication for the approach towards the many-body limit. Finally, the achieved degree of control in our experiment allows us to coherently manipulate the quantum state of a mesoscopic strongly interacting fermionic system.

6. Observing a Pauli-Crystal

In the last chapter we presented our measurements studying the few-body precursor of a phase transition. We have measured the excitation spectrum and information about the system has been extracted by counting the number of atoms in the trap below a certain energy. For the experiments we present in this chapter we go beyond atom counting and measure the momentum distribution of the atoms using the method described in section 4.3.2. Currently, this imaging scheme is limited to taking a single image in each experimental realization, i.e. we can extract information about only a single hyperfine state in each realization. Hence, we cannot access correlations between different hyperfine states and, for now, restrict the measurements to non-interacting samples. For these systems the momentum distribution of the different hyperfine states is independent and the momentum distribution of a single state contains all information. The results presented in this chapter have been published in Ref. [151].

Usually, the emergence of correlations and geometric structures is driven by interactions. The most prominent example is symmetry breaking in solid-state systems, where repulsive interactions between the ion cores dominate the system and result in the emergence of a crystal structure.
More exotic crystalline structures observed in finite systems include: a Wigner crystal of a dilute 1D electron gas [152], Coulomb crystals observed in ion trap experiments [153, 154] and spatial structures in the Rydberg excitation pattern of a Mott insulator of ultracold Rubidium [155]. All these examples have in common that the repulsive interactions dominate all other energies scales (kinetic energy and temperature) of the system.
However, correlations and spatial structures can also arise from quantum statistics. The structure of a system of identical fermions is determined by the antisymmetry of the wavefunction, which results in Pauli blocking and anti-bunching [156]. For non-interacting fermions in periodic potentials their quantum statistics gives rise to a band insulator at unity filling [157]. The influence of fermionic statistics has also been observed in density correlations of ultracold atoms released from a periodic potential [137, 158]. For these quantum effects to have

an observable consequence the distance of the particles has to be comparable to their wavelength.
Here, we study the effect of Fermi statistics on the density distribution of non-interacting (ground-state) samples in the quasi-2D harmonic oscillator. The fermionic many-body wavefunction is given by the Slater determinant of the single-particle wavefunctions.[1] This results in correlations between the position of the individual particles and the emergence of geometric structures without interactions. These geometric structures were first discussed in Ref. [159, 160] and termed 'Pauli crystals'. The requirement to produce low-entropy, non-interacting samples makes their experimental observation very challenging.
The 2D harmonic confinement used in the experiment is rotationally symmetric. Hence, the atoms are measured along a random axis in each experimental realization and it is not sufficient to simply measure the density distribution to reveal the structure caused by the exchange symmetry. Instead, we have to probe the correlations between the atoms.

6.1. Sampling the Many-Body Wavefunction

We start the experiment with non-interacting closed-shell configurations consisting of $N = 3$ or $N = 6$ fermions per spin state (see chapter 5). We probe the momentum distribution of the atoms in state $|3\rangle$. To this end, we apply a matter-wave focusing technique (section 3.6) consisting of a 12 ms expansion in the SWT trap ($\omega_{\mathrm{tof}} = 2\pi \times (20.7 \pm 0.5)$ Hz) at a magnetic field of $B = 568$ G and image the sample in free space subsequently. This allows us to sample the the many-body momentum distribution.
After the atom identification, which is performed as described in section 4.3.2, we only keep measurements, where an atom number corresponding to the initialized closed-shell configuration of $N = 3$ or $N = 6$ is detected. This yields post selection rates of 30 % in agreement with the combined imaging and preparation fidelity at low magnetic fields. To reveal the structure emerging from quantum statistics we follow the image processing procedure described in Ref. [160]:

- First, the center of mass momentum of the atoms in each realization is aligned, i.e. the center of mass is shifted to the image center. The center of mass distribution over all experimental realizations is a Gaussian with a width consistent with the total mass of the N-particle system. The resulting

[1] Since the number of terms in the Slater determinant scales as the factorial of the particle number, explicitly calculating all higher-order correlations is a very demanding task already for a few non-interacting particles.

density distributions of the relative momenta for $N = 3$ and $N = 6$ are shown in Fig. 6.2 (a) and (c). The distributions are azimuthally symmetric as expected for the round trap. There are no correlation visible between the atoms, as theses images show the single-particle density of the relative momenta.

- We reveal the underlying correlations between the particles by using the predicted symmetries of the $N = 3$ and $N = 6$ atom Pauli crystals, which are 3- and 5-fold, respectively [160]. The $N = 6$ Pauli crystal consist of one central atom surrounded by a ring of 5 atoms. Thus, for $N = 6$ we ignore the atom with the smallest relative momentum for the determination of the symmetry axis. The known symmetry allows us to rotate the atom pattern of each image onto a chosen target symmetry axis. The rotation angle is determined as follows (see Fig. 6.1): We sort the particles in the image according to their angle ϕ_j in polar coordinates in ascending order. The average rotation angle is determined as

$$\varphi_{\mathrm{rot}} = -\frac{1}{L}\sum_{j=1}^{L}\left(\varphi_j - \frac{2\pi}{L}(j-1)\right) = -\frac{1}{L}\sum_{j=1}^{L}(\Delta\varphi_j)\,. \tag{6.1}$$

  Here L denotes the symmetry of the crystal and j is the index of the j^{th} atom. We rotate the atom positions in this image by φ_{rot} modulo $2\pi/L$. This chancels the mean angular deviation of the atoms from the chosen symmetry configuration.

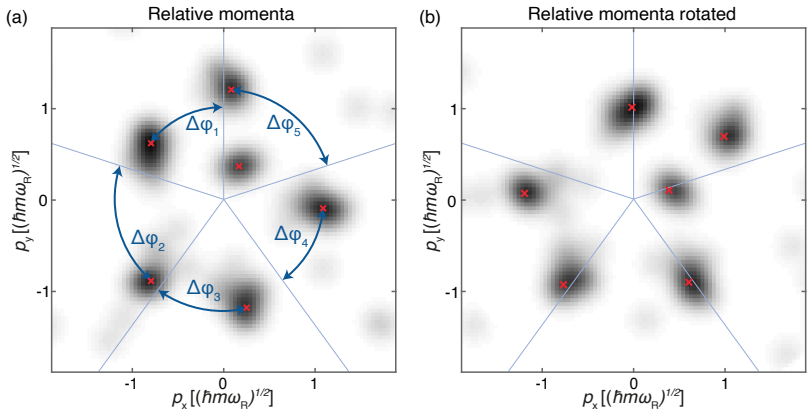

Figure 6.1.: **Processing of single atom resolved images.** (a) Relative momentum of $N = 6$ atoms (red) in a single experimental realization. The symmetry axes of the Pauli crystal are obtained from Ref. [160] and drawn in light blue. The angular deviation of an atom from its respective symmetry axis $\Delta\varphi_j$ is drawn in dark blue. (b) Rotating the image by the average angular deviation, aligns each image to the same fixed symmetry axis.

The analysis presented above gives rise to the distributions shown in Fig. 6.2 (b) and (d) for $N = 3$ and $N = 6$ respectively. In these configuration probability densities we observe the emergence of structure and higher-order density correlations due to quantum statistics. The detected correlations are in momentum space. However, for a harmonic oscillator, the wavefunction in real and momentum space have the same shape and the expansion in the SWT corresponds to a simple magnification of the in situ wavefunction by a factor $\omega_r/\omega_{\mathrm{tof}} \approx 47$.

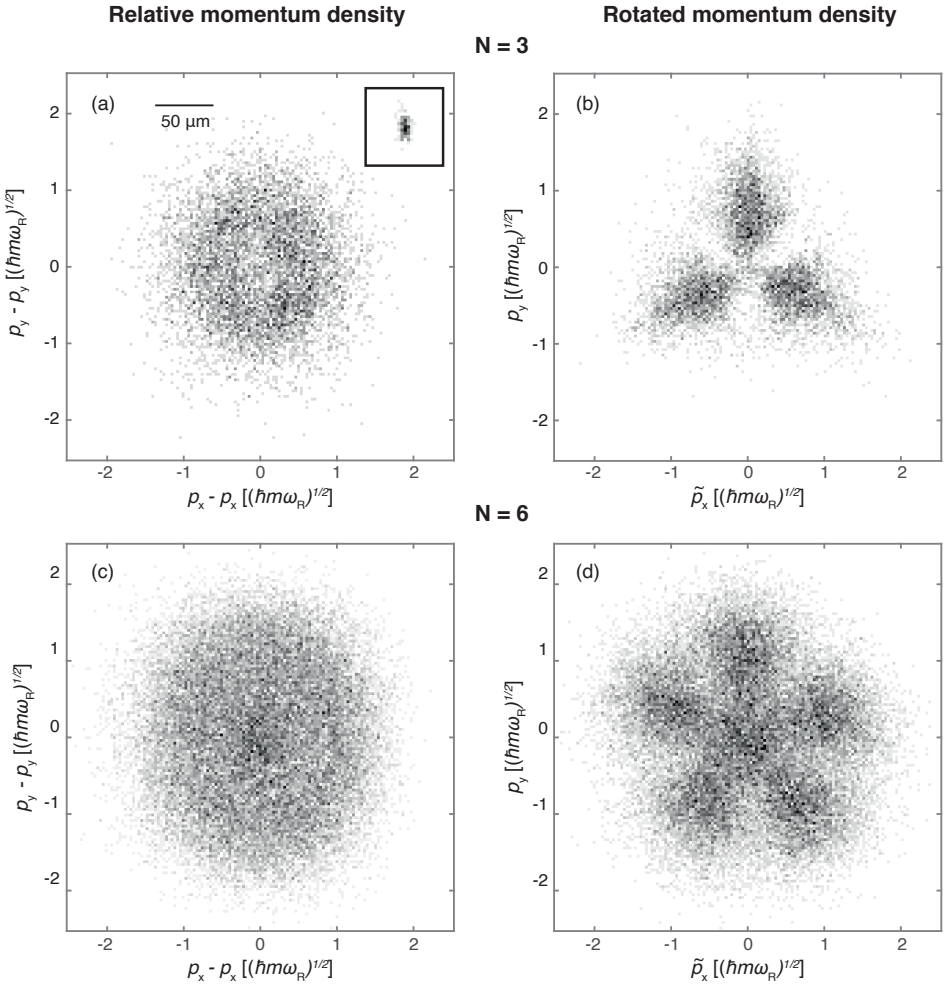

Figure 6.2.: **Pauli crystal measurements.** Relative momentum density for $N = 3$ (a) and $N = 6$ (c) atoms. These images correspond to the single particle momentum density after removing the center of mass momentum. The inset shows a histogram of the detected positions for a single atom that is repeatedly initialized at well-defined position. Rotating the atom distribution in each individual measurement to a chosen symmetry axis results in the configuration probability densities shown in (b) and (d). Here, correlations between all particles are visible. The data for $N = 3$ and $N = 6$ correspond to 2452 and 5373 single images, respectively. Figure adapted from Ref. [151].

6.2. Melting the Crystal

Next, we investigate the $N = 6$ Pauli crystal in more detail and study the decay of correlations, when heating the system. To this end, we modulate the depth of the radial confinement for 50 ms at a frequency of $f_{\mathrm{ex}} = 1965\,\mathrm{Hz}$, which corresponds to twice the trap frequency. The resulting configuration probability densities for different modulation amplitudes are shown in Fig. 6.3, where we observe a decay of the correlation pattern for larger modulation amplitudes.

The heating for each modulation amplitude is quantified by the average energy of the sample, which is extracted from the average momentum distribution. For the lowest achievable temperature, we obtain an energy of $E = (13.1 \pm 0.6)\,\hbar\omega_r$, which is below the harmonic oscillator ground state energy of $E = 14\,\hbar\omega_r$ for $N = 6$ particles. The error is given by the uncertainty of the determination of the trap frequency of the SWT, used for the time of flight expansion. Since the trap frequency is the same for all measurements, this results in a systematic shift of the measured energies. A further potential systematic shift of the measured energy is given by the not precisely known magnification of our imaging system (which we calculated from the ratio of focal lengths). Since the energy depends quadratically on the magnification, this can easily result in systematic shifts of the energy on the order of 10 %. Note that both the trap frequency [83] and the magnification [161] could in principle be determined with a much higher accuracy and precision in a later measurement, if required. Nevertheless, we can still compare the relative change in energy to characterize the excitations of the system.

To investigate the decay of correlations in more detail, we fit the angle dependence of the density at twice the harmonic oscillator momentum with a sine function (Fig. 6.3 (b)). We extract the visibility $V = (\max - \min)/(\max + \min)$ of the fitted sine as a function of the mean energy. The visibility decreases linearly with a slope $\frac{\mathrm{d}V}{\mathrm{d}E} = (-0.054 \pm 0.010)/\hbar\omega_r$. This error does not include any systematic effects and is given by the uncertainty of the fit. Note that this is a heuristic choice for the fitting functions, as there is neither an analytic prediction for the exact angular dependence of the atom density nor for the temperature dependence of the contrast.

The loss of contrast when heating the system confirms that the pattern arises from correlations in the quantum state of the system and is not caused by the imaging or the analysis, which are both independent of the energy.

Remarkably, the modulation of the system is done at zero interaction and naively one would expect that we drive the system coherently. Nevertheless, we see a linear loss in contrast of the pattern with the mean energy of the system. This

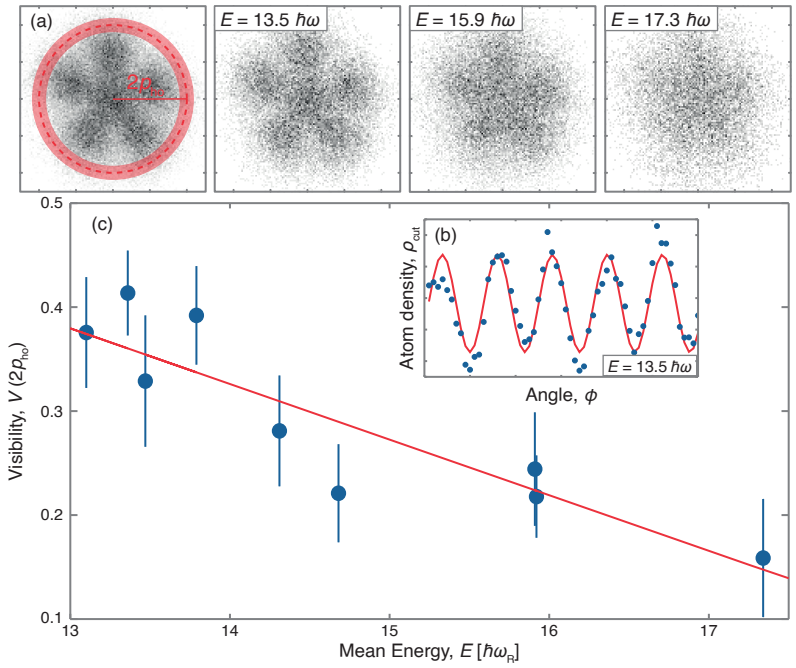

Figure 6.3.: **Melting the Pauli Crystal.** (a) Configuration probability density for $N = 6$ atoms for different mean energies. (b) We fit the density at two times the harmonic oscillator momentum to extract the visibility of the pattern. (c) The visibility decreases with increasing mean energy. For the higher energy data, we take approximately 3000 images for each modulation amplitude. Figure adapted from Ref. [151].

can be understood by considering the large number of many-body states and the dense spectrum at twice the trap frequency. There are 54264 different many-body states for $N = 6$ particles in the lowest 6 shells, i.e. when considering single particle states up to $2\,E_F$. This results in a coupling to a large number of states, when modulating the system and a loss of visibility due to the averaging over a large number of different correlation patterns (when considering small fluctuations between the different experimental realizations). For the future, it might be interesting to investigate this loss of coherence in more detail. This might allow us to study how thermalization emerges in mesoscopic isolated quantum systems [162], when turning on interactions. This is especially exciting as in this system we have access to both an isolated pair excitation mode, that can be driven coherently and a dense spectrum of states above twice the trap frequency, where an incoherent rate equation picture might be the better description.

In conclusion, we have demonstrated single-particle and momentum resolved imaging of up to 6 atoms released from a quasi-2D harmonic trap. The access to all momenta in a single experimental realization, allowed us to detect higher order

correlations between the non-interacting fermions. These correlations originate from the anti-symmetrization of the many-body wavefunction and decay, when heating the sample.

These measurements of Pauli Crystals constitute the first observation of beyond second-order density correlations arising from fermionic quantum statistics in bulk systems. Note that these geometric structures and density correlations due to the Pauli principle are local, as opposed to true (interaction driven) crystalline phases, where the system has true long-range order. This is due to the short range nature of the Pauli exclusion principle, which results in correlations on distances comparable to the inverse of the Fermi momentum. For our small system these correlations are, nevertheless, strong enough to create a global structure.

7. Conclusion and Outlook

In this thesis we have presented our recent experiments studying the emergence of collective behavior in mesoscopic 2D Fermi systems.
The first experimental achievement and the basis for all other experiments is the deterministic preparation of mesoscopic low-entropy samples in a quasi-2D geometry. When scanning the potential depth we observe the enhanced stability of closed-shell configurations consisting of 2, 6 and 12 fermions in the ground state of the trap.
These deterministically created closed-shell configurations of the 2D harmonic oscillator are the starting point for our observation of the few-body precursor of a quantum phase transition. The phase transition arises from the competition of the gapped single-particle spectrum with the attractive interactions and is revealed by a measurement of the excitation spectrum. The full counting statistics of the excitation spectrum reveals pair excitations, whose energy has a non-monotonous interaction dependence. These modes are the few-body precursors of the amplitude mode of the order parameter for the normal to superfluid quantum phase transition. Already the smallest non-trivial closed-shell configuration of 6 atoms shows qualitatively the same spectrum as in the many-body limit. The comparison of the spectra for 6 and 12 atoms allows us to observe first signatures of the approach towards the many-body limit, which is indicated by the deepening and shifting of the minimal excitation gap for 12 atoms.
In a second set of experiments we go beyond counting the number of atoms in the trap and measure the momentum distribution of the sample with single-atom resolution. Here, we investigate the momentum distribution of closed-shell configurations of non-interacting particles. The single-particle sensitivity of the imaging allows us to measure the momenta of all particles in a single shot and thereby makes it possible to sample the many-body wavefunction and to obtain all order density correlation functions. We detect strong correlations between identical fermions, that arise from the anti-symmetrization of the wavefunction. This constitutes the first observation of higher-order density correlations in non-interacting fermionic bulk systems. Furthermore, the application of our imaging scheme to a non-interacting system serves as an important benchmark for the

method, before proceeding to interacting systems, where no theory prediction is available.

As the next step, we plan to apply our capability to measure the momentum distribution of the interacting system. Measuring the momentum distribution of both spin states will allow us to probe the emergence of pair correlations in the system. This requires to measure the *in situ* momentum distribution, which can be done by quenching the interactions at the release of the sample and a subsequent ballistic expansion. For this purpose, we are currently implementing a microwave setup into the experiment, which will allow us to drive state $|3\rangle$ to $|4\rangle$, which is weakly interacting with state $|1\rangle$.
This will enable us to study the in situ momentum correlations of the system across the few-body precursor of the phase transition. We expect to observe the emergence of pair correlations between opposite spins for increasing interactions. At the same time, a deformation of the Pauli-crystal structure in the correlations of identical particles indicating the deformation of the miniature Fermi sea is expected. Additionally, our coherent control over the Higgs mode enables us to study momentum correlations in the excited state, where we expect larger pair correlations in the excited than in the ground state for weak attraction.
In contrast to this time of flight protocol, we can also choose to keep the interactions on during the expansion, such that the gas remains collisional. In this case, one expects an interaction-induced redistribution of the momenta during the expansion. This opens up the possibility to study the validity of hydrodynamics in systems consisting of only a few particles. This offers a connection to the physics of heavy-ion collisions, where at the initial stage after the collision the quark-gluon plasma expands hydrodynamical until the so-called freeze out after which the particles propagate ballistically to the detector where they are measured.[1]
Besides these momentum-space measurements we can also study the properties of the system in more detail in situ. The measurements of the excitation spectrum show that there are two qualitatively different regions in the spectrum. The isolated pair excitation mode, which can be driven coherently and the dense spectrum above twice the trap frequency. For the Pauli-crystal measurements we have observed a loss of coherence even when we drive the non-interacting system in this frequency range with a dense many-body spectrum. This might open up ways to explore thermalization in strongly interacting isolated quantum systems [162].

[1] See Ref. [163] for a review comparing hydrodynamics in ultracold atoms and quark-gluon plasmas.

In addition to these measurements, which should be readily possible in the existing setup, there are also other exciting avenues: By trading control for system size it might be possible to scale the system to approximately one-hundred particles at low entropy. This separates the scales of the harmonic oscillator spacing and the Fermi energy. The goal is to observe the emergence of Cooper pairs directly by correlations in momentum space [164]. Then proceeding to the strongly interacting regime, where we have observed signatures of many-body paring in the rf response [111], it might be possible to observe higher-order correlations in the momentum distribution and gain further insight in this strongly correlated system.

Another possibility is to make use of the flexibility of the SLM and study different trapping geometries. By rotating the trap we could create gauge fields to study quantum hall physics [126]. Furthermore, the creation of an array of coupled microtraps and studying mesoscopic Fermi-Hubbard systems is an exciting prospect. Our first experiments in this direction are summarized in Ref. [130]. Here, the first goal would be the observation of Nagaoka magnetism in a plaquette [165], i.e. observing the change of the ground state from anti-ferromagnetic to ferromagnetic upon increasing the repulsion in the hole-doped system.

Bibliography

[1] P. W. Anderson. More Is Different. *Science* **177**.4047 (1972), pp. 393–396.

[2] R. B. Laughlin and D. Pines. The Theory of Everything. *Proceedings of the National Academy of Sciences* **97**.1 (2000), pp. 28–31.

[3] J. Goldstone, A. Salam, and S. Weinberg. Broken Symmetries. *Physical Review* **127**.3 (1962), pp. 965–970.

[4] A. Altland and B. Simons. *Condensed Matter Field Theory*. Cambridge University Press, 2010.

[5] S. Sachdev. *Quantum Phase Transitions*. Cambridge University Press, 2011.

[6] S. Grebenev, J. P. Toennies, and A. F. Vilesov. Superfluidity within a small helium-4 cluster: The microscopic Andronikashvili experiment. *Science* **279**.5359 (1998), pp. 2083–2086.

[7] M. Goldhaber and E. Teller. On Nuclear Dipole Vibrations. *Physical Review* **74**.9 (1948), pp. 1046–1049.

[8] A. B. Migdal. Superfluidity and the moments of inertia of nuclei. *Nuclear Physics* **13**.5 (1959), pp. 655–674.

[9] S. M. Reimann and M. Manninen. Electronic structure of quantum dots. *Reviews of Modern Physics* **74**.4 (2002), pp. 1283–1342.

[10] A. W. Castleman and S. N. Khanna. Clusters, Superatoms, and Building Blocks of New Materials. *The Journal of Physical Chemistry C* **113**.7 (2009), pp. 2664–2675.

[11] F. Serwane, G. Zürn, T. Lompe, T. B. Ottenstein, A. N. Wenz, and S. Jochim. Deterministic preparation of a tunable few-fermion system. *Science* **332**.6027 (2011), pp. 336–338.

[12] A. N. Wenz, G. Zürn, S. Murmann, I. Brouzos, T. Lompe, and S. Jochim. From few to many: Observing the formation of a Fermi sea one atom at a time. *Science* **342**.6157 (2013), pp. 457–460.

[13] I. Bloch, J. Dalibard, and W. Zwerger. Many-body physics with ultracold gases. *Reviews of Modern Physics* **80**.3 (2008), pp. 885–964.

[14] S. Murmann, A. Bergschneider, V. M. Klinkhamer, G. Zürn, T. Lompe, and S. Jochim. Two Fermions in a Double Well: Exploring a Fundamental Building Block of the Hubbard Model. *Physical Review Letters* **114**.8 (2015).

[15] U. Schneider, L. Hackermuller, S. Will, T. Best, I. Bloch, T. A. Costi, R. W. Helmes, D. Rasch, and A. Rosch. Metallic and Insulating Phases of Repulsively Interacting Fermions in a 3D Optical Lattice. *Science* **322**.5907 (2008), pp. 1520–1525.

[16] R. Jördens, N. Strohmaier, K. Günter, H. Moritz, and T. Esslinger. A Mott insulator of fermionic atoms in an optical lattice. *Nature* **455**.7210 (2008), pp. 204–207.

[17] V. Berezinsky. Destruction of long-range order in one-dimensional and two-dimensional systems possessing a continuous symmetry group. II. Quantum systems. *Zh. Eksp. Teor. Fiz.* **61** (1972), p. 610.

[18] J. M. Kosterlitz and D. J. Thouless. Ordering, metastability and phase transitions in two-dimensional systems. *Journal of Physics C: Solid State Physics* **6**.7 (1973), pp. 1181–1203.

[19] A. J. Leggett. "Diatomic molecules and cooper pairs". In: *Modern Trends in the Theory of Condensed Matter*. Springer Berlin Heidelberg, 1980, pp. 13–27.

[20] M. Bartenstein, A. Altmeyer, S. Riedl, S. Jochim, C. Chin, J. H. Denschlag, and R. Grimm. Crossover from a Molecular Bose-Einstein Condensate to a Degenerate Fermi Gas. *Physical Review Letters* **92**.12 (2004).

[21] M. W. Zwierlein, J. R. Abo-Shaeer, A. Schirotzek, C. H. Schunck, and W. Ketterle. Vortices and superfluidity in a strongly interacting Fermi gas. *Nature* **435**.7045 (2005), pp. 1047–1051.

[22] W. Ketterle and M. W. Zwierlein. Making, probing and understanding ultracold Fermi gases. *Rivista del Nuovo Cimento* (2008).

[23] M. M. Parish. "The BCS–BEC Crossover". In: *Cold Atoms*. IMPERIAL COLLEGE PRESS, 2014, pp. 179–197.

[24] G. C. Strinati, P. Pieri, G. Röpke, P. Schuck, and M. Urban. The BCS–BEC crossover: From ultra-cold Fermi gases to nuclear systems. *Physics Reports* **738** (2018), pp. 1–76.

[25] W. Zwerger. “Strongly Interacting Fermi Gases”. In: *Proceedings of the International School of Physics 'Enrico Fermi'*. Vol. 191 "Quantum Matter at Ultralow Temperatures". 2016, pp. 63–142.

[26] G. M. Bruun and B. R. Mottelson. Low Energy Collective Modes of a Superfluid Trapped Atomic Fermi Gas. *Physical Review Letters* **87**.27 (2001).

[27] G. M. Bruun. Long-lived Higgs mode in a two-dimensional confined Fermi system. *Physical Review A - Atomic, Molecular, and Optical Physics* **90**.2 (2014).

[28] J. Bjerlin, S. M. Reimann, and G. M. Bruun. Few-body precursor of the higgs mode in a fermi gas. *Physical Review Letters* **116**.15 (2016).

[29] L. M. L. L. Landau. *Quantum Mechanics Non-Relativistic Theory*. Elsevier LTD, Oxford, 1981.

[30] L. de Broglie. XXXV. A tentative theory of light quanta. *The London, Edinburgh, and Dublin Philosophical Magazine and Journal of Science* **47**.278 (1924), pp. 446–458.

[31] M. E. Peskin and D. V. Schroeder. *An Introduction To Quantum Field Theory*. Taylor & Francis Ltd, 2019.

[32] W. Pauli. Über den Zusammenhang des Abschlusses der Elektronengruppen im Atom mit der Komplexstruktur der Spektren. *Zeitschrift für Physik* **31**.1 (1925), pp. 765–783.

[33] F. Schwabl. *Statistische Mechanik*. Springer-Verlag GmbH, 2006.

[34] C. Pethick and H. Smith. *Bose-Einstein Condensation in Dilute Gases*. Cambridge University Press, 2001.

[35] J. J. Sakurai. *Modern Quantum Mechanics*. Reading, Mass.: Addison-Wesley Pub. Co, 1994.

[36] J. Dalibard. “Collisional dynamics of ultra-cold atomic gases”. In: *Proceedings of the International School of Physics-Enrico Fermi*. Vol. 321. 1999.

[37] C. Chin, R. Grimm, P. Julienne, and E. Tiesinga. Feshbach resonances in ultracold gases. *Reviews of Modern Physics* **82**.2 (2010), p. 1225.

[38] J. Levinsen and M. M. Parish. “Strongly interacting two-dimensional Fermi gases”. In: *Annual Review of Cold Atoms and Molecules*. World Scientific, 2015, pp. 1–75.

[39] G. Zürn, T. Lompe, A. N. Wenz, S. Jochim, P. S. Julienne, and J. M. Hutson. Precise characterization of Li6 Feshbach resonances using trap-sideband-resolved RF spectroscopy of weakly bound molecules. *Physical Review Letters* **110**.13 (2013).

[40] M. Lu, N. Q. Burdick, and B. L. Lev. Quantum Degenerate Dipolar Fermi Gas. *Physical Review Letters* **108**.21 (2012).

[41] P. G Hansen and B Jonson. The Neutron Halo of Extremely Neutron-Rich Nuclei. *Europhysics Letters (EPL)* **4**.4 (1987), pp. 409–414.

[42] P. Bloom. Two-dimensional Fermi gas. *Physical Review B* **12**.1 (1975), pp. 125–129.

[43] B. Fröhlich, M. Feld, E. Vogt, M. Koschorreck, M. Köhl, C. Berthod, and T. Giamarchi. Two-Dimensional Fermi Liquid with Attractive Interactions. *Physical Review Letters* **109**.13 (2012).

[44] D. S. Petrov and G. V. Shlyapnikov. Interatomic collisions in a tightly confined Bose gas. *Physical Review A* **64**.1 (2001).

[45] T. Busch, B.-G. Englert, K. Rzażewski, and M. Wilkens. Two cold atoms in a harmonic trap. *Foundations of Physics* **28**.4 (1998), pp. 549–559.

[46] Z. Idziaszek and T. Calarco. Analytical solutions for the dynamics of two trapped interacting ultracold atoms. *Physical Review A* **74**.2 (2006), p. 022712.

[47] Y. Chen, D.-W. Xiao, R. Zhang, and P. Zhang. Analytical solution for the spectrum of two ultracold atoms in a completely anisotropic confinement. *arXiv:2002.02168v4* (2020).

[48] L. D. Landau. On the theory of phase transitions. *Ukr. J. Phys.* **11** (1937), pp. 19–32.

[49] V. L. Ginzburg and L. D. Landau. On the Theory of superconductivity. *Zh. Eksp. Teor. Fiz* (1950).

[50] J. Bardeen, L. N. Cooper, and J. R. Schrieffer. Theory of Superconductivity. *Physical Review* **108**.5 (1957), pp. 1175–1204.

[51] D. Pekker and C. Varma. Amplitude/Higgs Modes in Condensed Matter Physics. *Annual Review of Condensed Matter Physics* **6**.1 (2015), pp. 269–297.

[52] K. G. Wilson. The renormalization group: Critical phenomena and the Kondo problem. *Reviews of Modern Physics* **47**.4 (1975), pp. 773–840.

[53] J. Goldstone. Field theories with Superconductor solutions. *Il Nuovo Cimento* **19**.1 (1961), pp. 154–164.

[54] P. Higgs. Broken symmetries, massless particles and gauge fields. *Physics Letters* **12**.2 (1964), pp. 132–133.

[55] R. Sooryakumar and M. V. Klein. Raman scattering by superconducting-gap excitations and their coupling to charge-density waves. *Physical Review Letters* **45**.8 (1980), pp. 660–662.

[56] C. Rüegg, B. Normand, M. Matsumoto, A. Furrer, D. F. McMorrow, K. W. Krämer, H. U. Güdel, S. N. Gvasaliya, H. Mutka, and M. Boehm. Quantum magnets under pressure: Controlling elementary excitations in TlCuCl3. *Physical Review Letters* **100**.20 (2008).

[57] U. Bissbort, S. Götze, Y. Li, J. Heinze, J. S. Krauser, M. Weinberg, C. Becker, K. Sengstock, and W. Hofstetter. Detecting the amplitude mode of strongly interacting lattice bosons by Bragg scattering. *Physical Review Letters* **106**.20 (2011).

[58] M. Endres, T. Fukuhara, D. Pekker, M. Cheneau, P. Schauss, C. Gross, E. Demler, S. Kuhr, and I. Bloch. The 'Higgs' amplitude mode at the two-dimensional superfluid/Mott insulator transition. *Nature* **487**.7408 (2012), pp. 454–458.

[59] R. Matsunaga, Y. I. Hamada, K. Makise, Y. Uzawa, H. Terai, Z. Wang, and R. Shimano. Higgs Amplitude Mode in the BCS SuperconductorsNb1-xTixNInduced by Terahertz Pulse Excitation. *Physical Review Letters* **111**.5 (2013).

[60] J. Léonard, A. Morales, P. Zupancic, T. Donner, and T. Esslinger. Monitoring and manipulating Higgs and Goldstone modes in a supersolid quantum gas. *Science* **358**.6369 (2017), pp. 1415–1418.

[61] K. Katsumi, N. Tsuji, Y. I. Hamada, R. Matsunaga, J. Schneeloch, R. D. Zhong, G. D. Gu, H. Aoki, Y. Gallais, and R. Shimano. Higgs Mode in the d-Wave Superconductor $Bi_2Sr_2CaCu_2O_{8+x}$ Driven by an Intense Terahertz Pulse. *Physical Review Letters* **120**.11 (2018).

[62] A. Behrle, T. Harrison, J. Kombe, K. Gao, M. Link, J. S. Bernier, C. Kollath, and M. Köhl. Higgs mode in a strongly interacting fermionic superfluid. *Nature Physics* **14**.8 (2018), pp. 781–785.

[63] S. Jochim, M. Bartenstein, A. Altmeyer, G. Hendl, C. Chin, J. H. Denschlag, and R. Grimm. Pure Gas of Optically Trapped Molecules Created from Fermionic Atoms. *Physical Review Letters* **91**.24 (2003).

[64] D. Petrov, C. Salomon, and G. V. Shlyapnikov. Weakly bound dimers of fermionic atoms. *Physical review letters* **93**.9 (2004), p. 090404.

[65] S. Jochim, M Bartenstein, A Altmeyer, G Hendl, S Riedl, C Chin, J. H. Denschlag, and R Grimm. Bose-Einstein condensation of molecules. *Science* **302**.5653 (2003), pp. 2101–2103.

[66] M. Greiner, C. A. Regal, and D. S. Jin. Emergence of a molecular Bose–Einstein condensate from a Fermi gas. *Nature* **426**.6966 (2003), pp. 537–540.

[67] M. W. Zwierlein, C. A. Stan, C. H. Schunck, S. M. F. Raupach, S. Gupta, Z. Hadzibabic, and W. Ketterle. Observation of Bose-Einstein condensation of molecules. *Physical Review Letters* **91**.25 (2003), p. 250401.

[68] C. M. Varma. Higgs Boson in Superconductors. *Journal of Low Temperature Physics* **126**.3/4 (2002), pp. 901–909.

[69] P. W. Anderson. Random-Phase Approximation in the Theory of Superconductivity. *Physical Review* **112**.6 (1958), pp. 1900–1916.

[70] P. B. Littlewood and C. M. Varma. Amplitude collective modes in superconductors and their coupling to charge-density waves. *Physical Review B* **26**.9 (1982), pp. 4883–4893.

[71] H. Kurkjian, S. N. Klimin, J. Tempere, and Y. Castin. Pair-Breaking Collective Branch in BCS Superconductors and Superfluid Fermi Gases. *Physical Review Letters* **122**.9 (2019).

[72] S. D. Huber, B. Theiler, E. Altman, and G. Blatter. Amplitude Mode in the Quantum Phase Model. *Physical Review Letters* **100**.5 (2008).

[73] D. Podolsky, A. Auerbach, and D. P. Arovas. Visibility of the amplitude (Higgs) mode in condensed matter. *Physical Review B* **84**.17 (2011).

[74] L. Pollet and N. Prokof'ev. Higgs Mode in a Two-Dimensional Superfluid. *Physical Review Letters* **109**.1 (2012).

[75] T. Cea and L. Benfatto. Nature and Raman signatures of the Higgs amplitude mode in the coexisting superconducting and charge-density-wave state. *Physical Review B* **90**.22 (2014).

[76] T. Cea, C. Castellani, G. Seibold, and L. Benfatto. Nonrelativistic Dynamics of the Amplitude (Higgs) Mode in Superconductors. *Physical Review Letters* **115**.15 (2015).

[77] D. M. Eagles. Possible Pairing without Superconductivity at Low Carrier Concentrations in Bulk and Thin-Film Superconducting Semiconductors. *Physical Review* **186**.2 (1969), pp. 456–463.

[78] R. Haussmann, W. Rantner, S. Cerrito, and W. Zwerger. Thermodynamics of the BCS-BEC crossover. *Physical Review A* **75**.2 (2007).

[79] C. Cao, E. Elliott, J. Joseph, H. Wu, J. Petricka, T. Schafer, and J. E. Thomas. Universal Quantum Viscosity in a Unitary Fermi Gas. *Science* **331**.6013 (2010), pp. 58–61.

[80] L. P. Pitaevskii and A. Rosch. Breathing modes and hidden symmetry of trapped atoms in two dimensions. *Physical Review A* **55**.2 (1997), R853–R856.

[81] S. Moroz. Scale-invariant Fermi gas in a time-dependent harmonic potential. *Physical Review A* **86**.1 (2012).

[82] M. Olshanii, H. Perrin, and V. Lorent. Example of a Quantum Anomaly in the Physics of Ultracold Gases. *Physical Review Letters* **105**.9 (2010).

[83] M. Holten, L. Bayha, A. Klein, P. Murthy, P. Preiss, and S. Jochim. Anomalous Breaking of Scale Invariance in a Two-Dimensional Fermi Gas. *Physical Review Letters* **121**.12 (2018).

[84] T. Peppler, P. Dyke, M. Zamorano, I. Herrera, S. Hoinka, and C. Vale. Quantum Anomaly and 2D-3D Crossover in Strongly Interacting Fermi Gases. *Physical Review Letters* **121**.12 (2018).

[85] N. D. Mermin and H. Wagner. Absence of Ferromagnetism or Antiferromagnetism in One- or Two-Dimensional Isotropic Heisenberg Models. *Physical Review Letters* **17**.22 (1966), pp. 1133–1136.

[86] Z. Hadzibabic and J. Dalibard. "Two-dimensional Bose fluids: An atomic physics perspective". In: *Rivista del Nuovo Cimento*. Vol. 34. 2011, pp. 389–434.

[87] D. R. Nelson and J. M. Kosterlitz. Universal Jump in the Superfluid Density of Two-Dimensional Superfluids. *Physical Review Letters* **39**.19 (1977), pp. 1201–1205.

[88] M. Kohmoto and Y. Takada. Superconductivity from an Insulator. *Journal of the Physical Society of Japan* **59**.5 (1990), pp. 1541–1544.

[89] P. Nozières and F. Pistolesi. From semiconductors to superconductors: a simple model for pseudogaps. *The European Physical Journal B* **10**.4 (1999), pp. 649–662.

[90] G. M. Bruun. Low-Energy Monopole Modes of a Trapped Atomic Fermi Gas. *Physical Review Letters* **89**.26 (2002).

[91] G. M. Bruun and H. Heiselberg. Cooper pairing and single-particle properties of trapped Fermi gases. *Physical Review A* **65**.5 (2002).

[92] H. Heiselberg and B. Mottelson. Shell Structure and Pairing for Interacting Fermions in a Trap. *Physical Review Letters* **88**.19 (2002).

[93] L. Bayha, M. Holten, R. Klemt, K. Subramanian, J. Bjerlin, S. M. Reimann, G. M. Bruun, P. M. Preiss, and S. Jochim. Observing the emergence of a quantum phase transition – shell by shell. *arXiv:2004.14761* (2020).

[94] M. Ries. A magneto-optical trap for the preparation of a three-component Fermi gas in an optical lattice. Diploma thesis. Heidelberg University, 2010.

[95] A. Bohn. Towards an ultracold three-component Fermi Gas in a two-dimensional optical lattice. Diploma thesis. Heidelberg University, 2012.

[96] M. Neidig. A realization of a two-dimensional Fermi gas in a standing wave trap. Masters's thesis. Heidelberg University, 2013.

[97] A. Wenz. From Few to Many: Ultracold Atoms in Reduced Dimensions. Dissertation. Heidelberg University, 2013.

[98] M. Ries. A Two-Dimensional Fermi Gas in the BEC-BCS Crossover. Dissertation. Heidelberg University, 2014.

[99] M. Gehm. Preparation of an optically-trapped degenerate Fermi gas of 6Li: Finding the route to degeneracy. PhD thesis. Duke University, 2003.

[100] P. Simon. Apparatus for the preparation of ultracold Fermi gases. Diploma thesis. Heidelberg University, 2010.

[101] C. J. Foot. *Atomic physics*. Oxford University Press, 2004.

[102] R. Grimm, M. Weidemüller, and Y. B. Ovchinnikov. "Optical Dipole Traps for Neutral Atoms". In: *Advances In Atomic, Molecular, and Optical Physics*. Elsevier, 2000, pp. 95–170.

[103] K. Hueck, N. Luick, L. Sobirey, J. Siegl, T. Lompe, and H. Moritz. Two-Dimensional Homogeneous Fermi Gases. *Physical Review Letters* **120**.6 (2018).

[104] M. Neidig. Many-Body Pairing in a Two-Dimensional Fermi Gas. PhD thesis. Heidelberg University, 2017.

[105] S. Tung, G. Lamporesi, D. Lobser, L. Xia, and E. A. Cornell. Observation of the Presuperfluid Regime in a Two-Dimensional Bose Gas. *Physical Review Letters* **105**.23 (2010).

[106] P. A. Murthy, D. Kedar, T. Lompe, M. Neidig, M. G. Ries, A. N. Wenz, G. Zürn, and S. Jochim. Matter-wave Fourier optics with a strongly interacting two-dimensional Fermi gas. *Physical Review A* **90** (2014).

[107] M. W. Zwierlein, C. A. Stan, C. H. Schunck, S. M. F. Raupach, A. J. Kerman, and W. Ketterle. Condensation of Pairs of Fermionic Atoms near a Feshbach Resonance. *Physical Review Letters* **92**.12 (2004).

[108] P. A. Murthy. Emergent phenomena in two-dimensional Fermi systems. PhD thesis. Heidelberg University, 2018.

[109] M. Ries, A. Wenz, G. Zürn, L. Bayha, I. Boettcher, D. Kedar, P. Murthy, M. Neidig, T. Lompe, and S. Jochim. Observation of Pair Condensation in the Quasi-2D BEC-BCS Crossover. *Physical Review Letters* **114**.23 (2015), p. 230401.

[110] P. Murthy, I Boettcher, L Bayha, M Holzmann, D Kedar, M Neidig, M. Ries, A. Wenz, G Zürn, and S Jochim. Observation of the Berezinskii-Kosterlitz-Thouless Phase Transition in an Ultracold Fermi Gas. *Physical Review Letters* **115**.1 (2015).

[111] P. A. Murthy, M. Neidig, R. Klemt, L. Bayha, I. Boettcher, T. Enss, M. Holten, G. Zürn, P. M. Preiss, and S. Jochim. High-temperature pairing in a strongly interacting two-dimensional Fermi gas. *Science* **359**.6374 (2018), pp. 452–455.

[112] N. Prokof'ev and B. Svistunov. Two-dimensional weakly interacting Bose gas in the fluctuation region. *Physical Review A* **66**.4 (2002).

[113] D. S. Petrov, M. A. Baranov, and G. V. Shlyapnikov. Superfluid transition in quasi-two-dimensional Fermi gases. *Physical Review A* **67**.3 (2003).

[114] I. Boettcher and M. Holzmann. Quasi-long-range order in trapped two-dimensional Bose gases. *Physical Review A* **94**.1 (2016).

[115] M. Bauer, M. M. Parish, and T. Enss. Universal Equation of State and Pseudogap in the Two-Dimensional Fermi Gas. *Physical Review Letters* **112**.13 (2014).

[116] A. Schirotzek, Y. il Shin, C. H. Schunck, and W. Ketterle. Determination of the Superfluid Gap in Atomic Fermi Gases by Quasiparticle Spectroscopy. *Physical Review Letters* **101**.14 (2008).

[117] G. Gauthier, I. Lenton, N. M. Parry, M. Baker, M. J. Davis, H. Rubinsztein-Dunlop, and T. W. Neely. Direct imaging of a digital-micromirror device for configurable microscopic optical potentials. *Optica* **3**.10 (2016), p. 1136.

[118] P. Zupancic, P. M. Preiss, R. Ma, A. Lukin, M. E. Tai, M. Rispoli, R. Islam, and M. Greiner. Ultra-precise holographic beam shaping for microscopic quantum control. *Optics Express* **24**.13 (2016), p. 13881.

[119] S. Bergamini, B. Darquié, M. Jones, L. Jacubowiez, A. Browaeys, and P. Grangier. Holographic generation of microtrap arrays for single atoms by use of a programmable phase modulator. *Journal of the Optical Society of America B* **21**.11 (2004), p. 1889.

[120] M. J. Stephen and J. P. Straley. Physics of liquid crystals. *Reviews of Modern Physics* **46**.4 (1974), pp. 617–704.

[121] K. Hueck, A. Mazurenko, N. Luick, T. Lompe, and H. Moritz. Note: Suppression of kHz-frequency switching noise in digital micro-mirror devices. *Review of Scientific Instruments* **88**.1 (2017), p. 016103.

[122] E. G. Steward. *Fourier Optics an Introduction*. Dover Publications Inc., 2004. 272 pp.

[123] R. R. V. Bijnen. Quantum engineering with ultracold atoms. en. PhD thesis. Technische Universiteit Eindhoven, 2013.

[124] A. L. Gaunt and Z. Hadzibabic. Robust Digital Holography For Ultracold Atom Trapping. *Scientific Reports* **2**.1 (2012).

[125] M. Holten. Hamiltonian Engineering in Ultracold Atom Experiments using a Spatial Light Modulator. Bachelor's thesis. Heidelberg University, 2014.

[126] L. Palm. Exploring fractional quantum hall physics using ultracold fermions in rotating traps. Masters's thesis. Heidelebrg University, 2018.

[127] M. Kress. *Digital Diffractive Optics*. John Wiley & Sons, 2000. 400 pp.

[128] B. Classen. Intensity Stability of Potentials created with an Analog Spatial Light Modulator. Bachelor's thesis. Heidelberg University, 2016.

[129] M. Holten. Collective Modes and Turbulence in Two-Dimensinal Fermi Gases. Masters's thesis. Heidelberg University, 2017.

[130] A. Klein. Versatile Platform for Cold Atom Physics with ^{6}Li based on Holographic Potentials. Masters's thesis. Heidelberg University, 2018.

[131] F. Serwane. Deterministic preparation of a tunable few-fermion system. PhD thesis. Heidelberg University, 2011.

[132] A. Bergschneider. Ultracold few-fermion systems in multiwell potentials. Masters's thesis. Heidelberg University, 2013.

[133] Z. Hu and H. J. Kimble. Observation of a single atom in a magneto-optical trap. *Optics Letters* **19**.22 (1994), p. 1888.

[134] D. B. Hume, I. Stroescu, M. Joos, W. Muessel, H. Strobel, and M. K. Oberthaler. Accurate Atom Counting in Mesoscopic Ensembles. *Physical Review Letters* **111**.25 (2013).

[135] A. Bergschneider, V. M. Klinkhamer, J. H. Becher, R. Klemt, G. Zürn, P. M. Preiss, and S. Jochim. Spin-resolved single-atom imaging of Li 6 in free space. *Physical Review A* **97**.6 (2018).

[136] A. Bergschneider, V. M. Klinkhamer, J. H. Becher, R. Klemt, L. Palm, G. Zürn, S. Jochim, and P. M. Preiss. Experimental characterization of two-particle entanglement through position and momentum correlations. *Nature Physics* **15**.7 (2019), pp. 640–644.

[137] P. M. Preiss, J. H. Becher, R. Klemt, V. Klinkhamer, A. Bergschneider, N. Defenu, and S. Jochim. High-Contrast Interference of Ultracold Fermions. *Physical Review Letters* **122**.14 (2019).

[138] J. H. Becher. Towards Spin and Site-Resolved, Single-Atom Imaging of ^{6}Li Atoms in a Multiwell Potential. Masters's thesis. Heidelberg University, 2016.

[139] A. Bergschneider. Strong correlations in few-fermion systems. PhD thesis. Heidelberg University, 2017.

[140] V. Klinkhamer. Few-Fermion Systems Under a Matterwave Microscope. PhD thesis. Heidelberg University, 2017.

[141] C. S. Chiu, G. Ji, A. Mazurenko, D. Greif, and M. Greiner. Quantum State Engineering of a Hubbard System with Ultracold Fermions. *Physical Review Letters* **120**.24 (2018).

[142] C. Weitenberg, S. Kuhr, K. Mølmer, and J. F. Sherson. Quantum computation architecture using optical tweezers. *Physical Review A* **84**.3 (2011).

[143] V. N. Mahajan and G. ming Dai. Orthonormal polynomials in wavefront analysis: analytical solution. *Journal of the Optical Society of America A* **24**.9 (2007), p. 2994.

[144] R. M. W. van Bijnen, C Ravensbergen, D. J. Bakker, G. J. Dijk, S. J. J. M. F. Kokkelmans, and E. J. D. Vredenbregt. Patterned Rydberg excitation and ionization with a spatial light modulator. *New Journal of Physics* **17**.2 (2015), p. 023045.

[145] G. Zürn, F. Serwane, T. Lompe, A. N. Wenz, M. G. Ries, J. E. Bohn, and S. Jochim. Fermionization of Two Distinguishable Fermions. *Physical Review Letters* **108**.7 (2012).

[146] G. Zürn. Few-fermion systems in one dimension. PhD thesis. Heidelberg University, 2012.

[147] G. Zürn, A. N. Wenz, S. Murmann, A. Bergschneider, T. Lompe, and S. Jochim. Pairing in Few-Fermion Systems with Attractive Interactions. *Physical Review Letters* **111**.17 (2013).

[148] CVI Melles-griot. *Gaussian Beam Optics*. URL: https://www.cvimellesgriot.com/Products/Documents/TechnicalGuide/Gaussian-Beam-Optics.pdf.

[149] M. Rontani, J. R. Armstrong, Y. Yu, S. Åberg, and S. M. Reimann. Cold fermionic atoms in two-dimensional traps: Pairing versus Hund's rule. *Physical Review Letters* **102**.6 (2009).

[150] S. Murmann, F. Deuretzbacher, G. Zürn, J. Bjerlin, S. Reimann, L. Santos, T. Lompe, and S. Jochim. Antiferromagnetic Heisenberg Spin Chain of a Few Cold Atoms in a One-Dimensional Trap. *Physical Review Letters* **115**.21 (2015).

[151] M. Holten, L. Bayha, K. Subramanian, C. Heintze, P. M. Preiss, and S. Jochim. Observation of Pauli Crystals. *arXiv:2005.03929* (2020).

[152] I. Shapir, A. Hamo, S. Pecker, C. P. Moca, Ö. Legeza, G. Zarand, and S. Ilani. Imaging the electronic Wigner crystal in one dimension. *Science* **364**.6443 (2019), pp. 870–875.

[153] D. J. Wineland, J. C. Bergquist, W. M. Itano, J. J. Bollinger, and C. H. Manney. Atomic-Ion Coulomb Clusters in an Ion Trap. *Physical Review Letters* **59**.26 (1987), pp. 2935–2938.

[154] F. Diedrich, E. Peik, J. M. Chen, W. Quint, and H. Walther. Observation of a Phase Transition of Stored Laser-Cooled Ions. *Physical Review Letters* **59**.26 (1987), pp. 2931–2934.

[155] P. Schauss, J. Zeiher, T. Fukuhara, S. Hild, M. Cheneau, T. Macri, T. Pohl, I. Bloch, and C. Gross. Crystallization in Ising quantum magnets. *Science* **347**.6229 (2015), pp. 1455–1458.

[156] H. Kiesel, A. Renz, and F. Hasselbach. Observation of Hanbury Brown–Twiss anticorrelations for free electrons. *Nature* **418**.6896 (2002), pp. 392–394.

[157] A. Omran, M. Boll, T. A. Hilker, K. Kleinlein, G. Salomon, I. Bloch, and C. Gross. Microscopic Observation of Pauli Blocking in Degenerate Fermionic Lattice Gases. *Physical Review Letters* **115**.26 (2015).

[158] T. Rom, T. Best, D. van Oosten, U. Schneider, S. Fölling, B. Paredes, and I. Bloch. Free fermion antibunching in a degenerate atomic Fermi gas released from an optical lattice. *Nature* **444**.7120 (2006), pp. 733–736.

[159] M. Gajda, J. Mostowski, T. Sowiński, and M. Załuska-Kotur. Single-shot imaging of trapped Fermi gas. *EPL (Europhysics Letters)* **115**.2 (2016), p. 20012.

[160] D. Rakshit, J. Mostowski, T. Sowiński, M. Załuska-Kotur, and M. Gajda. On the observability of Pauli crystals in experiments with ultracold trapped Fermi gases. *Scientific Reports* **7**.1 (2017).

[161] L. Bayha. A Strongly Interacting Fermi Gas in a Two-Dimensional Optical Lattice. Masters's thesis. Heidelberg University, 2015.

[162] L. D'Alessio, Y. Kafri, A. Polkovnikov, and M. Rigol. From quantum chaos and eigenstate thermalization to statistical mechanics and thermodynamics. *Advances in Physics* **65**.3 (2016), pp. 239–362.

[163] A. Adams, L. D. Carr, T. Schäfer, P. Steinberg, and J. E. Thomas. Strongly correlated quantum fluids: ultracold quantum gases, quantum chromodynamic plasmas and holographic duality. *New Journal of Physics* **14**.11 (2012), p. 115009.

[164] E. Altman, E. Demler, and M. D. Lukin. Probing many-body states of ultracold atoms via noise correlations. *Physical Review A* **70**.1 (2004), p. 013603.

[165] J von Stecher, E Demler, M. D. Lukin, and A. M. Rey. Probing interaction-induced ferromagnetism in optical superlattices. *New Journal of Physics* **12**.5 (2010), p. 055009.

List of Publications

- **Observation of pair condensation in the quasi-2D BEC-BCS crossover**
  M. G. Ries*, A. N. Wenz*, G. Zürn*, L. Bayha, I. Boettcher, D. Kedar, P. A. Murthy, M. Neidig, T. Lompe, S. Jochim
  Phys. Rev. Lett. **114**, 230401 (2015)
  Some of the results of this publication have been used in chapter 3.

- **Observation of the Berezinskii-Kosterlitz-Thouless Phase Transition in an Ultracold Fermi Gas**
  P. A. Murthy*, I. Boettcher*, L. Bayha, M. Holzmann, D. Kedar, M. Neidig, M. G. Ries, A. N. Wenz, G. Zürn, S. Jochim
  Phys. Rev. Lett. **115**, 010401 (2015)
  Some of the results of this publication have been used in chapter 3.

- **Equation of State of Ultracold Fermions in the 2D BEC-BCS Crossover Region**
  I. Boettcher, L. Bayha, D. Kedar, P. A. Murthy, M. Neidig, M. G. Ries, A. N. Wenz, G. Zürn, S. Jochim, T. Enss
  Phys. Rev. Lett. **116**, 045303 (2016)

- **High temperature pairing in a strongly interacting two-dimensional Fermi gas**
  P. A. Murthy*, M. Neidig*, R. Klemt*, L. Bayha, I. Boettcher, T. Enss, M. Holten, G. Zürn, P. M. Preiss, S. Jochim
  Science **359**, 452-455 (2018)
  Some of the results of this publication have been used in chapter 3.

- **Quantum scale anomaly and spatial coherence in a 2D Fermi superfluid**
  P. A. Murthy*, N. Defenu*, L. Bayha, M. Holten, P. M. Preiss, T. Enss, S. Jochim
  Science **365**, 268-272 (2019)

- **Anomalous breaking of scale invariance in a two-dimensional Fermi gas**
  M. Holten, L. Bayha, A. C. Klein, P. A. Murthy, P. M. Preiss, S. Jochim
  Phys. Rev. Lett. **121**, 120401 (2018)

- **Observing the emergence of a quantum phase transition – shell by shell**
  L. Bayha*, M. Holten*, R. Klemt, K. Subramanian, J. Bjerlin, S. M. Reimann, G. M. Bruun, P. M. Preiss, S. Jochim
  arXiv:2004.14761 (2020)
  The results of this publication have been used in chapter 5.

- **Observation of Pauli Crystals**
  M. Holten*, L. Bayha*, K. Subramanian, C. Heintze, P. M. Preiss, S. Jochim
  arXiv:2005.03929 (2020)
  The results of this publication have been used in chapter 6.

The authors marked with * contributed equally to this publication.

A. Appendix

This appendix contains the probability distributions for all atom numbers of the pair excitation spectra for 6 atoms (Fig. 5.7) and for 12 atoms (Fig. 5.11 (a)).

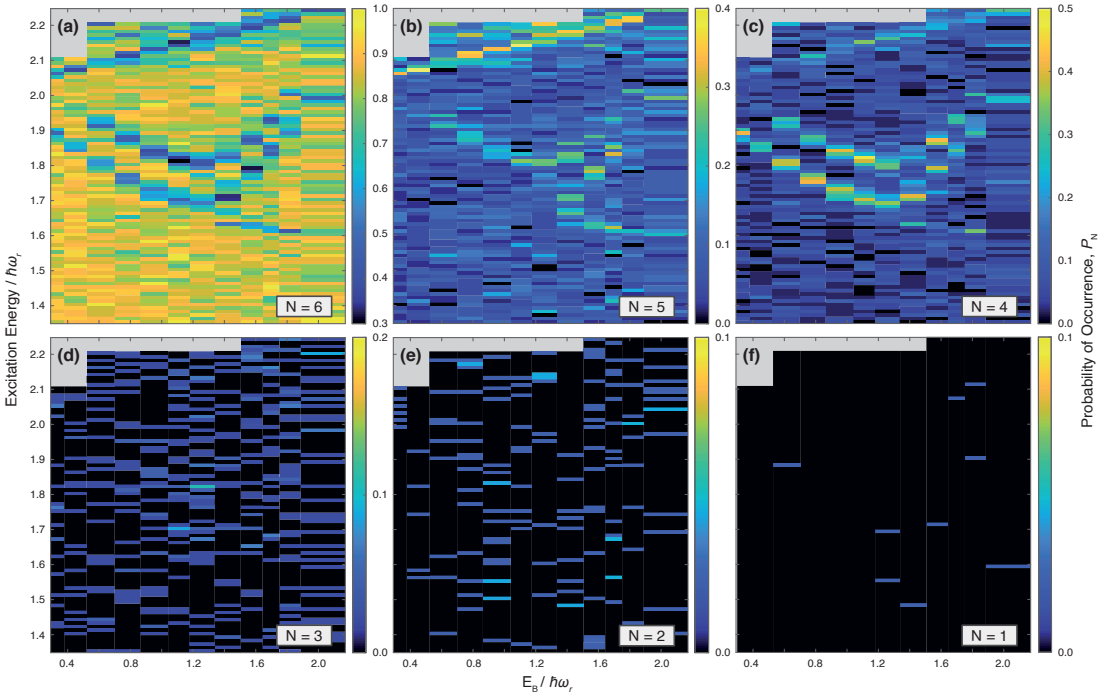

Figure A.1.: **Probabilities of retaining N atoms in the lowest 2 shells for the 6 atom initial state.** The different panels show the probability of detecting N atoms as function of the modulation frequency and interaction strength. All spectra are obtained by modulating the interaction strength. Note the different color scales of the different panels. From the reduced probabilities of measuring $N = 6$ atoms in (a) we find three resonances. The resonance highest in energy consist mainly of single particle excitations as both the probability of detecting $N = 5$ (b) and $N = 4$ (c) is increased at these frequencies. The lower two resonances show a non-monotonous interaction dependence and are pair excitations, as mainly the probability of detecting $N = 4$ atoms (c) is enhanced. The probability of detecting $N = 4$ atoms is approximately one half for the frequencies corresponding to the pair excitation as expected for an incoherent superposition of the ground and excited state (see section 5.3). The pair excitation is also non-linear and it is only possible to excite a single pair as seen from the flat probability distribution for $N = 2$ atoms. Figure adapted from Ref. [93].

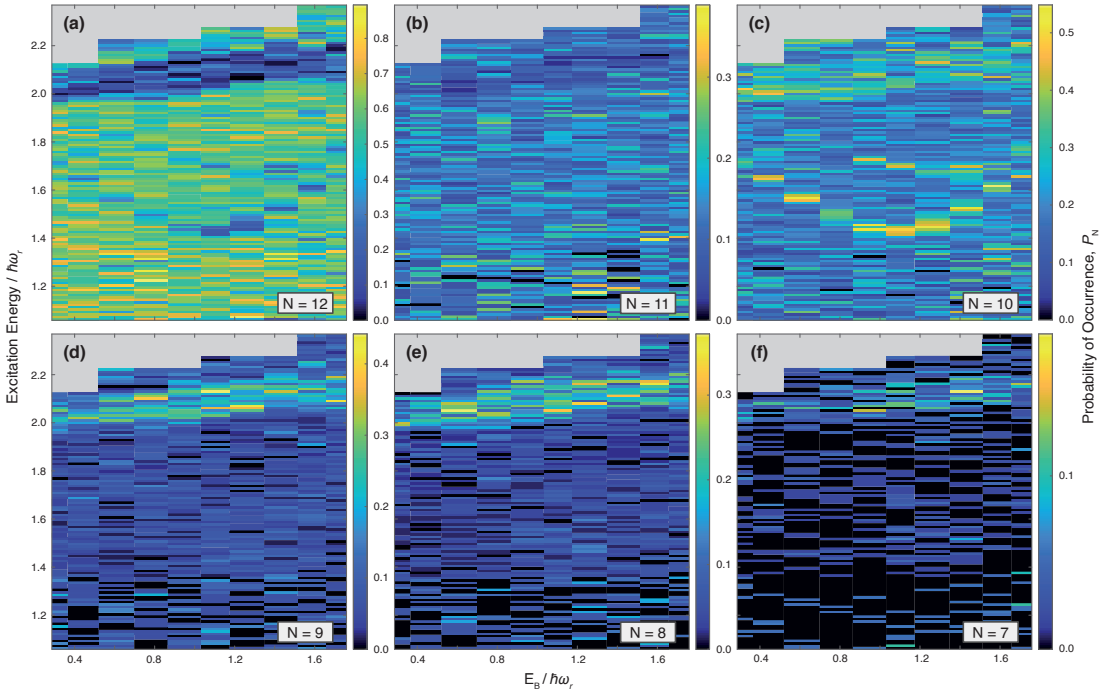

Figure A.2.: **Probabilities of retaining N atoms in the lowest 3 shells for the 12 atom initial state.** The different panels show the probability of detecting N atoms as function of the modulation frequency and interaction strength. All spectra are obtained by modulating the interaction strength. Note the different colors scale of the different panels. From the reduced probabilities of measuring $N = 12$ atoms in (a) we find three resonances. The resonance highest in energy consist mainly of single particle excitations as the probability of detecting $N = 10$ (c), $N = 9$ (d), $N = 8$ (e), $N = 7$ (f) atoms is increased at these frequencies. For the chosen drive strength and duration the system is excited several times at these frequencies, as seen form the complete depletion of the probability for $N = 11$ and $N = 12$ atoms in this frequency range. The lower two resonances show a non-monotonous interaction dependence and are pair excitations, as mainly the probability of detecting $N = 10$ atoms (c) is enhanced. The probability of detecting $N = 10$ atoms is approximately one half for the frequencies corresponding to the lower pair excitation as expected for an incoherent superposition (see section 5.3). The pair excitation is also non-linear and it is only possible to excite a single pair as seen from the probability distribution for $N = 8$ atoms (e), which shows no resonance in this frequency range. Figure adapted from Ref. [93].

Danksagung

Diese Arbeit zu schreiben, hätte ich ohne die großartige Unterstützung von vielen tollen Leuten nicht geschafft.
Zuerst geht mein Dank an Selim für all die Unterstützung in den letzten Jahren. Deine offene und optimistische Art und die Fähigkeit sich für alles zu begeistern, sowie dein unglaubliches technisches und pyhsikalisches Verständnis haben mir sehr geholfen.
Auch bedanke ich mich bei Prof. Markus Oberthaler für die Übernahme der Zweitkorrektur, sowie bei Prof. Maurits Haverkort und Priv.-Doz. José Crespo für die Bereitschaft, Teil des Prüfungskomitees zu sein.
Ein großer Dank geht an die ganze Ultracold Arbeitsgruppe für die gute Zusammenarbeit im Labor und die gemeinsamen sozialen Aktivitäten. Dem Team vom alten Experiment (in der Reihenfolge des Erscheinens) Gerhard, Simon, Andrea, Vincent, Jan Hendrik, Ralf, Michael, Lukas, Ram-Janik, Laurin und Philipp L. danke ich für die vielen coolen Diskussionen über Physik und sonstige Themen! Beim Team vom neuen Experiment Andre, Martin, Mathias, Puneet, Dhruv, Marvin, Philipp P., Antonia, Keerthan und Carl möchte ich mich zusätzlich noch für die großartige Zusammenarbeit am Experiment bedanken! Wir haben echt viel geschafft und coole Physik gemacht in den letzten Jahren.
I also want to thank our theory collaborators Igor Boettcher, Tilman Enss, Nicolo Defenu, Johannes Bjerlin, Stephanie Reimann and Georg Bruun. Discussing with you has significantly improved my understanding of strongly interacting Fermions!
Furthermore, I want to thank Dan Stamper-Kurn and his team (especially Zephy, Claire, Thomas and Johnathan) for the time in Berkeley. It was fun even though we had to suffer quite some technical problems.
Ein besonderer Dank geht an die Korrekturleser Marvin, Jan Hendrik, Ralf, Keerthan, Philipp P., Philipp K. und Paul.
Auch möchte ich mich bei meinen Freunden in Stuttgart, Heidelberg und an allen anderen Orten für die tolle Ablenkung von der Arbeit und jede Menge Spaß bedanken. Ein besonderer Dank geht hier an Philipp K. für die Donnerstagabende, die coolen Reisen und dass du alle Übungsblätter mit mir gemacht hast!
Ich freue mich, dass ich eine so tolle Familie (inklusive aller Leute im Starenweg) habe und mich immer auf euch verlassen kann, wenn es Probleme gibt und ihr mich immer unterstützt.
Zuletzt möchte ich noch Caro für die Unterstützung (vor allem in den letzten sicher anstrengenden Wochen) danken! Ich bin froh, dass es dich gibt.